

THESIS ON NATURAL AND EXACT SCIENCES B214

**An Evolution of Freshwater Bulge in  
Laboratory Scale Experiments and  
Natural Conditions**

EDITH SOOSAAR

**TUT**  
PRESS

# TALLINN UNIVERSITY OF TECHNOLOGY

## Marine Systems Institute

Dissertation was accepted for the defence of the degree of Doctor of Philosophy in Earth Sciences on April 29, 2016

**Supervisors:** Prof. Urmas Raudsepp, Marine Systems Institute at Tallinn University of Technology.

Prof. Robert D. Hetland, Department of Oceanography Texas A&M University.

**Opponents:** Dr. Andreas Lehmann, Helmholtz Centre for Ocean Research Kiel, Germany

Dr. Aarne Männik, Senior Researcher, Laboratory of Atmospheric Physics, Tartu University

Defense of the thesis: 21.06. 2016

Tallinn University of Technology

Akadeemia tee 15a, Tallinn

### **Declaration:**

*Hereby I declare that this doctoral thesis, my original investigation and achievement, submitted for the doctoral degree at Tallinn University of Technology has not been submitted for any degree.*

Edith Soosaar .....

Copyright: Edith Soosaar, 2016

ISSN 1406-4723

ISBN 978-9949-23-966-5 (publication)

ISBN 978-9949-23-967-2 (PDF)

LOODUS- JA TÄPPISTEADUSED B214

# **Jõevee levik rannikumeres Riia lahe näitel**

EDITH SOOSAAR



# Contents

<b>Table of Contents</b>	<b>5</b>
<b>List of original publications</b>	<b>6</b>
<b>List of acronyms and symbols</b>	<b>7</b>
<b>1 Introduction</b>	<b>8</b>
<b>2 Materials and methods</b>	<b>10</b>
2.1 Laboratory scale study . . . . .	10
2.2 Natural scale study . . . . .	12
2.2.1 Description of the GoR . . . . .	12
2.2.2 Numerical simulations . . . . .	13
2.2.3 Remote sensing data . . . . .	14
<b>3 Results and discussion</b>	<b>15</b>
3.1 River bulge development in laboratory scale . . . . .	15
3.2 River bulge development in natural conditions. . . . .	19
3.3 Bulge momentum balance . . . . .	23
3.4 Background circulation in the GoR. . . . .	28
<b>4 Conclusions</b>	<b>31</b>
<b>Bibliography</b>	<b>33</b>
<b>Paper I</b>	<b>39</b>
<b>Paper II</b>	<b>51</b>
<b>Paper III</b>	<b>69</b>
<b>Acknowledgments</b>	<b>81</b>
<b>Abstract</b>	<b>82</b>
<b>Resümee</b>	<b>84</b>
<b>Curriculum Vitae</b>	<b>86</b>
<b>Elulookirjeldus</b>	<b>88</b>

## List of original publications

The thesis is based on following papers that are referred to in the text by Arabic numbers.

- I Soosaar, E., Hetland, R.D., Horner-Devine, A., Avenier, M. E. and Raudsepp, U. (2014). Offshore spreading of buoyant bulge from numerical simulations and laboratory experiments. 2014 IEEE/OES Baltic International Symposium. DOI: 10.1109/BALTIC.2014.6887889
- II Soosaar, E., Maljutenko, I., Uiboupin, R., Skudra, M. and Raudsepp, U. (2016). River bulge evolution and dynamics in a non-tidal sea - Daugava River plume in the Gulf of Riga, Baltic Sea. *Ocean Sci.*, 12, 417-432.
- III Soosaar, E., Maljutenko, I., Raudsepp, U. and Elken, J. (2014). An investigation of anticyclonic circulation in the southern Gulf of Riga during the spring period. *Continental Shelf Research*, 78, 75 - 84.

## Author's contribution

- I In the first publication the author performed numerical model simulations and analyzed the raw data from laboratory experiments and numerical simulations. The author wrote the manuscript
- II The author assisted with selecting the data and data analysis as well as with writing the manuscript (except the method part for satellite imagery and model description).
- III In the third publication the author analyzed data from numerical simulations and assisted on setting up numerical simulations for the specific idealized cases. The author performed linear regression calculations, analysis and prepared corresponding images. The author drafted the main part of the manuscript (with the exception of the numerical model description and the PCA analysis part in the method section).

## List of acronyms and symbols

- GoR - Gulf of Riga
- ROFI - Region of Freshwater Influence
- ROMS - Regional Ocean Modeling System
- GETM - General Estuarine Transport Model
- GOTM - General Ocean Turbulence Model
- $v_\theta$  - depth-averaged orbital velocity
- $r$  - radial coordinate relative to the center of the bulge circulation
- $f$  - Coriolis parameter
- $g' = g(\rho_0 - \rho_i)/\rho_0$  - reduced gravity ( $g$  - gravitational acceleration,  $\rho_0$  - ambient density,  $\rho_i$  - inflow density).
- $h$  - buoyant layer thickness /bulge thickness
- $L_b = \left(\frac{2Qg'}{f^3}\right)^{\frac{1}{4}}$  - bulge Rossby radius
- $Q$  - inflow rate
- $U = Q(HW)^{-1}$  - mean inflow velocity
- $H$  - inflow thickness
- $W$  - inflow width
- $t$  - time
- $TSM$  - Total suspended matter
- $T$  - rotation period
- PEA - Potential Energy Anomaly
- $R_0$  - Rossby number

# 1 Introduction

Fresh water from rivers contributes significant amounts of buoyancy to large areas of the coastal sea. The region where buoyancy input by rivers is comparable to or exceeds the seasonal input of buoyancy as heat is called ROFI (a term adapted by [46]).

River water entering a coastal ocean typically forms a buoyant plume with an expanding anti-cyclonically rotating bulge near the river mouth and a coastal current in the coastally trapped wave direction [55, 18, 5, 22, 23, 10, 25, 24, 21, 38, 33]. A coastal current is generally considered to be in a geostrophic balance [18, 49, 10]. Yankovsky and Chapman (1997) [55] hypothesized and Horner-Devine (2009) [24] confirmed for the Columbia River plume that the dynamics of the river bulge are described as balanced between centrifugal, Coriolis and pressure gradient force. Horner-Devine et al. (2015) [26] have summarized the dynamics of an anti-cyclonically rotating bulge, with special emphasis on the river water volume recirculating within the bulge. In their study, with reference to Nof and Pichevin (2001) [37], they summarize that, with stronger anti-cyclonic circulation within the bulge, more water recirculates in the bulge. It is suggested that the amount of water going into the coastal current depends on the Rossby number,  $Ro = U/fW$  [18]. With high Rossby number  $\mathcal{O}(1)$  most of the freshwater stays in the bulge. The proposed magnitude of water in the bulge ranges from 30-75% [37, 5, 10, 23].

In natural conditions, the evolution of the bulge is affected by properties of the outflow [55, 5], tides [52], wind [17, 54, 11, 29] and the ambient circulation [18]. When an estuary is wider than the internal Rossby deformation radius, the combination of classical longitudinal estuarine circulation and the Earth's rotation may cause the surface circulation to become anti-cyclonic [19]. In the northern hemisphere, this circulation would eventually transport fresh water from the river along the left hand coast, opposite to the coastally trapped wave direction. Such a circulation would have longer timescale than river bulge events.

Anti-cyclonic residual circulation has been observed at the estuary head of Ise Bay, Osaka Bay and Tokyo Bay [19]. Measurements in the Kara Sea show the presence of an anticyclonic circulation in the Ob River discharge region in the late summer period [36], which was reproduced by numerical simulations [39]. In the Gulf of Trieste, in the northern Adriatic, an anti-cyclonic gyre covers the surface layer during the stratified season [34]. In all of these cases, the salinity distribution consists of vertical stratification, i.e. a brackish upper layer and a more saline lower layer, and a horizontal salinity gradient in the surface layer.

In this thesis we cover research done on a circulation in the coastal sea influenced by buoyant river discharge(s). The study focuses on surface

advective river plumes and circulation in the wide estuaries.

The main objective of the present thesis is to study the buoyant river bulge in the coastal sea and the circulation in the head of the gulf type ROFI, which affects the spreading of river water. The specific aims are:

- to study river bulge evolution on laboratory scale with different characteristics of inflowing and ambient water (Paper I).
- to show river bulge evolution and dynamics in a non-tidal sea including evidence of the anticyclonic circulation within the Daugava river bulge (Paper II).
- to assess current theoretical understanding of river bulge internal structure and dynamics (Paper II).
- to map the most common circulation patterns in the GoR that influence river water spreading in spring using long term simulation for the Baltic Sea area (Paper III).

The thesis is organized as follows. Chapter 2 gives an overview of materials and methods. The results are presented in Chapter 3. River bulge evolution both in laboratory and natural scale is described in subsections 3.1 and 3.2 respectively. River bulge dynamics is discussed in subsections 3.3 and background circulation in the GoR in subsections 3.4. Main conclusions are summarized in Chapter 4. The main results of the work are presented in more detail in three attached papers (denoted by Roman numerals I to III)

## 2 Materials and methods

### 2.1 Laboratory scale study

Rotating table laboratory experiments were carried out in the University of Washington’s Harris Hydraulics Laboratory. An annular tank (inner radius = 22 cm, outer radius = 92 cm and depth of 20 cm) was placed on the table and filled with salt water (salinity = 1-5 g kg<sup>-1</sup> depending on the experiment) (Figure 1). A steep coastal wall was simulated by a vertical Plexiglas sheet in the tank. The table was brought to a rotation rate of  $\Omega$  and spun up at that rate for 60 minutes. After spin-up, fresh water (dyed with red food dye) was pumped onto the surface of the salt water. The fresh water entered the tank through a 1 cm deep and 5 cm wide gap in the coastal wall. To achieve a uniform velocity profile a fine sponge in the inlet was used to diffuse the inflow. The rotating tank and configurations are described in detail in [23, 56]. (Paper I).

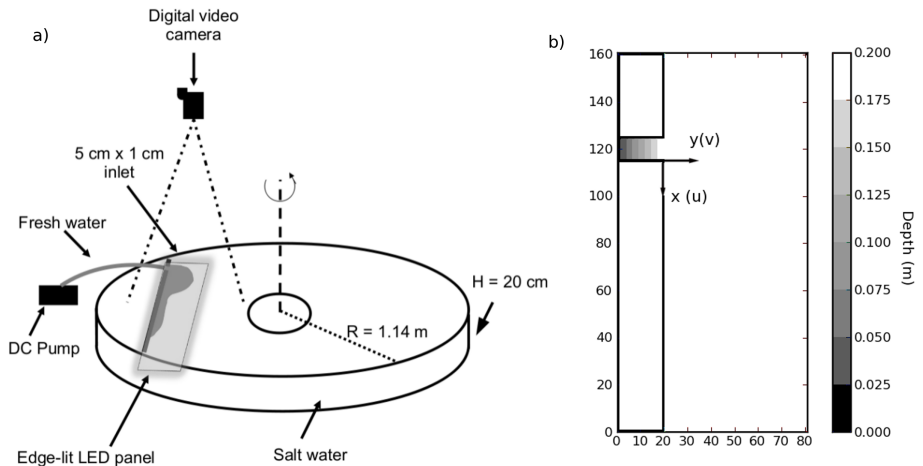


Figure 1: (a) Plan of the laboratory experiment, (b) Plan view of study domain. Study area size 30x80 cm with uniform 20 cm depth. Inlet basin with sloping bottom located in the ‘western’ wall. Fresh water is introduced to the system through the inlet basin. Downcoast direction is toward x and offshore direction is toward y, u and v are velocities in the according direction. Adapted from Paper I

Numerical model ROMS was used to study the model’s ability to reproduce a river plume on laboratory scale  $\mathcal{O}(1$  cm). ROMS is a 3-dimensional, hydrostatic, primitive-equation ocean model that uses a split-explicit scheme

to solve for a free surface [43, 44]. Numerical simulations of the river discharge into a rectangular tank, along the straight wall were made. The model's horizontal resolution was  $\Delta x = \Delta y = 0.5$  cm with 30 layers in vertically stretched  $\sigma$ -coordinates. Fresh water is added through the inlet basin in the "western" wall. A total of 14 model simulations was performed by modifying: 1) the background salinity, 2) fresh water inflow rate, 3) tidal amplitude, and 4) rotation rate of the tank in order to reproduce laboratory experiments. (Paper I).

## 2.2 Natural scale study

### 2.2.1 Description of the GoR

The GoR contains brackish water and is an almost bowl-shaped and semi-enclosed sub-basin of the Baltic Sea. Its area is about  $18\,000\text{ km}^2$  (110 km wide and 140 km in length), with a mean depth of 22 m (Figure 2). GoR is connected with the Baltic Sea by two straits in the north-west. Irbe Strait is 25 m deep, with minimum cross-section area of  $0.4\text{ km}^2$  and Virtsu Strait is 5 m deep, minimum cross-section area of  $0.04\text{ km}^2$ . It's small tidal oscillation ( $\mathcal{O}(1 - 10\text{ cm})$ , [30]) allows it to be considered as a non-tidal estuary.

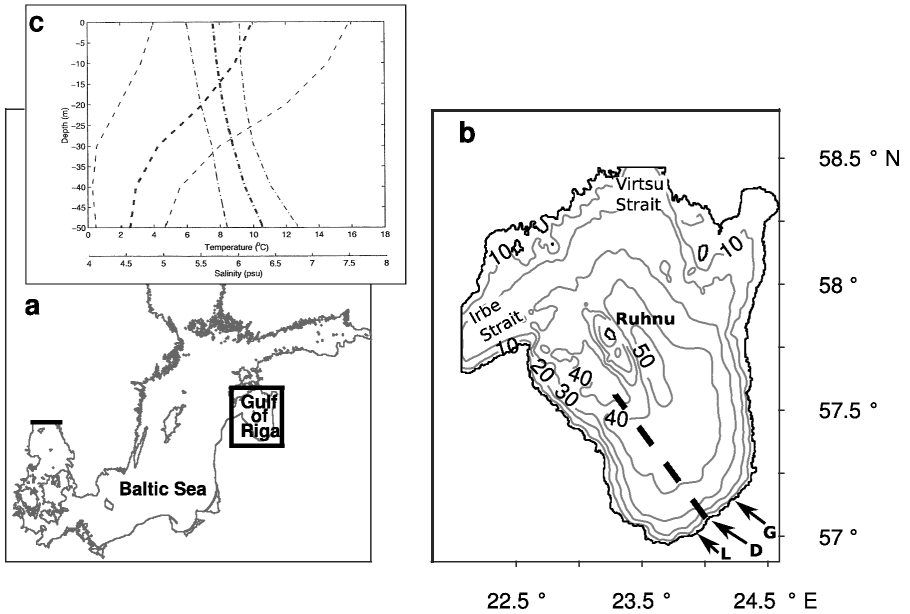


Figure 2: Map showing the location of the Gulf of Riga in the Baltic Sea (a), topography of the Gulf of Riga [1](b). Arrows mark river mouth locations for the Daugava (D), Lielupe (L) and Gauja (G) rivers. Bold dashed line shows the transect of ferry-box measurements used for the model validation in Paper II. Mean temperature (bold dashed) and salinity (mean dash dotted) profiles with standard deviations (thin) from the central Gulf of Riga (c) (Paper II).

The main fresh water source for the area is the Daugava River at the south-eastern coast of the GoR. Its discharge ranges from  $200\text{ m}^3\text{s}^{-1}$  in late summer to  $2500\text{ m}^3\text{s}^{-1}$  in early spring. The Daugava river is located between two smaller rivers, Gauja 18 km to the north-east and Lielupe

8 km to the south-west with a discharge ranging from 20 to 220  $m^3s^{-1}$  and from 20 to 380  $m^3s^{-1}$  respectively.

As the GoR is shallow it is usually vertically mixed from December to March [41]. The annual ice period and extent varies in wide range depending on the severity of the winter. During the summer and autumn stratification is mostly maintained by temperature flux from the atmosphere. During March-April increased freshwater discharge creates a two-layer vertical salinity stratification [47]. During that time GoR can be considered as classical gulf type ROFI where buoyancy from rivers exceeds buoyancy created due to the atmospheric fluxes [46].

## 2.2.2 Numerical simulations

The numerical model adapted for the Baltic Sea is a fully baroclinic and hydrostatic ocean model GETM [8] that is coupled to the GOTM [50] for vertical turbulence parametrization. The GETM uses a spherical coordinate system in the horizontal plane and a bottom-following vertical coordinate system. Using a mode splitting technique, GETM solves water dynamics on the Arakawa C-grid [3]. The GETM is characterized by advanced numerical techniques of advection schemes and internal pressure discretization schemes that minimize computational errors [40, 43, 48, 9, 31].

Numerical simulations were made to study formation of an anti-cyclonic rotating bulge at the Daugava river discharge from 20 March to 5 April 2007. The study area covered GoR with closed boundaries at the Irbe Strait and the Virtsu Strait. The simulation was made with fine horizontal resolution of 0.125 km. The vertical water column was split into 30 density adaptive layers. Hourly river runoff input from the measurements of three rivers, Daugava, Lielupe and Gauja, was included. The meteorology was adapted from the EM-CWF ERA-Interim data set with a lateral resolution of 25 km and a temporal resolution of 6 h [12]. Initial salinity fields were interpolated from the 1 nautical mile simulation for the Baltic Sea [35]. Additional numerical sensitivity tests were made with (1) stratified GoR without wind forcing (2) homogeneous GoR (6  $gkg^{-1}$ , [41]) and without wind forcing and (3) cross-shore and alongshore wind (2 and 4  $ms^{-1}$ ). (Paper II).

Using GETM, a ten year numerical simulation was made for the total Baltic Sea area from 1997 to 2006. The simulation was made with coarse spacial resolution using a horizontal grid step 3.7 km. The vertical water column was split into 25 sigma layers. Initial salinity and temperature fields were interpolated from the climatic mean field constructed using the Data Assimilation System coupled with the Baltic Environmental Database at Stockholm University (<http://nest.su.se/das>, [28]). Atmospheric forcing was adapted from the ERA40 re-analysis data which had been dynamically

down-scaled with the Rossby Centre Atmosphere Ocean (RCAO) model [15, 16]. River runoff was obtained from the hydrological model HYPE [32]. In total data from 40 spring months (from March to June) was analyzed. We studied monthly mean velocity fields. Additional simplified simulations were made including only the GoR area with closed boundaries at the Irbe and Virtsu Straits, with various combinations of initial and forcing conditions (Figure 2). (Paper III).

### **2.2.3 Remote sensing data**

ENVISAT/MERIS data with 0.3 *km* resolution was used for monitoring bulge dynamics and structure (<http://www.coastcolour.org/data/archive/>). The MERIS images were processed using Case-2 Regional algorithm [13, 14]. TSM (total suspended matter) concentration was used as a marker to distinguish turbid river water from clear sea water [20, 51, 4, 6, 45]. Over the studied time period seven sufficiently cloud free images were available from March 20th, 26th, 27th, 29th, 30th and April 1st and 4th 2007. For a more detailed description see Paper II.

## 3 Results and discussion

### 3.1 River bulge development in laboratory scale

Time evolution of the fresh water thickness distribution for the first numerical and laboratory simulations show that during the first  $0.5 T$ , both laboratory and numerical plume fronts have spread 12-13 *cm* offshore, and some of the fresh water is beginning to be carried downcoast (Figure 3). By the end of the first rotation period bulge and coastal current are formed for both studies. From 2-8  $T$ , bulge expansion is slower but still steady for both experiments. The front location is reproduced with  $\sim 10\%$  accuracy until the end of 8  $T$ . Numerical simulation underestimates the width of the coastal current. In the laboratory simulation a bigger concentration of the fresh water is located near the discharge and along the coast. (Paper I). Such a development agrees well with theoretical bulge spreading for the river discharge along the straight coast [37].

The numerical model reproduces the bulge remarkably well when the inflow Kelvin number,  $K = Wf/(g'H)^{-1}$ , is about one (Figure 3). When  $K > 1$  or  $K < 1$ , the model accordingly underestimates or overestimates the bulge offshore reach. (Paper I).

The difference was likely caused by the use of the inlet channel. Using such an inlet to lessen instability from direct input is common practice in river plume modeling. However the present study shows that with wide/narrow inlet channel in comparison to the inflow Rossby deformation radius,  $L_0 = (g'H)^{1/2}f^{-1}$ , water flow is altered before reaching the main basin, hence changing discharge conditions. With a wide inlet, outflow is not uniform across the channel but deflected to the right due to rotational effects. Using an inlet channel instead of direct inflow alters the bulge spreading during initial bulge formation when the front moves rapidly offshore. This lasts approximately 0.3-0.7 rotation period. Then spreading slows down and continues at steady phase of  $0.1 \text{ cm s}^{-1}$  for numerical and  $0.11 \text{ cm s}^{-1}$  for laboratory bulge until the end of the simulation. The shift time from first to the second phase loosely corresponds with the formation of a coastal current. (Paper I). This confirms theoretical study by Huq 2009 [27] where it is concluded that the velocity profile at the river mouth varies with the Kelvin number.

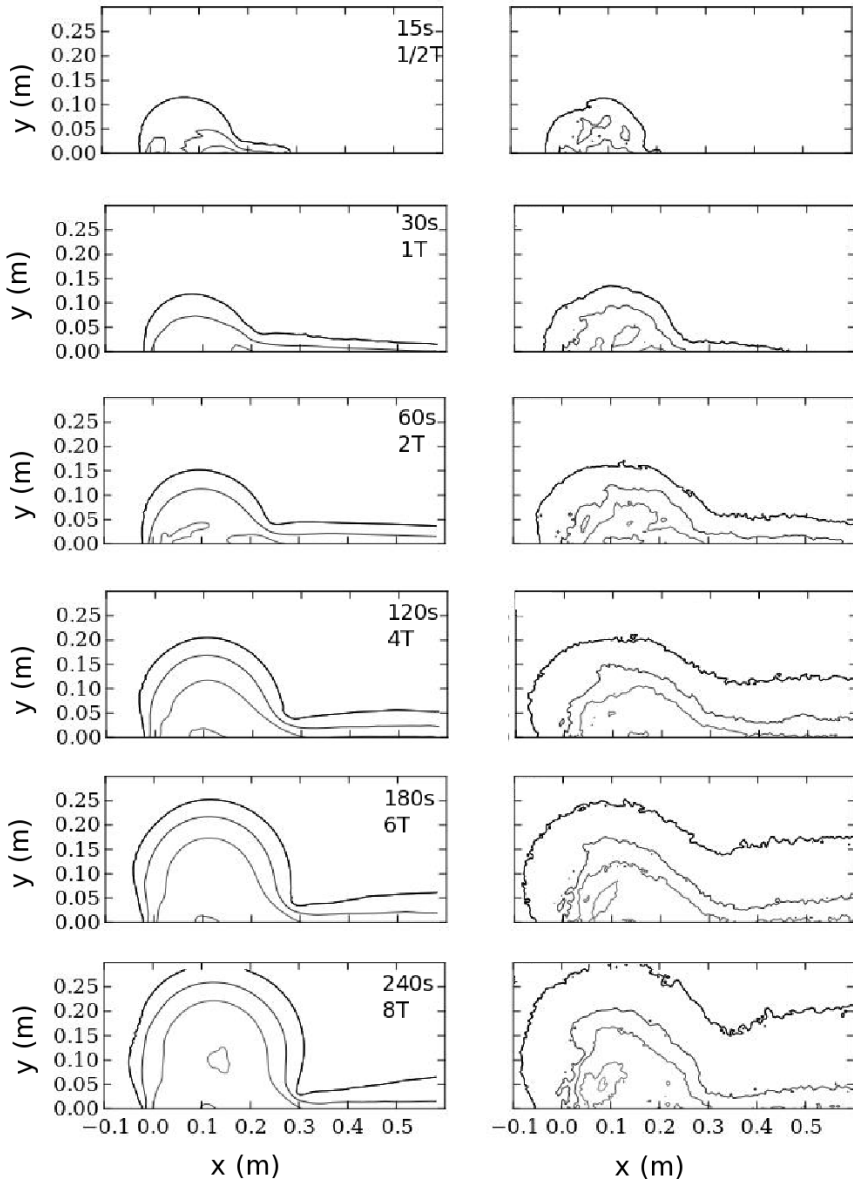


Figure 3: Time evolution of fresh water thickness (fwt) for numerical simulations (left column) and corresponding laboratory experiments (right column) at time  $1/2 T$ ,  $1 T$ ,  $2 T$ ,  $4 T$ ,  $6 T$  and  $8 T$ . Bold line is edge of fresh water area where  $fwt = 0.1 \text{ cm}$ , contour interval is  $0.5 \text{ cm}$ . Adapted from Paper I)

From laboratory and numerical experiments expansion is usually estimated by bulge effective radius or front offshore location. Both increase proportionally to the bulge Rossby radius [23, 25, 5],

$$L_b = \left( \frac{2Qg'}{f^3} \right)^{1/4} \quad (1)$$

where  $Q$  is river discharge.

We approximated the growth rate of the bulge radius using a power function,

$$r_b = \frac{r}{L_b} \simeq \left( \frac{t}{T} \right)^n \quad (2)$$

where  $t$  is the time after the initiation of the plume,  $T$  is the rotation period, and  $n$  is an exponent describing the growth rate [23, 25, 5].

From laboratory experiments we estimated  $n = 0.48$  ( $R^2 = 0.80$ ) and from numerical simulations  $n = 0.36$  ( $R^2 = 0.85$ ) (Figure 4). This agrees reasonably well with previous laboratory simulations [23] and [5] where  $n = 0.39$  and  $n = 0.4$ , respectively. Our study supports the conclusion that bulge expansion scales with bulge Rossby radius instead of inertial radius.

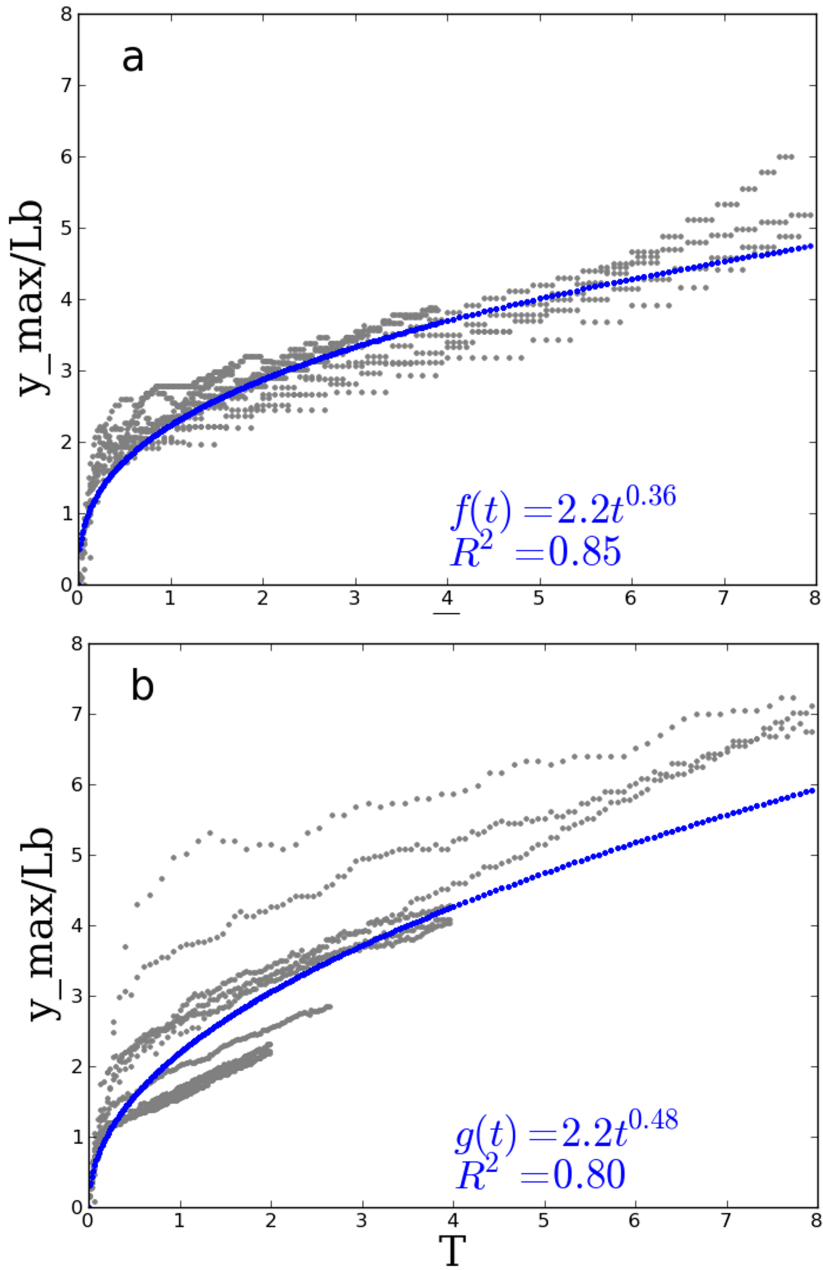


Figure 4: Bulge front maximum offshore reach over time from a) laboratory simulation and b) numerical model. The blue line is a fitted power function.  $R^2$  is coefficient of determination.

### 3.2 River bulge development in natural conditions.

The first satellite image on 20 March showed three river plumes, all consisting bulge area and a coastal current Figure 5. Right before the first satellite image, the wind speed dropped from 11 to  $2 \text{ ms}^{-1}$  that is favorable for the plume development. The plume on 26 March was the result of the re-initiation of the river plume on 24 March. The core of the bulge was almost circular, with intrusions along the outer rim. In the core high TSM concentration of freshly discharged water formed a jet with an anti-cyclonic spreading pattern along the left side of the bulge. During that period the northeasterly wind may push the bulge offshore and cause intrusions. Model simulation showed a strong background anti-cyclonic circulation of about  $20 \text{ cms}^{-1}$  in the south-eastern GoR. During the next 4 days, i.e. until 30 March, the wind speed was very low, between 0 and  $3 \text{ ms}^{-1}$ . The main feature inside the bulge was anti-cyclonically turning river water with a high TSM concentration (Figure 5 c-e) and a well established anti-cyclonic circulation in the bulge, with a characteristic current speed of  $20 \text{ cms}^{-1}$  (Figure 5 il). This gives direct confirmation that water in natural buoyant bulges circulates anti-cyclonically in the Northern Hemisphere. By 1 April, the bulge had been transported westward and nearly detached from the Daugava River outlet. Due to increased wind around April 2 the bulge has dispersed by the April 4. In the idealized simulation where river discharge into a homogeneous GoR with forcing switched off river plume developed steadily into an anti-cyclonically recirculating bulge and a coastal current. Paper II.

The bulge effective radius,  $r_b$ , was estimated through the area of the bulge,  $A_b$ , assuming a circular shape of the bulge [23]:

$$r_b = \frac{A_b^{\frac{1}{2}}}{\pi} \tag{3}$$

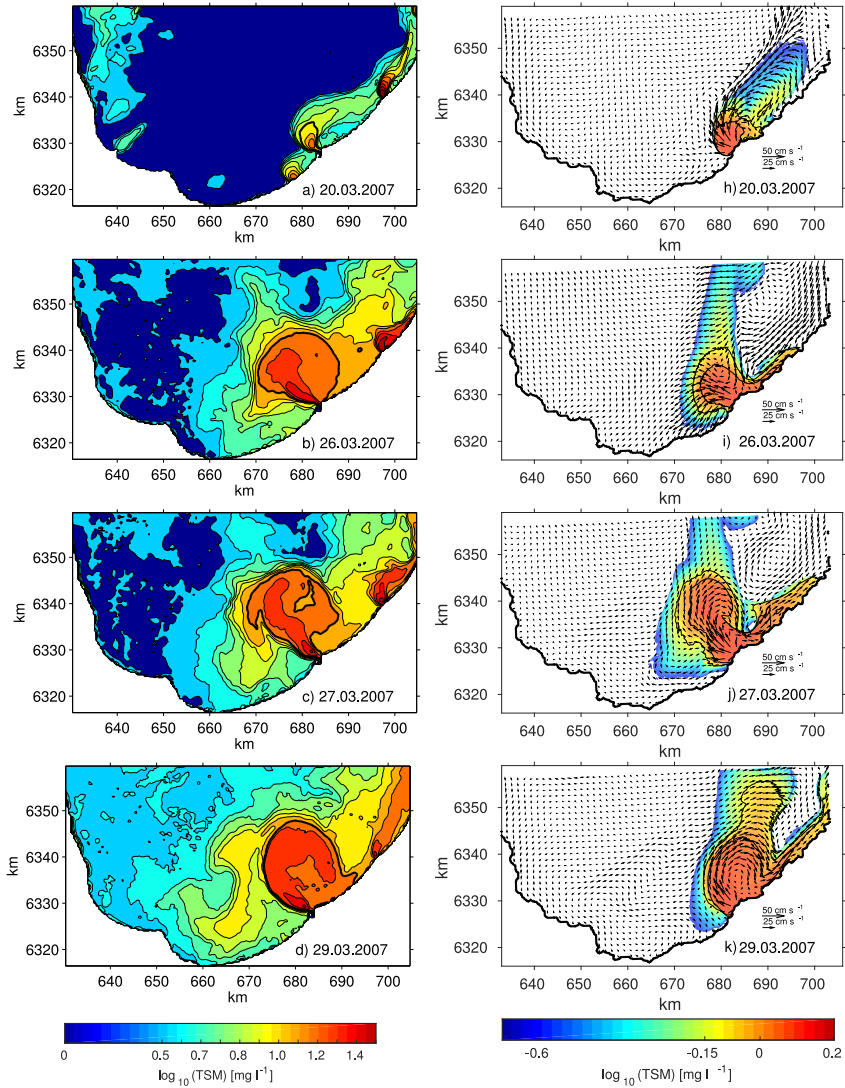


Figure 5: TSM concentration maps for the southern part of the Gulf of Riga from satellite images (left column) and TSM concentration and surface velocity maps from the numerical simulation (right column). The bold contours on the satellite images show the indicative edge of the Daugava River bulge. Black contours on the numerical model simulation maps represent TSM concentrations of  $\log_{10}(\text{TSM}) = -0.15$  and  $= -0.05$ . The former is used for the determination of the Daugava River bulge. The coordinate system is on the UTM-34v projection. Paper II.

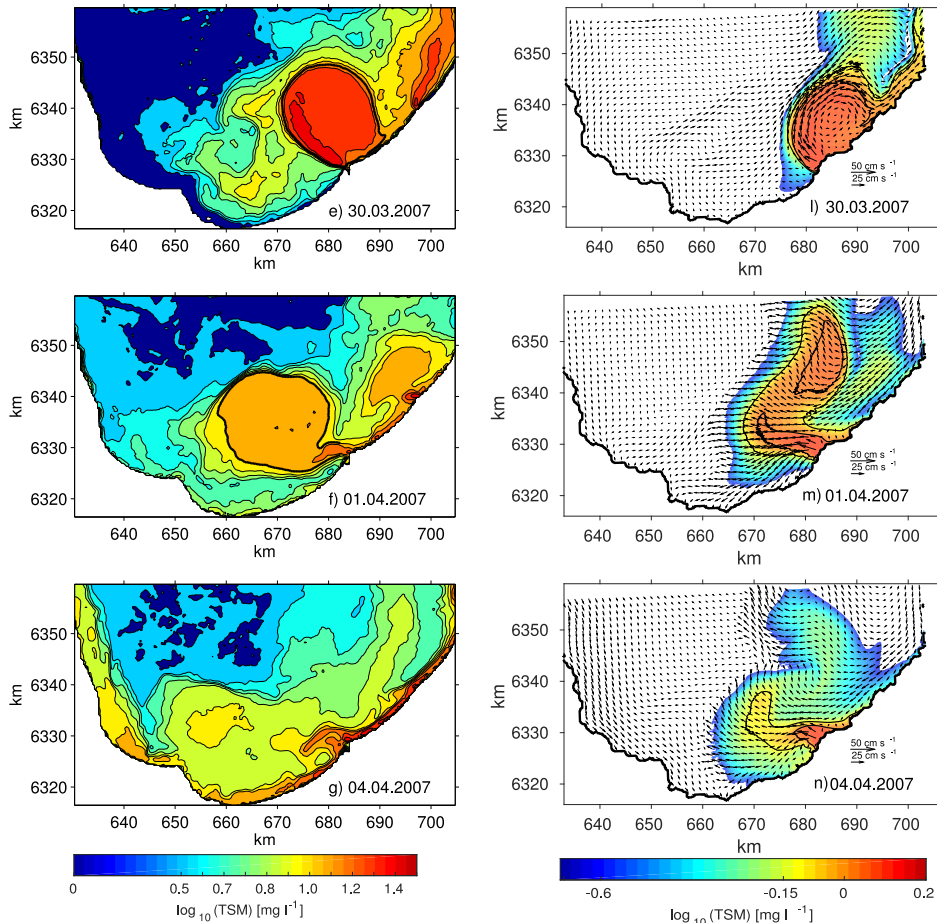


Figure 5: continued.

In our case, the bulge Rossby radius varied between 2.7 and 3.1  $\text{km}$  in time, according to the actual runoff of the Daugava River. We approximated the growth rate of the bulge radius using a power function. In the real case, we excluded the time period when the bulge started to dissipate, i.e. maintaining the values up to  $8 T$ . The real and ideal simulations gave  $r_b \sim t^{0.50 \pm 0.04}$  and  $r_b \sim t^{0.28 \pm 0.01}$ , with the coefficients of determination being  $R_2 = 0.90$  and  $R_2 = 0.98$  respectively. Thus, in the real model simulation, the growth of the bulge radius was faster than in the ideal simulation. It can be explained by prevailing upwelling favorable winds which even with a speed of  $3\text{-}4 \text{ m s}^{-1}$  restrained the development of a coastal current and retained more water in the bulge. Paper II. The bulge spreading rates agree well with laboratory experiments ( $\sim t^{1/4}$  by [23]) and fit in the margin of the Niagara River bulge study ( $\sim t^{0.46 \pm 0.29}$  by [25]).

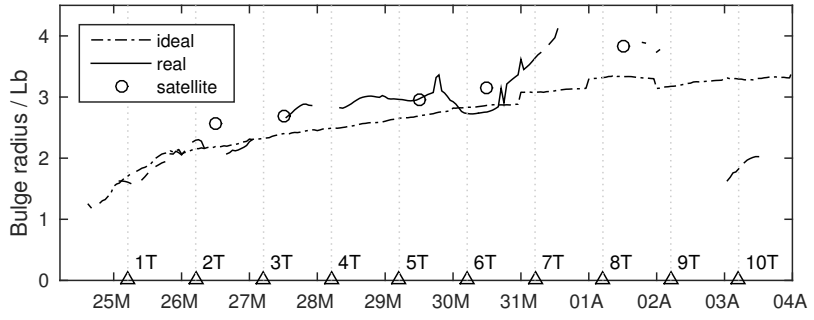


Figure 6: Time series of the bulge effective radius scaled with bulge Rossby radius from satellite data (circles), real (solid) and idealized (dash-dotted) numerical simulations. Adapted from Paper II.

### 3.3 Bulge momentum balance

The dynamics of the river bulge are described as a balance between centrifugal, Coriolis and pressure gradient terms [55, 23]:

$$\frac{v_\theta^2}{r} + f v_\theta = g' \frac{\delta h}{\delta r} \quad (4)$$

We calculated the time series of spatially averaged momentum balance terms, Eq. 4, for the ideal bulge (Figure 7 a) and the real bulge (Figure 7 b). For the ideal bulge, all three terms contributed significantly to the momentum balance during the initial phase of bulge development, i.e. up to  $1 T$  (Figure 7 a). Between  $1 T$  and  $2 T$  the contribution from the centrifugal force decreased, so that this term became nearly an order of magnitude smaller than the Coriolis term and the pressure gradient term. In the case of the real bulge the initial value of the centrifugal force was an order of magnitude smaller than the Coriolis and pressure terms already at the beginning. Paper II.

We calculated these terms for the case of the real bulge and the ideal bulge development on 29 March 2007 at 20:00. With the exception of the near-field region, the centrifugal force was nearly an order of magnitude smaller than the Coriolis term and the pressure gradient term (Figure 8). Paper II.

Although the ideal and real bulges were similar quantitatively, the bulge center was much closer to the coast (3 km) for the ideal bulge than for the real bulge (6 km). The explanation for the discrepancy between the ideal bulge and laboratory experiments could be the different behavior of the plume in a near-field region. In a near-field region, river flow has a lift-off point in the location where river water detaches from the bottom and the upper layer Froude number,  $Fr = U(g' H_r)^{-1/2}$ , is equal to one [26]. At the lift-off point, vertical velocities cause shoaling of the plume interface and acceleration of the upper layer flow in a more seaward region. This, in turn, increases the Froude number, resulting in intense vertical mixing. Paper II.

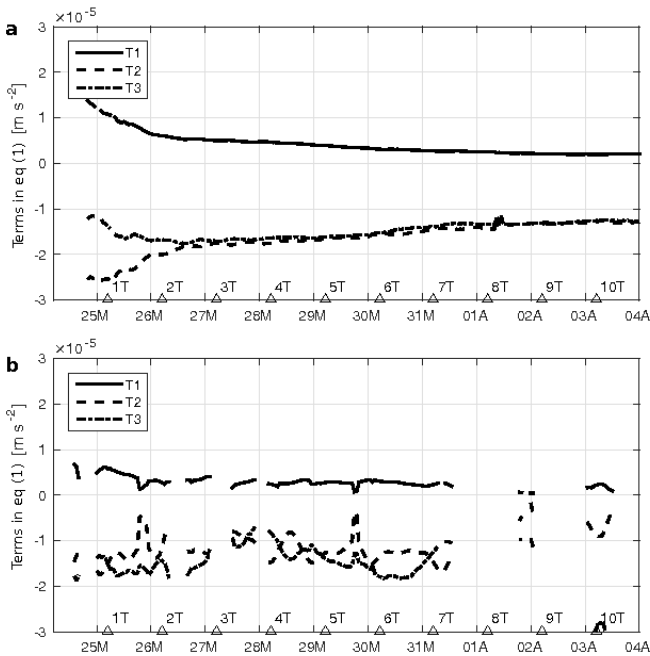


Figure 7: Time series of spatially averaged momentum balance terms (see Eq. 4): centrifugal term (T1) (solid), Coriolis term (T2) (dashed), pressure gradient term (T3) (dash dotted) for ideal (a) and real bulge (b). Triangles represent the rotation period of the earth starting from 24 March 2007 05:00. Paper II.

In our idealized numerical simulation, the lift-off occurred at about  $0.5 \text{ km}$  from the river mouth (Figure 8 a). The most intensive mixing started at  $1 \text{ km}$  from the coast where tracer concentrations were below the limit of the bulge definition (white area in Figure 8). In our case the Froude number,  $Fr \geq 2$ , there (Figure 9). The intensive mixing suppressed horizontal flow and the current velocities were low right behind the intense mixing zone, while the current velocities were higher at the left and right sides of the mixing zone (Figure 8 a). Thus, the intensive mixing zone created a barrier for the river water flow and split it into two jets. The jet on the right formed a rotating bulge. As the barrier altered the flow direction, the flow angle was notably smaller than  $90^\circ$ , resulting in a bulge center located closer to the coast [5]. The jet on the left remained on the outer edge of the bulge. Paper II.

Such a barrier region is not observed in realistic model simulations (Figure 8, right column). Natural buoyant river plumes have a small vertical to horizontal aspect ratio,  $\mathcal{O}(10^3)$ , where vertical turbulent flux of density was considered to be dominant over horizontal turbulent fluxes [26]. For labo-

ratory scale simulations, the aspect ratio is at least an order of magnitude smaller. Horizontal turbulence flux would be comparable in magnitude to vertical mixing, and a sharply separated region of intense mixing is far less likely to form. In addition, in our numerical simulations, the Daugava River runoff was smeared over five horizontal grid points right at the coast, which enables a better resolution of the river plume in the near field than, for instance, that achieved by [22]. Paper II.

In the case of the realistic model simulation, wind mixing overpowered the local mixing, thereby avoiding the creation of the barrier region [7, 11]. The density-driven and wind-forced background currents restricted the development of a plume coastal current and pushed the river bulge offshore. As a result, the bulge center was further away from the coast. Paper II.

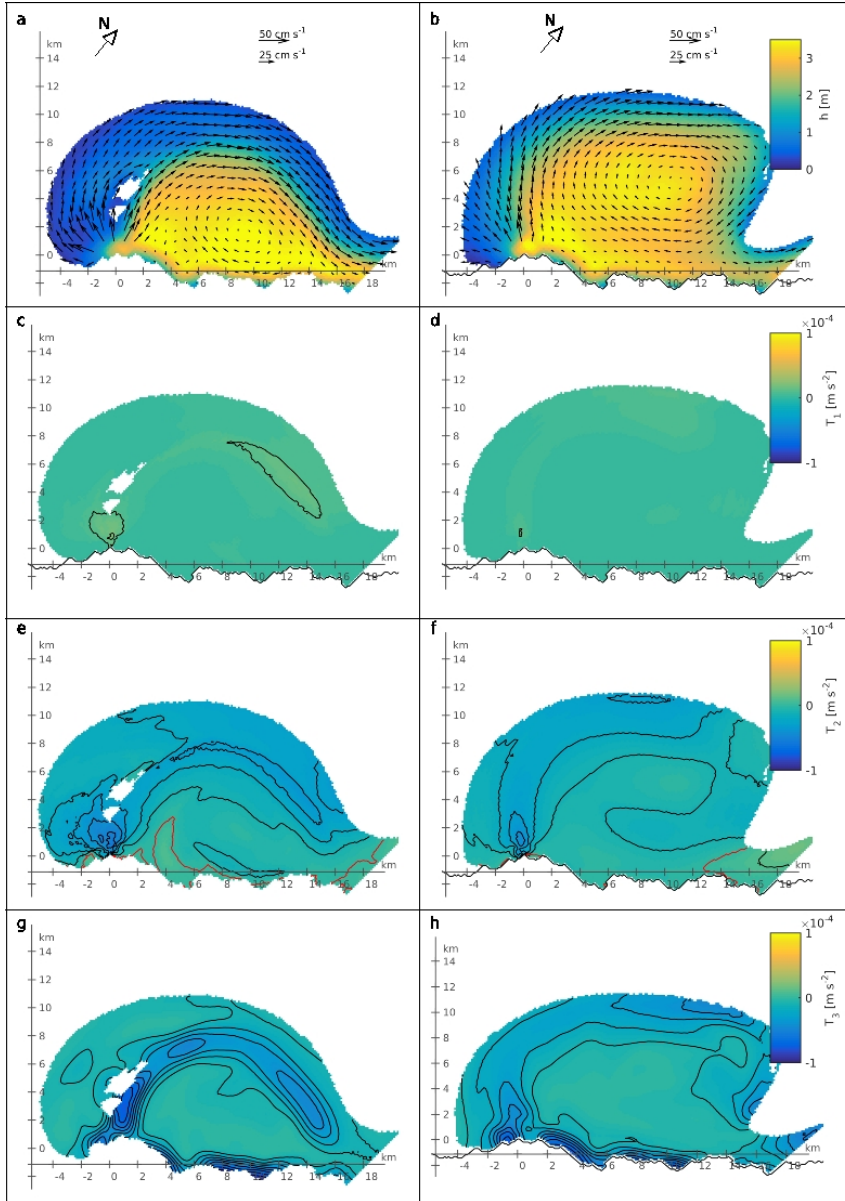


Figure 8: Bulge depth and depth averaged velocities, the terms ( $T_1$ ,  $T_2$ ,  $T_3$ ) of the balance (see Eq. 4) for idealized (left column) and realistic (right column) model simulations on 29 March 2007 at 20:00. Bulge depth and depth averaged velocities (a-b), centrifugal term ( $T_1$ ) (c-d), Coriolis term ( $T_2$ ) (e-f), pressure gradient term ( $T_3$ ) (g-h). The contour interval is  $1 \text{ m s}^{-2}$ . The red isoline represents zero. The blank area within the bulge is where the tracer concentrations were below the threshold values of the bulge definition. The origin of the coordinate system is at the mouth of the Daugava River. True north is shown with the arrow. Adapted from Paper II.

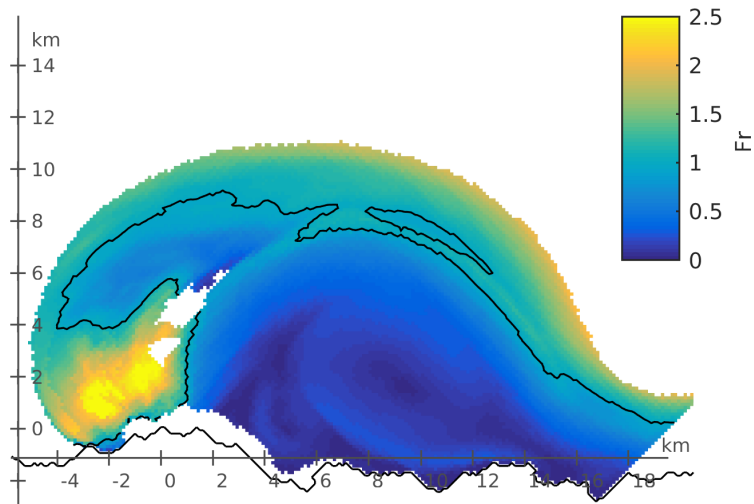


Figure 9: Idealized bulge Froude number. The blank area within the bulge is where the trace concentrations were below the threshold values of the bulge definition. The origin of the coordinate system is at the mouth of Daugava River.

### 3.4 Background circulation in the GoR.

The background circulation plays significant role in transporting the river water over the large area (Figure 5). Ten year numerical simulation data for the GoR was studied to map dominant circulation patterns during high river runoff period, i.e. March-June. Data for the GoR area was extracted from the Baltic Sea simulation with GETM setup (Paper III).

The PCA analyzes was used to obtain dominant circulation schemes in the surface layer of the GoR (Figure 10) during the spring from March to June. The first three modes explain 43 %, 14 % and 10 % of the total variability in the model, respectively. The first circulation mode is a double gyre with the anticyclonic/cyclonic gyre in the southeastern and cyclonic/anticyclonic gyre in the northwestern part of the GoR (Figure 10a). This pattern corresponds to the classical wind-forced double gyre circulation scheme in large lakes [7]. Due to shallowness of the GoR, double-gyre wind-driven circulation is readily excited in the GoR [41, 42]. The second mode has strong coastal current along the east coast (Figure 10b). The third mode consist of a large gyre covering most of the GoR with a smaller gyre/loop in the north (Figure 10c). Paper III).

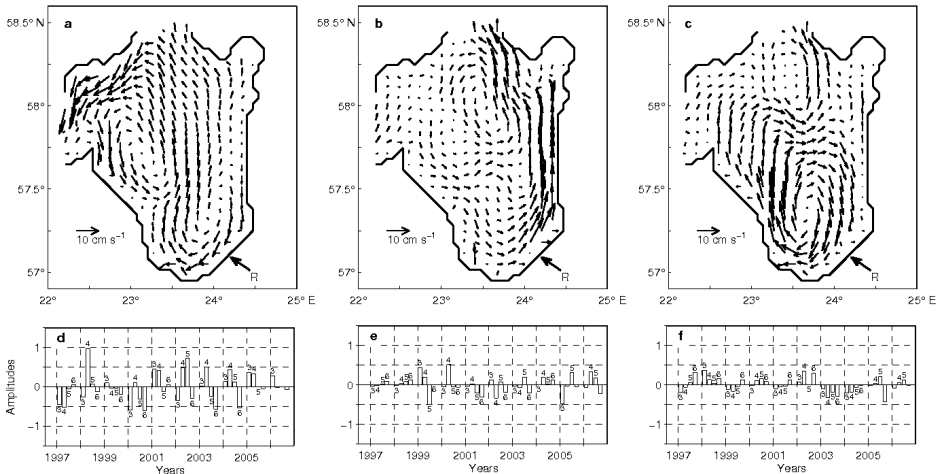


Figure 10: Circulation modes at 5 m depth from PCA for 40 month data (March-June from 1997 to 2006). First (a), second (b) and third (c) circulation mode. Corresponding amplitudes (d)-(f). Paper III.

The corresponding amplitudes show that all three modes occur almost as often with positive amplitude as with negative (i.e. vectors directed opposite, Figure 10 d, e, f). Rotation patterns were studied further by looking at the monthly mean relative vorticity for the southern part of the

GoR. For forty (40) studied spring months anticyclonic mean vorticity was clearly dominant. Paper III.

The main possible forcing factors for the GoR anticyclonic circulation are wind, spacial density gradients, freshwater discharge from the river(s) and water exchange with the Baltic Sea. A simplified numerical simulation for the GoR area was developed from the 10-year Baltic Sea numerical simulation. We focused on April 1998 when anticyclonic gyre was strongly present. Comparison of monthly mean circulations with open and closed boundary conditions show only minor differences. Hence using closed boundary conditions for the GoR was a reasonable simplification when studying processes in the time frame of couple of months. Paper III.

The first simulation was made with 3-dimensional density stratification without wind and river forcing. Monthly mean circulation shows anticyclonic circulation over the entire southern GoR reaching up to 57.75°N and a cyclonic loop in the northern part of the gulf (Figure 11a). Paper III.

The second simulation was made with wind forcing, uniform ambient density and without river discharge. Monthly mean circulation was double-gyre with an anticyclonic loop in the south-eastern part and cyclonic gyre over the central and north-west part of the GoR (Figure 11b). Wind in April 1998 was mainly from the east and northeast. Paper III.

The third simulation was made with river discharge, uniform ambient density and without wind. The monthly mean circulation pattern was similar to the discharge along the straight wall with an expanding bulge and coastal current (Figure 11c). Paper III.

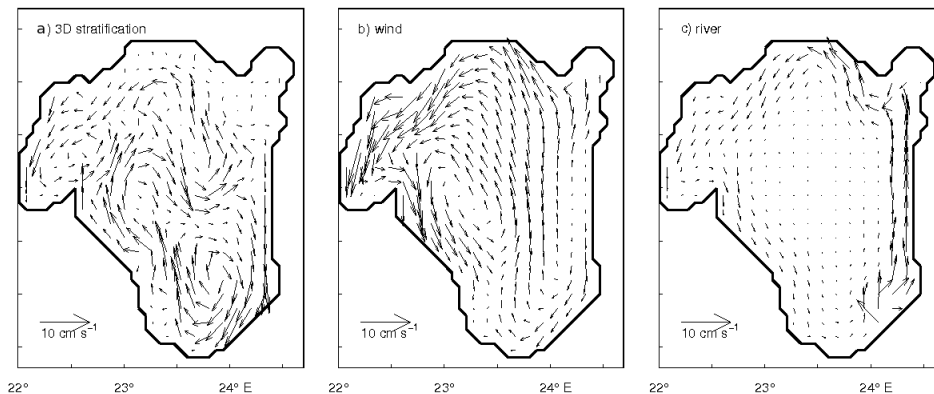


Figure 11: Monthly mean velocity patterns at 5 m depth (in April 1998) from the idealized simulations. a) 3-d density gradient forcing, b) wind forcing from March and April 1998 c) river discharge forcing from from March and April 1998.(g)-(e). Paper III

The monthly mean values of PEA, river discharge,  $Q$ , wind mixing, monthly accumulated salt flux through transect in the Irbe Strait east-west and north-south components of monthly accumulated wind impulse and density difference between the northwestern and southeastern GoR, were considered as potential factors influencing circulation. A multiple regression model for the dependent variable of vertically averaged vorticity showed that main factors were the east-west wind impulse and spacial density difference. Paper III.

Taking into account potential forcing mechanisms and calculated monthly mean spatially averaged relative vorticity, we may conclude that there is asymmetry in the realization of either cyclonic or anticyclonic circulation in the southern GoR. The present study shows that negative mean vorticity is more frequent in the southern GoR than a positive one. A relatively strong positive eastwest monthly accumulated wind impulse is needed to reverse anticyclonic circulation in the southern GoR. Paper III.

Most previous studies assume that with little or no wind forcing river water will spread along the right hand coast [55, 18, 5, 22, 23, 10, 25, 24], which is the case when ambient water density is homogeneous. The present study supplements the common understanding of river water circulation by taking into account anticyclonic circulation caused by three-dimensional density stratification that transports river water to the left and offshore from the river mouth. We can conclude that the main cause for the anticyclonic circulation in the GoR is a three-dimensional estuarine type density gradient and formation of an ambient anticyclonic circulation is driven by a combination of two mechanisms Paper III. Either by upward entrainment of lower layer water into the upper layer [19] due to continuous inflow of saline water into the estuarine basin, or by baroclinic geostrophic adjustment [53] in the case of an event like the supply of saline water. A numerical model study by Andrejev et al. (2010) [2] for the Gulf of Finland shows anticyclonic circulation forming near the Neva River mouth and fresher water being partly transported along the left hand coast.

## 4 Conclusions

The present thesis investigated the evolution and dynamics of the buoyant river bulge in the coastal sea and the circulation in the head of the gulf type ROFI, which affects the spreading of river water. The study is based on data from laboratory experiments and numerical model simulation in laboratory scale and remote sensing data and numerical simulations in the GoR.

The main conclusions of this work are listed below:

- Satellite images showed a clearly formed river bulge from the Daugava River discharge during the studied low wind period and confirmed anti-cyclonic rotation inside the bulge.
- A radial growth of the bulge in laboratory scale experiments and in natural conditions scales with bulge Rossby radius. The bulge growth rate was estimate from  $t^{0.28}$  to  $t^{0.50}$ . This is in good agreement with previous studies.
- A bulge spreading can be split into two phases. First an initial rapid spreading phase, when surface advective bulge forms, lasts 0.3-1.0 rotation periods. Then the spreading slows down and the growth continues on steadily until the bulge is dispersed by external forcing. The shift from first to second phase coincides with time when coastal current forms.
- While previous studies conclude that mid-field bulge region is governed by a balance between centrifugal, Coriolis and pressure gradient terms, our study showed that geostrophic balance is valid for the entire mid-field of the bulge.
- The ideal numerical model simulation showed that in the case of a high inflow Rossby number, the river inflow might split into two jets in the plume near-field region, with a strong mixing zone in-between.
- When setting up numerical simulations with inlet basins, inflow Kelvin number must be considered. Simulations with inlet basins give good estimates of bulge offshore spreading when the Kelvin number is close to one. When Kelvin number is larger/smaller, then the model underestimates/overestimates the bulge offshore reach.
- Monthly mean circulations in the southern part of the GoR in spring show strong asymmetry toward the anticyclonic circulation.
- The main cause for the anticyclonic circulation in the GoR is a three-dimensional estuarine type density gradient. Formation of an ambient

anticyclonic circulation is driven by a combination of two mechanisms. Either by upward entrainment of lower layer water into the upper layer due to continuous inflow of saline water into the estuarine basin, or by baroclinic geostrophic adjustment in the case of an event like the supply of saline water.

## References

- [1] BSHC (Baltic Sea Hydrographic Commission). Baltic Sea Bathymetry Database version 0.9.3., 2013.
- [2] O. Andrejev, A. Sokolov, T. Soomere, R. Värvi, and B. Viikmäe. The use of high-resolution bathymetry for circulation modelling in the gulf of finland. *Est. J. Eng.*, 16:187210, 2010.
- [3] A. Arakawa and V. R. Lamb. Computational design of the basic dynamical processes of the UCLA general circulation model. *Meth. Comput. Phys.*, 17:173263, 1977.
- [4] J. Attila, S. Koponen, K. Kallio, A. Lindfors, S. Kaitala, and P. Ylöstalo. MERIS Case II water processor comparison on coastal sites of the northern Baltic Sea. *Remote Sensing of Environment*, 128:138–149, 2013.
- [5] G. Avicola and P. Huq. The characteristics of the recirculating bulge region in coastal buoyant outflows. *Journal of Marine Research*, 61(4):435–463(29), 2003.
- [6] J. M. Beltrn-Abaunza, S. Kratzer, and C. Brockmann. Evaluation of MERIS products from Baltic Sea coastal waters rich in CDOM. *Ocean Sci.*, 10:377396, 2014.
- [7] J. Bennett. On the dynamics of wind-driven lake currents. *J. Phys. Oceanogr.*, 4:400414, 1974.
- [8] H. Burchard and K. Bolding. GETM - a general estuarine transport model. Scientific documentation. *Technical Report EUR 20253 EN, European Commission*, 2002.
- [9] H. Burchard and H. Rennau. Comparative quantification of physically and numerically induced mixing in ocean models. *Ocean Modelling*, 20(3):293311, 2008.
- [10] R. Chant, J. Wilkin, W. Zhang, B.-J. Choi, E. Hunter, R. Castelao, S. Glenn, J. Jurisa, O. Schofield, R. Houghton, J. Kohut, T. Frazer, and M. Moline. Dispersal of the Hudson River plume in the New York Bight: Synthesis of observational and numerical studies during LaTTE. *Oceanography*, 21(4):148161, 2008.
- [11] B. Choi and J. Wilkin. The effect of wind on the dispersal of the Hudson River plume. *J. Phys. Oceanogr.*, 37:18781897, 2007.

- [12] D. P. Dee, S. M. Uppala, A. J. Simmons, P. Berrisford, P. Poli, S. Kobayashi, U. Andrae, M. A. Balmaseda, G. Balsamo, P. Bauer, P. Bechtold, A. C. M. Beljaars, L. van de Berg, J. Bidlot, N. Bormann, C. Delsol, R. Dragani, M. Fuentes, A. J. Geer, L. Haimberger, S. B. Healy, H. Hersbach, E. V. Holm, L. Isaksen, P. Kallberg, M. Köhler, M. Matricardi, A. P. McNally, B. M. Monge-Sanz, J.-J. Morcrette, B.-K. Park, C. Peubey, P. de Rosnay, C. Tavolato, J.-N. Thepaut, and F. Vitart. ERA-Interim reanalysis: configuration and performance of the data assimilation system. *J. Roy. Meteor. Soc.*, 137:553597, 2011.
- [13] R. Doerffer and H. Schiller. The MERIS case 2 water algorithm. *International Journal of Remote Sensing*, 28(3-4):517–535, 2007.
- [14] R. Doerffer and H. Schiller. MERIS Regional Coastal and Lake Case 2 Water Project atmospheric correction ATBD (Algorithm Theoretical Basis Document). *International Journal of Remote Sensing*, 1.0, 41:41, 2008.
- [15] R. Döscher, U. Willen, C. Jones, A. Rutgersson, H. Meier, U. Hansson, and L. Graham. The development of the regional coupled ocean-atmosphere model RCAO. *Boreal Environ. Res.*, 7:183192, 2002.
- [16] R. Döscher, K. Wyser, H. Meier, M. Qian, and R. Redler. Quantifying arctic contributions to climate predictability in a regional coupled ocean-ice-atmosphere model. *Clim. Dyn.*, 34:11571176, 2010.
- [17] B. Dzwonkowski and X. Yan. Tracking of a Chesapeake Bay estuarine outflow plume with satellite-based ocean color data. *Continental Shelf Research*, 25(16):1942–1958, 2005.
- [18] D. Fong and W. Geyer. The Alongshore Transport of Freshwater in a Surface-Trapped River Plume. *J. Phys. Oceanog.*, 32:957–972, 2002.
- [19] T. Fujiwara, L. Sanford, K. Nakatsujic, and Y. Sugiyama. Anticyclonic circulation driven by the estuarine circulation in a gulf type ROFI. *Journal of Marine Systems*, 12:83–99, 1997.
- [20] A. A. Gitelson, D. Gurlin, W. J. Moses, , and T. Barrow. A biooptical algorithm for the remote estimation of the chlorophyll-a concentration in case 2 waters. *Environ. Res. Lett.*, 4:045003, 2009.
- [21] S. Gregorioa, D. Haidvogelb, P. Thomasa, E. Taskinogluc, and A. Skeend. Laboratory and numerical simulations of gravity-driven coastal currents: Departures from geostrophic theory. *Dynamics of Atmospheres and Oceans*, 52:20–50, 2011.

- [22] R. D. Hetland and R. Signell. Modelling coastal current transport in the gulf of Maine. *Deep-Sea Res. II*, 52:2430–2449, 2005.
- [23] A. Horner-Devine. Velocity, density, and transport measurements in rotating, stratified flows. *Experiments in Fluids online*, pages 1–13, 2006.
- [24] A. Horner-Devine. The bulge circulation in the Columbia River plume. *Cont. Shelf Res.*, 29:234–251, 2009.
- [25] A. Horner-Devine, D. Fong, and S. Monismith. Evidence for the inherent unsteadiness of a river plume: Satellite observations of the niagara river discharge. *Limnol. Oceanogr.*, 53:2731–2737, 2008.
- [26] A. Horner-Devine, R. Hetland, and D. MacDonald. Mixing and transport in coastal river plumes. *Annual Review of Fluid Mechanics*, 47:569–594, 2015.
- [27] P. Huq. The role of kelvin number on bulge formation from estuarine buoyant outflows. *Estuaries and Coasts*, 32:709–719, 2009.
- [28] F. Janssen, C. Schrum, and J. Backhaus. A climatological dataset of temperature and salinity for the north sea and the baltic sea. *Ger. J. Hydrogr.*, 9:1245, 1999.
- [29] J. Jurisa and R. Chant. The coupled hudson river estuarine-plume response to variable wind and river forcings. *Ocean Dyn.*, 62:771–784, 2012.
- [30] M. Keruss and J. Sennikovs. Determination of tides in Gulf of Riga and Baltic Sea. *Proc. International Scientific Colloquium 'Modelling of Material Processing', Riga, May 28 - 29, 1999*, 1999.
- [31] K. Klingbeil, M. Mohammadi-Aragh, U. Gräwe, and H. Burchard. Quantification of spurious dissipation and mixing discrete variance decay in a finite-volume frame-work. *Ocean Model.*, 81:49–64, 2014.
- [32] G. Lindström, F. Janssen, C. Schrum, and J. Backhaus. Development and testing of the HYPE (Hydrological Predictions for the Environment) water quality model for different spatial scales. *Hydrol. Res.*, 41:295319, 2010.
- [33] U. Lips, V. Zhurbas, M. Skudra, and G. Väli. A numerical study of circulation in the Gulf of Riga, Baltic Sea. part i: Whole-basin gyres and mean currents. *Cont. Shelf Res.*, 112:1–13, 2016.
- [34] V. Malačič and P. Petelin. Climatic circulation in the Gulf of Trieste (northern adriatic). *J. Geophys. Res.Oceans*, 114, 2009.

- [35] I. Maljutenko and U. Raudsepp. Validation of GETM model simulated long-term salinity fields in the pathway of saltwater transport in response to the major baltic inflows in the baltic sea. *IEEE/OES Baltic International Symposium (BALTIC)*, 2014.
- [36] T. McClimans, D. Johnson, M. Krosshavn, S. King, J. Carroll, and O. Grenness. Transport processes in the Kara Sea. *J. Geophys. Res.Oceans*, 105 (14):12114, 2000.
- [37] D. Nof and T. Pichevin. The ballooning of outflows. *J. of Phys. Oceanogr.*, 31:3045–3058, 2001.
- [38] J. Pan, Y. Gu, , and D. Wang. Observations and numerical modeling of the Pearl River plume in summer season. *J. Geophys. Res.- Oceans*, 119:24802500, 2014.
- [39] G. Pantelev, A. Proshutinsky, M. Kulakov, D. Nechaev, and W. Maslowski. Investigation of the summer Kara Sea circulation employing a variational data assimilation technique. *J. Geophys. Res.Oceans*, 112, 2007.
- [40] J. Pietrzak. The use of TVD limiters for forward-in-time upstream-biased advection schemes in ocean modeling. *Mon. Weather Rev.*, 126:812–830, 1998.
- [41] U. Raudsepp. Interannual and seasonal temperature and salinity variations in the Gulf of Riga and corresponding saline water inflow from the Baltic Proper. *Nordic Hydrology*, 33 (2):135–160, 2001.
- [42] U. Raudsepp, D. Beletsky, and D. Schwab. Basin-scale topographic waves in the Gulf of Riga. *J. Phys. Oceanogr.*, 33:11291140, 2003.
- [43] A. Shchepetkinm and J. McWilliams. TA method for computing horizontal pressuregradient force in an oceanic model with a nonaligned vertical coordinate. *J. Geophys. Res.*, 108:3090, 2003.
- [44] A. Shchepetkinm and J. McWilliams. The regional oceanic modeling system (ROMS): a split-explicit, free-surface, topographically-following-coordinate oceanic model. *Ocean Modelling*, 9:347–404, 2005.
- [45] L. Siitam, L. Sipelgas, and R. Uiboupin. Analysis of natural background and dredging-induced changes in TSM concentration from MERIS images near commercial harbours in the Estonian coastal sea. *J. Remote Sens.*, 35:67646780, 2014.
- [46] J. H. Simpson. Physical processes in the ROFI regime. *Journal of Marine Systems*, 12:3–15, 1997.

- [47] T. Stipa, T. Tamminen, and J. Seppälä. On the creation and maintenance of stratification in the Gulf of Riga. *Journal of Marine Systems*, 23(1-3):27–49, 1999.
- [48] A. Stips, K. Bolding, T. Pohlmann, and H. Burchard. Simulating the temporal and spatial dynamics of the North Sea using the new model GETM (general estuarine transport model). *Ocean Dyn*, 54 (2):266–283, 2004.
- [49] P. J. Thomas and P. F. Linden. Rotating gravity currents: small scale and large-scale laboratory experiments and a geostrophic model. *J. Fluid Mech.*, 578:3565, 2007.
- [50] L. Umlauf and H. Burchard. Second-order turbulence closure models for geophysical boundary layers. a review of recent work. *Cont. Shelf Res.*, 2:795827, 2005.
- [51] D. Vaicute, M. Bresciani, and M. Bucas. Validation of MERIS Bio-Optical Products with In Situ Data in the Turbid Lithuanian Baltic Sea Coastal Waters. *J. Appl. Remote Sens.*, 6:063568–1–063568–20, 2012.
- [52] A. Valente and J. Silva. On the observability of the fortnightly cycle of the Tagus estuary turbid plume using MODIS ocean colour images. *Journal of Marine Systems*, 75(1-2):131–137, 2009.
- [53] G. Wake, G. Ivey, J. Imberger, N. McDonald, and R. Stocker. Baroclinic geostrophic adjustment in a rotating circular basin. *Journal of Fluid Mechanics*, 515:63–86, 2004.
- [54] M. Whitney and R. Garvine. Wind influence on a coastal buoyant outflow. *J. Geophys. Res.*, 110(C3), 2005.
- [55] A. Yankovsky and D. Chapman. A simple theory for the fate of buoyant coastal discharges. *J. of Phys. Oceanogr.*, 27:1386–1401, 1997.
- [56] Y. Yuan, M. Avenier, and A. Horner-Devine. A two-color optical thickness method for determining layer depth in two interacting buoyant plumes. *Exp. Fluids.*, 50:5:1235–1245, 2011.



## **Publication I**

Soosaar, E., Hetland, R.D., Horner-Devine, A., Avenir, M. E. and Raudsepp, U. (2014). Offshore spreading of buoyant bulge from numerical simulations and laboratory experiments. 2014 IEEE/OES Baltic International Symposium. DOI: 10.1109/BALTIC.2014.6887889



# Offshore spreading of buoyant bulge from numerical simulations and laboratory experiments

Edith Soosaar<sup>1</sup>, Robert D. Hetland<sup>2</sup>, Alexander Horner-Devine<sup>3</sup>, Margaret E. Avenier<sup>3</sup>, Urmas Raudsepp<sup>1</sup>

1) Marine Systems Institute at Tallinn University of Technology, Akadeemia tee 15a, 12618 Tallinn, Estonia  
Edith Soosaar (corresponding author). Phone: (372) 6204307, Fax: (372) 6204301, email: edith.soosaar@msi.ttu.ee

2) Department of Oceanography, Texas A&M University, College Station, TX 77843-3146, USA.

3) Department of Civil and Environmental Engineering, University of Washington, Seattle, WA 98195-2700.

## Abstract

The ability of a three-dimensional hydrodynamic model to reproduce buoyant water entering a coastal sea at laboratory scales of  $O[1 \text{ cm}]$  is studied using Regional Ocean Modeling System (ROMS). ROMS is typically used for geophysical scale simulations. Inflowing water forms a growing anti-cyclonic buoyant bulge and coastal current. Available laboratory data is from a rotating circular basin experiment. The numerical domain is a rectangular basin with three open boundaries and a straight inflow channel for freshwater discharge. Altogether 11 pairs of laboratory-numerical simulation runs are analyzed. Three additional simulations are made to study the influence of ambient salinity. Rotation rate, ambient salinity and inflow rate- including oscillatory inflow as a proxy for tides, is varied. The present study concentrates on comparison of the bulge offshore front.

Development of a bulge and downcoast coastal current was observed in all experiments. Two phases of bulge spreading are identified. An initial rapid spreading phase lasts 0.3-0.7 rotation periods and a following slow expansion that lasts until the end of the simulation. The shift from first phase to second coincides with the formation of the coastal current. Bulge front spreading agrees well with inflow Kelvin number  $K \sim O(1)$ . When  $K > 1/K < 1$ , the model underestimates/overestimates the bulge offshore reach. Physical processes of discharged water are altered in the inflow estuary before the water enters the main basin. With estuary wide/narrow in comparison to the deformation radius resulting with non-uniform outflow profile. These differences however do not notably alter the spreading during the second phase. Bulge front spreading is scaled with various non-dimensional parameters and best scaling is achieved during the first phase for laboratory simulation with internal radius and numerical bulge spreading with the bulge Rossby radius. During the second phase both scale with with the bulge Rossby radius. The numerical bulge expands at a steady rate of  $0.10 \text{ cm s}^{-1}$  and laboratory bulge at  $0.11 \text{ cm s}^{-1}$ .

**Keywords:** River plumes, buoyancy driven flow, rotating tank, hydrodynamic model, laboratory scale numerical simulation

## INTRODUCTION

Buoyant water entering a coastal ocean typically forms a buoyant plume that consists of a large, surface-trapped, anti-cyclonically rotating bulge and a coastal current in the coastally trapped wave direction (from here on referred to as the coastal current) [6, 7]. The rotating bulge is a prominent feature in rotating tank experiments and numerical simulations [7, 3, 23, 18, 12, 21]. Observational studies confirm that the bulge is a naturally occurring phenomena, examples of observed anti-cyclonic bulges include the Hudson river plume [2], Niagara River plume [13] and Columbia River Plume [14,16]. Fong and Geyer (2002)[5] suggested that depending on the Rossby number, the amount of the fresh water accumulating in the bulge ranges from 30-75%. Nof and Pichevin 2001 [18] concluded that intense outflow (large Rossby number) dumps up to 66% of its mass flux into the growing bulge.

Multiple numerical and laboratory simulations estimate bulge and coastal current width, thickness and spreading velocity [1, 4, and 21]. A study by Gregorio et. al 2011 [8] used ROMS to reproduce buoyant a plume with reasonable agreement. However they also focus on coastal current formation and dynamics. Most research now agrees that the rotating part of the plume i.e. the bulge is in gradient wind balance (also called cyclostrophic wind balance) [23, 12, 14]. Horner-Davine 2006 [12] developed a conceptual model to describe bulge spreading based on a combination of internal radius and bulge Rossby radius. The dynamics is described by bulge effective radius and offshore displacement of the bulge center scaled with the internal Rossby radius and

inertial radius accordingly. Yankovsky and Chapman (1997) [23] assumed steady state flow but Nof and Pichevin 2001 [18] suggest that a steady-state is not possible. This was later confirmed by laboratory experiments by Horner-Devine et al. 2006 [12] and Avicola and Huq (2003) [1] who concluded that steadiness may not be valid in many cases. Also satellite observations for Niagara River discharge confirm unsteadiness of the plume [13]. During the first 1-2 rotation periods the bulge fills and forms, radial acceleration associated with bulge growth is an important contribution to the momentum balance. After the initial phase, the bulge is expected to maintain a quasi-steady momentum balance involving only the terms in the gradient-wind balance.

River plume dynamics is relatively well understood however most studies concentrate on bulge spreading after the initial spin-up when the bulge and coastal current have already formed but the momentum of the river discharge is still a considerable influence. The initial spin-up phase hasn't received much attention. Most studies ignore it and just look at the longer term evolution; however, plumes in nature are constantly being modified by the wind and "reset". Numerical simulation of bulge offshore spreading velocity by Avicola and Huq [1] (Fig 3B) show initial rapid increase and then slowing down notably. The same is observed in laboratory simulations by HD2000 [11].

An aim of this paper is to study formation and spreading of the circulating buoyant bulge with a focus on offshore front velocity. Bulge spreading is split into two phases, initial fast expansion phase and slower steady expansion phase. After initial formation, the recirculating bulge keeps growing. We attempt to determine non-dimensional scaling parameters for the two phases to separate dominant processes. Another purpose of this study is to test the model's ability to reproduce laboratory scale ( $O(1\text{cm})$ ) experiments. Altogether eleven laboratory-numerical simulation pairs are compared. Additional three model simulations are made to study bulge sensitivity to increased ambient water salinity. Available simulations have a wide range of Froude numbers to test the model with various ratios of inertial and gravitational forcing.

## METHODS

### 1. Laboratory experiments

Laboratory experiments were carried out on a rotating table in the University of Washington's Harris Hydraulics Laboratory (Fig. 1). An annular tank (inner radius = 22 cm, outer radius = 92 cm) was placed on top of the table and filled to a depth of 20 cm with salt water (salinity = 1-5  $\text{g kg}^{-1}$  depending on the experiment). A vertical Plexiglas sheet in the tank simulated a steep coastal wall. The table was brought to a rotation rate of  $\Omega$  and spun up at that rate for 60 minutes. After spin-up, fresh water was pumped onto the surface of the salt water layer from a storage container below the tank. The fresh water was dyed red with food dye, and entered the tank through an inlet 1 cm deep and 5 cm wide in the coastal wall. A fine sponge in the inlet diffused the inflow to achieve a uniform velocity profile. For periodic discharge runs the voltage input to the pump was varied such that the flow rate into the tank was approximately sinusoidal. The rotating tank and river plume configuration is described in detail in [12, 24].

The area of interest in the tank was illuminated from below with an edge-lit LED light panel and videotaped from above with a co-rotating video camera. Upon completion of a run, the video was captured on a computer and saved at one frame per second. Images were processed using the optical thickness method [10, 24], from which the depth of the fresh water layer was

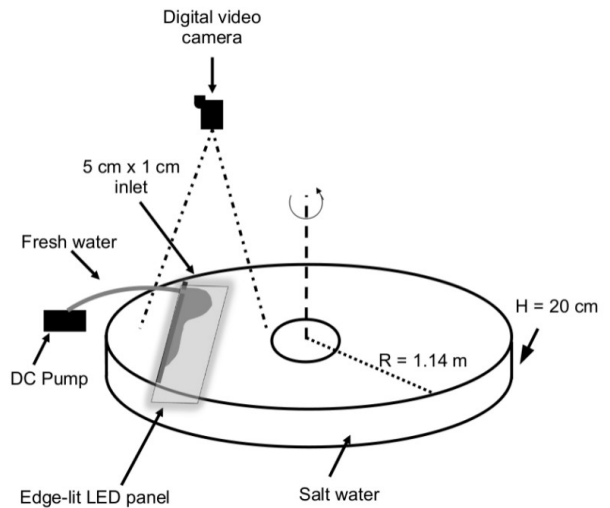
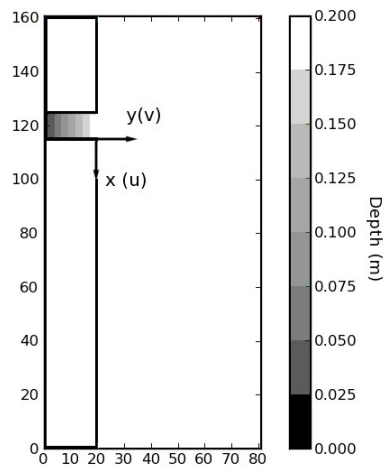


Fig.1 Sketch of the laboratory experimental setup. Rotating table with radius  $R = 1.14$  m and constant depth  $H = 20$  cm. Monitored model domain is marked with light gray rectangle. Colored fresh water is injected to the ambient salty water through 5x1 cm inlet trough gap in vertical Plexiglas wall imitating coastal wall in 'western' direction.

calculated at each pixel. The result is a 1 Hz sequence of whole plume fields of fresh water thickness. It is important to note, however, that the optical thickness method cannot differentiate between layer thickness and concentration. It measures the product of those two. Thus, no information is directly available about plume mixing.

## 2. Numerical model setup

ROMS is a three-dimensional, hydrostatic, primitive-equation ocean model that uses a split-explicit scheme to solve for a free surface [18]. The model domain is a rectangular basin with a coastal wall and three open boundaries (Fig. 2). No-gradient open boundary conditions are used for the open boundaries. The basin size is 80x30 cm (160x60 grid points) with a constant depth of 20 cm. The model's horizontal resolution is  $\Delta x = \Delta y = 0.5$  cm with 30 levels in a vertically stretched  $s$ -coordinate. The model resolution was chosen to find the optimal balance between the computational power and resolution needed to reasonably resolve the features in the buoyant plume. In the present study, the vertical grid is focused near the surface. The smallest vertical resolution is 0.21 cm at the surface layer ( $\theta_s=3$ ,  $\theta_b=0.4$ ). The effect of the tank's rotation is included through the Coriolis parameter. Tides are simulated in a similar way to the method used in the laboratory simulation, i.e. by sinusoidally changing fresh water inflow value. A river inlet is added through a straight inlet basin in the "western" wall. The inlet basin is 10 cm long and has a bottom slope from 1 to 20 cm (the study domain region has a constant flat bottom). Fresh water is added from 10 point sources (inflow total width 5 cm) at the end of the basin to imitate laboratory inlet conditions. In the laboratory simulation a sponge was used in front of the inflow to create a uniform velocity profile. In the numerical simulation the inlet basin is used to achieve this. Early studies showed that using a slope in the inlet caused water to spread more uniformly at the surface and enter the surface layer domain resembling the 1 cm diffused inflow in the laboratory setup. Some studies [18, 7] recommend introducing a weak, ambient, downcoast flow to avoid the formation of an upcoast propagation of the fresh water bulge. In the current numerical simulations the structure of the bulge is mostly stable over the time period required to make a comparison with the laboratory results. Therefore in order to better match the laboratory conditions an ambient current is not used.



**Fig. 2 Plan view of numerical model study domain. Study area size 30x80 cm with uniform 20 cm depth. Inlet basin with sloping bottom located in the 'western' wall. Fresh water is introduced to the system through the inlet basin. Offshore direction is toward  $y$  and downcoast direction is toward  $x$ .  $u$  and  $v$  are velocities in the according direction.**

Initial background salinity and temperature used in the basin are constant. A temperature of  $T_0 = 20$  °C is used for all runs while background salinity,  $S_0$ , is modified. Fresh water is introduced through the inlet basin in the coastal wall, and is a source of both mass and momentum. The inlet basin is 10 grid steps long and located in the range of 60-65 cm from the downcoast boundary and 10 cm from the upcoast boundary. The salinity of inflowing water is 0 g kg<sup>-1</sup> and the temperature is identical to the background temperature for all runs. The fresh water inlet is confined to the upper four layers (approximately 1 cm), so that the inlet source is 5 cm wide and 1 cm deep, which is the same size as the inlet used in the laboratory experiment.

Recursive MPDATA advection of tracers and quadratic bottom friction are used in the simulations. Horizontal viscosity as well as horizontal diffusivity is set to zero for all runs.  $k$ - $\epsilon$  turbulent closure scheme with horizontal smoothing of buoyancy/shear and Canuto A-stability function formulation are used for vertical mixing of momentum and tracers. The background vertical viscosity coefficient and vertical diffusion coefficient for salinity are set to  $10^{-6}$  m<sup>2</sup>s<sup>-1</sup> and  $5 \times 10^{-7}$  m<sup>2</sup> s<sup>-1</sup>, respectively. The turbulent kinetic energy background vertical mixing coefficients and the turbulent generic statistical field are  $5 \times 10^{-8}$  m<sup>2</sup> s<sup>-1</sup> and  $5 \times 10^{-9}$  m<sup>2</sup> s<sup>-1</sup>, respectively. Mass is lost through the open boundaries and gained from the source that represents the river inflow.

A total of 14 model simulations are performed by modifying: 1) the background salinity, 2) fresh water inflow rate, 3) tidal amplitude, and 4) rotation rate of the tank in order to reproduce laboratory experiments. Values of these parameters for each of the laboratory and numerical experiment pairs are shown in Table 1. Two additional simulations (runs 6 and 7) are made with no analog laboratory simulation.

**Table 1.** Experimental parameters of the ROMS simulation and laboratory experiment pairs. Run 4 and 7 do not have analogous laboratory experiments. The values listed are run number, rotation period,  $T$  [s], mean inflow rate  $Q$  [ $\text{cm}^3\text{s}^{-1}$ ], inflow amplitude,  $\Delta Q$  [ $\text{cm}^3\text{s}^{-1}$ ], ambient salinity,  $S_0$ , Kelvin number,  $K$ , minimum and maximum Rossby number,  $Ro$ , minimum and maximum Froude number,  $Fr$ ; minimum and maximum fractional depth,  $h/D$ .

<i>Run nr</i>	$T$ [s]	$Q$ [ $\text{cm}^3\text{s}^{-1}$ ]	$\Delta Q$ [ $\text{cm}^3\text{s}^{-1}$ ]	$S_0$ [ $\text{g kg}^{-1}$ ]	$K$	$Ro$ min	$Ro$ max	$Fr$ min	$Fr$ max	$h/D$ min	$h/D$ max	$R_d$
1	30	7,63	2,36	5	1,08	0,50	0,95	0,54	1,03	0,05	0,07	5,28
2	30	7,9	0	5	1,08	0,75	0,75	0,82	0,82	0,07	0,07	5,30
3	15	10,3	0	5	2,17	0,49	0,49	1,07	1,07	0,11	0,11	3,37
4	15	10,0	0	1	4,83	0,48	0,48	2,31	2,31	0,24	0,24	2,24
5	40	6,0	0	1	1,81	0,76	0,76	1,38	1,38	0,11	0,11	4,14
7	15	10,3	0	32	0,86	0,49	0,49	0,42	0,42	0,04	0,04	5,38
12	7,5	12,35	7,6	4,5	4,57	0,11	0,48	0,52	2,17	0,11	0,22	2,05
13	15	12,35	7,6	4,5	2,28	0,23	0,95	0,52	2,17	0,08	0,16	3,44
14	30	12,35	7,6	4,5	1,14	0,45	1,91	0,52	2,17	0,05	0,11	5,79
15	45	12,35	7,6	4,5	0,76	0,68	2,86	0,52	2,17	0,04	0,09	7,85
16	60	12,35	7,6	4,5	0,57	0,91	3,81	0,52	2,17	0,04	0,08	9,74
17	60	12,35	1,55	4,5	0,57	2,06	2,65	1,18	1,52	0,06	0,07	9,72
18	60	12,35	2,9	4,5	0,57	1,80	2,91	1,03	1,66	0,05	0,07	9,74
20	60	12,35	6,05	4,5	0,57	1,2	3,51	0,69	2,01	0,04	0,08	9,72

Simulations are set up so that fresh water forms surface advective plumes where bulge thickness,  $h$ , is much smaller than water depth  $D$ ,  $h_g/D < 0.25$ , where

$$h_g = \sqrt{\frac{2Qf}{g'}} \quad (1)$$

is depth scale (maximum geostrophic current depth) and  $D$  is ambient water depth [14].

### 3. Dimensionless parameters

A summary of the setup parameters and non-dimensional parameters for the numerical/laboratory experiment pairs is provided in Table 1. Setups are characterized by the inflow Rossby number ( $Ro$ ), Froude number ( $Fr$ ) and the inflow Kelvin number ( $K$ ). These parameters are defined mathematically as:

$$Ro = \frac{u}{Wf}, Fr = \frac{u}{g'H}, K = \frac{Wf}{\sqrt{g'H}} \quad (2)$$

where  $u$  is the bulk flow speed at the wall source calculated as  $u = Q(WH)^{-1}$ ,  $W$  is discharge width (5 cm),  $Q$  is flow rate,  $H$  is inflow thickness (1 cm),  $f$  is the Coriolis parameter,  $g' = g(\rho_0 - \rho_A)/\rho_0$  is reduced gravity,  $g$  is gravitational constant,  $\rho_0$  is fresh water density and  $\rho_A$  is ambient water density.

Discharge with Rossby number  $O(1)$  leaves most fresh water in the bulge, while with a low Rossby number, the amount of water going to coastal current increase [4]. Froude number of approximately unit value indicate that inertial and gravitational forces are in balance. Froude number under unit value indicate predominantly subcritical flow (buoyancy forcing dominates). As  $Fr < 1$  for most simulations in this study we are dealing with slow moving and possibly deep water. Kelvin number is the ratio of the width of the outflow to deformation radius, it indicates if discharge corresponds to narrow or wide estuary conditions.

## RESULTS

Fresh water thickness ( $fw_t$ ) is used to characterize the buoyant plume, calculated as:

$$fw_t = \int_D \frac{S_0 - S}{S_0} dz \quad (3)$$

where  $D$  is the depth of the domain,  $S$  is the salinity and  $S_0$  the salinity of ambient water. The bulge front is defined at  $fw_t = 0.1$  cm. Bulge offshore reach is calculated as front maximum reach toward  $y$  (Fig. 2).

Time evolution of the fresh water thickness distribution for the first numerical and laboratory simulations in Fig. 3 show that during  $0.5T$ , both laboratory and numerical plume fronts have spread 12-13 cm offshore, and some of the fresh water is beginning to be carried downcoast. The coastal current formation is faster for numerical than for laboratory simulation, the downcoast reach is  $\sim 10$  cm and  $\sim 2$  cm respectively. By the end of the first rotation period bulge and coastal current are formed for both studies. Numerical simulation areal extent and freshwater distribution match with laboratory analog. Differences in front location vary up to 10% in downcoast and up to 15% in the offshore directions. Differences in the distribution of freshwater inside the bulge are bigger but still reasonable.

From 2-8T, bulge expansion is slower but still steady for both experiments. The front location is reproduced with  $\sim 10\%$  accuracy until the end of 8T. Numerical simulation underestimates the width of the coastal current. Laboratory coastal current widens in time (at the end of the simulation up to 30 cm), while numerical study coastal current stay in the range of 5-10 cm throughout the simulation. Fwt distribution inside the bulge shows that in the numerical simulation more fresh water accumulates in the center of the bulge. The bulge center advances offshore during the simulation. In the laboratory simulation a bigger concentration of the fresh water is located near the discharge and along the coast. The bulge consists of shallow buoyant water expanding offshore. Estimating rotation inside the laboratory bulge is beyond the means of the present study.

Comparing run one and two indicates that turning off tidal modulation (proxy to tidal forcing) alters bulge spreading and water distribution very little (not shown). Varied inflow rate (Fig. 4a, runs 1, 2 and 14-20) alters numerical bulge spreading when the front retreats (20-40 seconds into a simulation). Inflow amplitude from runs 16-20 is modified from  $1.55$  to  $7.6 \text{ cm}^3 \text{ s}^{-1}$  while mean inflow rate  $Q$  is fixed to  $12.35 \text{ cm}^3 \text{ s}^{-1}$ . Bigger amplitude variation (run 16,  $\Delta Q = 7.6 \text{ cm}^3 \text{ s}^{-1}$ ) causes the front to retreat up to 5cm. Smaller amplitude variation (run 17,  $\Delta Q = 1.55 \text{ cm}^3 \text{ s}^{-1}$ ) causes the front to retreat up to 1cm. The retreating front is present only in numerical simulations.

The offshore spreading can be split into two distinct phases (Fig. 4). First, a short phase of front fast offshore spreading. Second, a slower steady advance of the bulge offshore front. These two phases can be identified in all numerical and laboratory simulations. The first phase is very short lasting up to 0.7 rotation periods, but in most simulations as little as 0.3 to 0.5 rotation periods. Also retreating front at runs 14-20 makes it difficult to pinpoint time of phase change (Fig. 4a). Model simulation first phase duration varies over simulations more than laboratory. Laboratory bulge development is more uniform in the studied parameter range. The first phase is finished within first ten seconds for all laboratory simulations. During first 20 seconds the offshore reach of the numerical bulges varies from 5-23 cm (Fig. 4a) while laboratory simulations the reach varies from 7-13 cm (Fig. 4b).

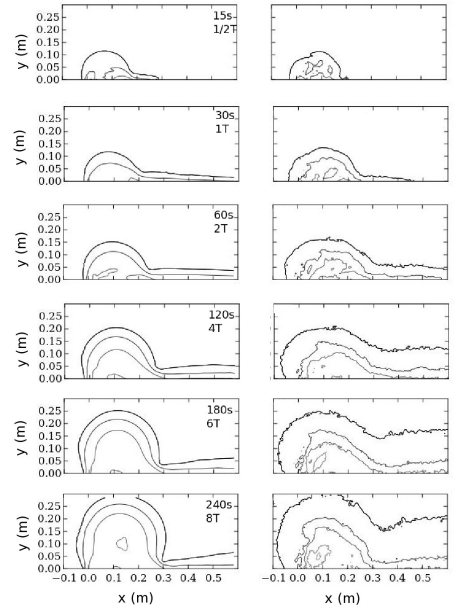


**Fig. 3** Time evolution of fresh water thickness ( $fw_t$ ) for numerical simulation run 1 (left column) and corresponding laboratory experiment (right column) (see Table 1) at time 1/6, 1/2, 1, 2, 4, 6, 8 T. Bold line is edge of fresh water area where  $fw_t = 0.1$  cm, contour interval is 0.5 cm.

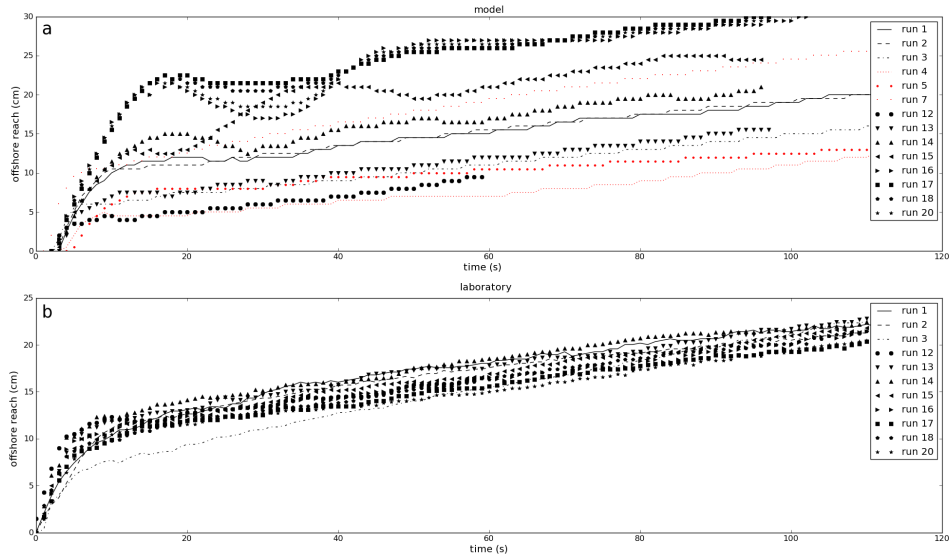


**Fig. 4** Bulge front maximum offshore reach over time for a) numerical model b) laboratory simulation. Runs 4, 5 and 7 are numerical simulations without laboratory equivalents.

The ending time of the first phase is estimated from front offshore spreading. The time of coastal current formation is estimated from fwt images. Both time scales are non-dimensionalized by rotation period,  $T$ . Comparing the two time scales shows a strong relationship between the end of the first phase and the formation of a coastal current (Fig. 5). A linear regression fit gives  $R^2=0.72$  for the numerical model but only  $R^2=0.3$  for the laboratory simulations. Thus during the second phase when the coastal current is well established, the offshore spreading of the bulge front is steady. For all the inflow parameters considered in this study the simulated bulge increases linearly during the second phase. Estimating laboratory and numerical simulations separately and fitting linear regression for all the results gives  $k=0.1108$  ( $R^2=0.87$ ,  $p<0.001$ ) and  $k=0.1036$  ( $R^2=0.79$ ,  $p<0.001$ ) accordingly.

To characterize bulge offshore spreading various parameters were tested. Best convergence was achieved

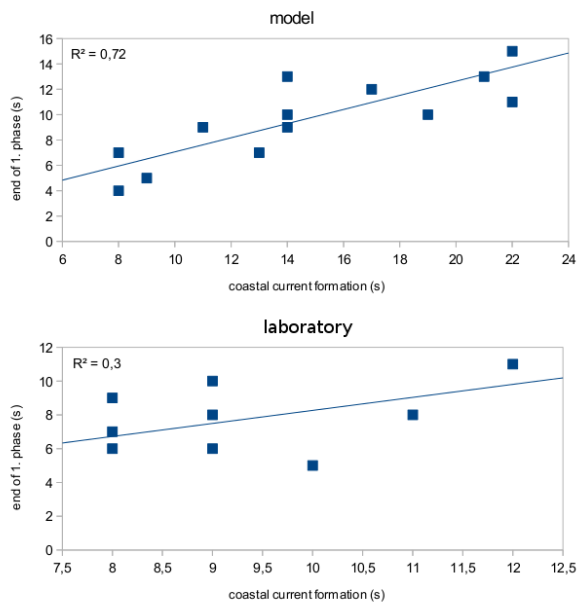


**Fig. 5.** End time of the first phase as a function of the coastal current formation time. Solid line is linear regression and  $R^2$  coefficient of determination.

with bulge internal radius and bulge Rossby radius:

$$L_i = \frac{U}{f}, \quad L_b = \left( \frac{2Qg'}{f^3} \right)^{1/4} \quad (4)$$

Time is non-dimensionalized by rotation period,  $T$ , and offshore spreading by bulge Rossby radius and internal radius (Fig. 6 and Fig. 7).

$$T_n = \frac{t}{T}, \quad W_b = \frac{x}{L_b}, \quad W_i = \frac{x}{L_i} \quad (5)$$

Studying all the simulations (laboratory and numerical separately) shows that during the first phase, the variance of bulge reach is minimal when normalized by internal radius for laboratory ( $R^2=0.76$ ) and bulge Rossby radius for numerical simulation ( $R^2=0.87$ ) (Fig. 6b and c). The difference between using  $L_b$  or  $L_i$  is small ( $R^2=0.73$  or  $0.76$  for numerical and  $R^2=0.84$  or  $0.87$  for laboratory simulations). During the second phase variance in  $y_f$  is minimal when normalized by the bulge Rossby radius for all simulations ( $R^2=0.89$  for laboratory and  $R^2=0.95$  for numerical simulations) (Fig. 7).

## DISCUSSION

In present experiments a freshwater plume forms an expanding buoyant bulge near the discharge, and a coastal current in the Kelvin wave direction. Both laboratory and numerical simulations show that the bulge spreads in two distinct phases. Similar behaviour is also present in simulations by Avicola and Huq 2003 ([1] Fig. 3). Our results indicate that the first rapid spreading phase lasts approximately, 0.3-0.7 rotation periods. The end of the numerical simulation first phase coincides with a coastal current formation. The laboratory simulation in the variable range studied shows very little dependence on rotation period. For laboratory simulations the phase shift takes place approximately at the same time and is only weakly connection coastal current formation time.

The differences between laboratory and numerical bulge spreading arise during the initial phase that causes numerical bulge spreading to vary in a wider range than for respective laboratory bulges. Difference arise due to the way the freshwater discharge is set up. In the laboratory experiments the water enters directly to the tank. Numerical simulations are set up using inlet basin. Simulations show that with inlet basin set up to imitate laboratory discharge can cause errors during the first phase. Physical processes of discharged water are affected in numerical simulations before water enters the main basin. The velocity profile of buoyant outflow is laterally uniform in case of  $K = 1$  [4, 20]. When  $K > 1$  channel is wide in comparison to the Rossby deformation radius and rotational effects deflect the flow to the right in the channel. This results in a laterally non-uniform

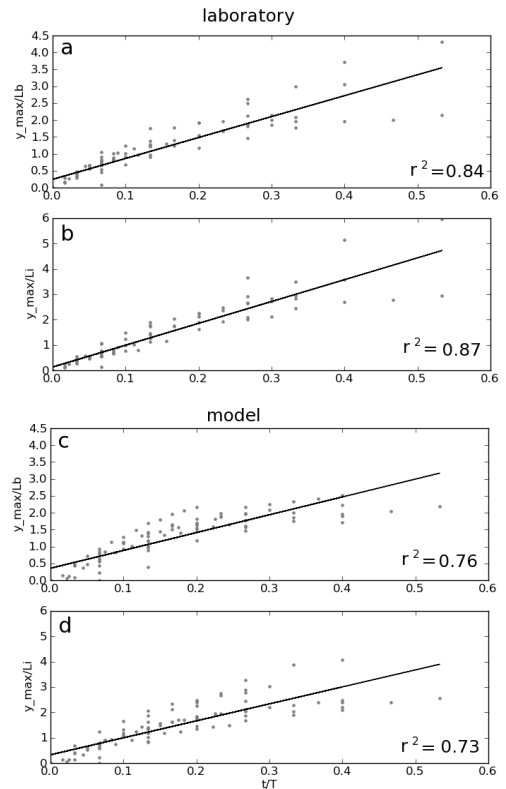


**Fig. 6. Bulge offshore spreading during the first phase (described in text) non-dimensionalized by bulge Rossby radius (a and c) and internal radius (b and d). All numerical and laboratory simulation runs are included. Figure illustrates scattering therefore distinguishing between runs are not important at that point. Solid line is linear regression and R2 coefficient of determination.**

velocity profile with high current speed at the right hand side wall in the channel mouth looking towards the main basin. When  $K < 1/K > 1$  model underestimates/overestimates bulge offshore spreading (Fig. 4 and Table 1). Results agree with Huq 2009 [15] who concluded that with  $K \sim O(1)$  the Rossby deformation radius and channel/estuary width are in balance and flow is not deflected to the right significantly.

Despite the differences arising during the first and the second phase, laboratory and numerical bulge spreading results agree reasonably well. During the second phase spreading is nearly unaffected by Kelvin number. Therefore it is possible to get a good estimate of bulge spreading when using inlet basin but in the case of a narrow or wide estuary modification during the initial phase must be considered.

In laboratory simulations during the first phase, front spreading scales with the internal radius that takes into account inlet geometry (discharge width and depth) and exclude buoyancy forcing (density difference). The shift to scaling with the bulge Rossby radius during the second phase indicates increasing influence by buoyancy forcing and lessening influence by inertial forcing and estuary geometry. The difference between scaling with these two parameters and between the two phases however is so small that it would be arbitrary to draw fundamental conclusions.

The numerical simulation scales better with the bulge Rossby radius in comparison to internal radius during both phases. During the first phase the difference between scalings is negligible. During the second phase scaling with bulge Rossby radius gives much better convergence the with internal radius.

Thus during the first phase the laboratory experiments scale with internal radius while the model scales better with Rossby radius but difference is not significant. We speculate that it is due to using an inlet basin as discussed above. During the second phase both laboratory and numerical simulations scale with bulge Rossby radius.

Most recent studies agree that centrifugal acceleration adds to geostrophic balance in the rotating bulge. Scaling with inertial radius is justified if the bulge is in cylostropic balance. A laboratory study by Horner-Devine 2006 [12] scaled bulge center offshore displacement with inertial radius and total area (effective radius) with the bulge Rossby radius. In present study, scaling is done by considering the bulge offshore front that corresponds to effective radius.

**ACKNOWLEDGMENTS**

This work was funded in part by Estonian Minister for Education and Research.

**BIBLIOGRAPHY**

[1] Avicola G and Huq P (2003) The characteristics of the recirculating bulge region in coastal buoyant outflows Journal of Marine Research, Volume 61, Number 4, 1 July 2003 , pp. 435-463(29)

[2] Chant, R.J., J. Wilkin, W. Zhang, B.-J. Choi, E. Hunter, R. Castelao, S. Glenn, J. Jurisa, O. Schofield, R. Houghton, J. Kohut, T.K. Frazer, and M.A. Moline. 2008. Dispersal of the Hudson River plume in the New York Bight: Synthesis of observational and numerical studies during LaTTE. *Oceanography* 21(4):148–161, <http://dx.doi.org/10.5670/oceanog.2008.11>.

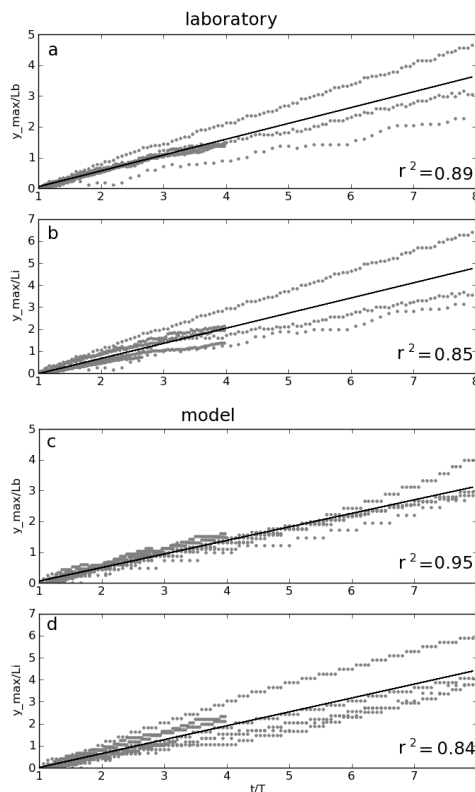


Fig. 7. Same as Fig. 6 but for the second phase.

- [3] Chen SN, Geyer W R, and Hsu TJ (2013). A numerical investigation of the dynamics and structure of hyperpycnal river plumes on sloping continental shelves. *Journal of Geophysical Research: OCEANS*, VOL. 118, 2702–2718, doi:10.1002/jgrc.20209, 2013
- [4] Fong DA (1998). Dynamics of Freshwater Plumes: Observations and Numerical Modeling of the Wind-forced Response and Alongshore Freshwater Transport. Ph.D. thesis, Joint Program in Oceanography, MIT/WHOI.
- [5] Fong DA, Geyer WR (2002). The Alongshore Transport of Freshwater in a Surface-Trapped River Plume. *J. Phys. Oceanog.* 32, 957–972.
- [6] Garvine RW (1995). A dynamical system for classifying buoyant coastal discharges. *Cont. Shelf Res.*, 15(13), 1585–1596.
- [7] Garvine RW (2001). The impact of model configuration in studies of buoyant coastal discharge. *J. of Marine Res.*, 59(2), 193–225.
- [8] Gregorio SO, Haidvogelb DB, Thomasa PJ, Taskinoglu ES, Skeend AJ (2011) Laboratory and numerical simulations of gravity-driven coastal currents: Departures from geostrophic theory. *Dynamics of Atmospheres and Oceans* 52 (2011) 20– 50
- [9] Hetland RD, Signell RP (2005). Modelling coastal current transport in the Gulf of Maine. *Deep-Sea Res. II*, 52, 2430–2449.
- [10] Holford J, Dalziel S. (1996). Measurements of layer depth during baroclinic instability in a two-layer flow. *Applied Scientific Research*, 56(2), 191–207.
- [11] Horner, A.R., D.A. Fong, J.R. Koseff, T. Maxworthy and S.G. Monismith, 2000. The control of coastal current transport. Fifth International Symposium on Stratified Flows, IAHR, 2:865-870, Vancouver, B.C.
- [12] Horner-Devine AR (2006). Velocity, density, and transport measurements in rotating, stratified flows. *Experiments in Fluids* online, pages 1–13, doi:10.1007/s00348--006--0181--2.
- [13] Horner-Devine AR, Fong DA, Monismith SG (2008). Evidence for the inherent unsteadiness of a river plume: Satellite observations of the Niagara River discharge. *Limnol. Oceanogr.*, 53, 2731–2737.
- [14] Horner-Devine, A.R. (2009). The bulge circulation in the Columbia River plume. *Cont. Shelf Res.*, 29, 234–251, doi: 10.1016/j.csr.2007.12.012.
- [15] Huq P (2009) The Role of Kelvin Number on Bulge Formation from Estuarine Buoyant Outflows. *Estuaries and Coasts* (2009) 32:709–719 DOI 10.1007/s12237-009-9162-z
- [16] Kudela RM, Horner-Devine AR, Banas NS, Hickey BM, Peterson T D, Lessard EJ, Frame E, Bruland KW, Lohan M, Jay DA, Peterson J, Peterson B, Kosro M, Palacios S, Dever EP (2001) Multiple trophic levels fueled by recirculation in the Columbia River plume. *Geophys. Res. Lett.*, 37, 7 pg. L18607 doi:10.1029/2010GL044342.
- [17] Narayanan C, Garvine RW (2002) Large scale buoyancy driven circulation on the continental shelf. *Dynamics of Atmospheres and Oceans* 36 (2002) 125–152.
- [18] Nof D, Pichevin T (2001) The ballooning of outflows. *J. of Phys. Oceanogr.*, 31, 3045–3058.
- [19] Shchepetkin AF, McWilliams JC (2005) The regional oceanic modeling system (ROMS): a split-explicit, free-surface, topographically-following-coordinate oceanic model. *Ocean Modelling*, 9, 347—404.
- [20] Rafael V. Schiller \*, Vassiliki H. Kourafalou (2010) Modeling river plume dynamics with the HYbrid Coordinate Ocean Model. *Ocean Modelling* 33. 101–117

- [21] Thomas PJ, Linden PF (2007) Rotating gravity currents: small-scale and large-scale laboratory experiments and a geostrophic model. *J. Fluid Mech.* (2007), vol. 578, pp. 35–65.
- [22] Vlasenko V, Stashchuk N and McEwan R (2013). High-resolution modelling of a large-scale river plume. *Ocean Dynamics* (2013) 63:1307–1320 DOI 10.1007/s10236-013-0653-x
- [23] Yankovsky AE, Chapman DC (1997) A simple theory for the fate of buoyant coastal discharges. *J. of Phys. Oceanogr.*, 27, 1386--1401.
- [24] Yuan Y, Avenier ME, Horner-Devine AR (2011) A two-color optical thickness method for determining layer depth in two interacting buoyant plumes., *Exp. Fluids.*, 50:5, pg. 1235-1245, DOI: 10.1007/s00348-010-0969-y.

## **Publication II**

Soosaar, E., Maljutenko, I., Uiboupin, R., Skudra, M. and Raudsepp, U. (2016). River bulge evolution and dynamics in a non-tidal sea - Daugava River plume in the Gulf of Riga, Baltic Sea. *Ocean Sci.*, 12, 417-432.





# River bulge evolution and dynamics in a non-tidal sea – Daugava River plume in the Gulf of Riga, Baltic Sea

Edith Soosaar, Ilja Maljutenko, Rivo Uiboupin, Maris Skudra, and Urmas Raudsepp

Marine Systems Institute at Tallinn University of Technology, Tallinn, Estonia

Correspondence to: Edith Soosaar (edith.soosaar@msi.ttu.ee)

Received: 1 September 2015 – Published in Ocean Sci. Discuss.: 21 October 2015

Revised: 4 February 2016 – Accepted: 29 February 2016 – Published: 10 March 2016

**Abstract.** Satellite remote sensing imagery and numerical modelling were used for the study of river bulge evolution and dynamics in a non-tidal sea, the Gulf of Riga (GoR) in the Baltic Sea. Total suspended matter (TSM) images showed a clearly formed anti-cyclonically rotating river bulge from Daugava River discharge during the studied low wind period. In about 7–8 days the bulge grew up to 20 km in diameter, before being diluted. A high-resolution (horizontal grid step of 125 m) General Estuarine Transport Model (GETM) was used for detailed description of the development of the river plume in the southern GoR over the period when satellite images were acquired. In the model simulation, the bulge growth rate was estimated as  $r_b \sim t^{0.5 \pm 0.04}$  ( $R^2 = 0.90$ ). Both the model simulation and the satellite images showed that river water was mainly contained in the bulge and there were numerous intrusions at the outer perimeter of the bulge. We performed numerical sensitivity tests with actual bathymetry and measured river runoff without wind forcing (1) having an initial three-dimensional density distribution, and (2) using initially a homogeneous ambient density field. In the first case, the anti-cyclonic bulge did not develop within the course of the model simulation and the coastal current was kept offshore due to ambient density-driven circulation. In the second case, the river plume developed steadily into an anti-cyclonically recirculating bulge, with  $r_b \sim t^{0.28 \pm 0.01}$  ( $R^2 = 0.98$ ), and a coastal current. Additional simulations with constant cross-shore and alongshore winds showed a significant effect of the wind in the evolution of the river bulge, even if the wind speed was moderate ( $3\text{--}4\text{ m s}^{-1}$ ). While previous studies conclude that the mid-field bulge region is governed by a balance between centrifugal, Coriolis and pressure gradient terms, our study showed that geostrophic balance is valid for the entire mid-field of

the bulge, except during the 1–1.5 rotation period at the beginning of the bulge formation. In addition, while there is discharge into the homogenous GoR in the case of a high inflow Rossby number, the river inflow might split into two jets, with strong mixing zone in-between, in the plume near-field region.

## 1 Introduction

River water entering a coastal ocean typically forms a buoyant plume with an expanding anti-cyclonically rotating bulge near the river mouth and a coastal current in the coastally trapped wave direction (Fong and Geyer, 2002). Coastal currents are favoured in the case of low-discharge conditions and downwelling winds, while bulge formation is favoured during high-discharge conditions and upwelling winds (Chant et al., 2008). The anti-cyclonically recirculating bulge is characteristic of the surface advective plume (Yankovsky and Chapman, 1997), being a prominent feature in rotating tank experiments and numerical simulations under ideal conditions (Avicola and Huq, 2003; Horner-Devine et al., 2006; Thomas and Linden, 2007). Approximately 25–70 % of river water is trapped in the bulge (Fong and Geyer, 2002).

Observational studies confirm that the bulge is a naturally occurring phenomenon with many rivers (Chant et al., 2008; Horner-Devine et al., 2008; Horner-Devine, 2009; Valente and da Silva, 2009; Saldías et al., 2012; Hopkins et al., 2013; Mendes et al., 2014; Pan et al., 2014; Fernández-Nóvoa et al., 2015), but an anti-cyclonic rotation inside a bulge is observed seldom (Kudela et al., 2010; Horner-Devine, 2009; Chant et al., 2008). Observations of the evolution of the bulge over a certain time period are almost non-existent, with the ex-

ception of the Niagara River plume (Horner-Devine et al., 2008) and the Tagus estuary plume (Valente and da Silva, 2009). However, both cases are without clear evidence of anti-cyclonic circulation within the bulge.

In natural conditions, the evolution of the bulge is affected by properties of the outflow (Yankovsky and Chapman 1997; Avicola and Huq, 2003), tides (Valente and da Silva, 2009), wind (Dzwonkowski and Yan, 2005; Whitney and Garvine, 2005) and the ambient coastal current (Fong and Geyer, 2002). Thus, the evolution of the structure and circulation inside the bulge is difficult to observe. Exploitation of optical satellite remote sensing has extended the possibilities of monitoring and understanding the river plume dynamics under various hydrological, morphological and hydrodynamical conditions. A number of existing papers provide composite maps where plume location and structure are described in response to prevailing wind conditions. Neither the evolution of the bulge nor the anti-cyclonic circulation within it can be identified from the composite satellite remote sensing images. Although each river plume can be considered as specific, Horner-Devine et al. (2015) have summarized the dynamics of an anti-cyclonically rotating bulge, with special emphasis on the river water volume recirculating within the bulge. In their study, with reference to Nof and Pichevin (2001), they summarize that, with stronger anti-cyclonic circulation within the bulge, more water recirculates in the bulge.

The aim of the present paper is to provide additional evidence of a well-developed anti-cyclonically rotating river bulge, using consecutive optical remote sensing images from a non-tidal sea, and to assess current theoretical understanding of river bulge internal structure and dynamics from the complementary numerical model simulation results. We focus on the evolution of an anti-cyclonically rotating bulge during one life-cycle, i.e. from its formation until its dilution with ambient water. The horizontal expansion of the bulge from remote sensing imagery and the reproduction by numerical simulation are compared with modelled undisturbed bulge development and existing theoretical knowledge. The bulge depth, volume of the river water trapped in the bulge and the movement of the bulge centre are evaluated from model experiments. The validity of gradient wind (or cyclostrophic) balance (see Eq. 2 below) is evaluated for specific time instants in the mid-field region of the plume.

The eastern sub-basin of the Baltic Sea, the Gulf of Riga (GoR), is used as the study area (Fig. 1a). The GoR is almost bowl-shaped, has brackish water and is semi-enclosed (connection to the Baltic Sea through the Irbe Strait, 25 m deep, minimum cross-section area 0.4 km<sup>2</sup> and, through the Virtsu Strait which is 5 m deep, a minimum cross-section area of 0.04 km<sup>2</sup>). The circulation in the GoR is mainly driven by wind forcing and three-dimensional density gradient forcing (Raudsepp et al., 2003; Soosaar et al., 2014b; Lips et al., 2016). The mean circulation in spring consists of two main gyres, with the cyclonic gyre covering the eastern part and

the anti-cyclonic gyre covering the western part of the GoR (Soosaar et al., 2014b; Fig. 2). This two-gyre system may transform into a single anti-cyclonic gyre/cyclonic gyre covering most of the basin area during the warm/cold season (Lips et al., 2016). A small tidal oscillation ( $O[0.01\text{--}0.1\text{ m}]$ ; Keruss and Sennikovs, 1999) allows us to consider it as a non-tidal estuary. The main freshwater source for the GoR is the Daugava River in the south-east, with a high discharge of 2500 m<sup>3</sup> s<sup>-1</sup> in early spring, which decreases to 200 m<sup>3</sup> s<sup>-1</sup> in late summer. The present study concentrates on the period from the last 12 days of March and early April 2007, when there was a high discharge of  $\sim 2500\text{ m}^3\text{ s}^{-1}$  and low wind.

## 2 Materials and methods

### 2.1 Satellite data

ENVISAT/MERIS (Medium Resolution Imaging Spectrometer) data with a 300 m resolution from the Coast Colour database (<http://www.coastcolour.org/data/archive/>) were used for monitoring bulge dynamics and structure. MERIS was designed to monitor coastal waters (Doerffer et al., 1999) and, therefore, it has sufficient spectral resolution in the range of wavelengths above 555 nm for monitoring turbid and optically complex waters like the Baltic Sea (Gitelson et al., 2009). MERIS imagery was preferred to other similar sensors (e.g. MODIS) as (i) MERIS-based water quality retrievals in optically complex Case-2 waters of the Baltic Sea are more accurate due to better performance of the atmospheric correction algorithm (Goyens et al., 2013). In addition, (ii) MERIS has a higher spatial resolution (300 m), which enables us to resolve detailed features of the river bulge. The MERIS images were processed using the Case-2 Regional (C2R) algorithm (Doerffer and Schiller, 2007, 2008) in the BEAM software package (<http://www.brockmann-consult.de/cms/web/beam/>) in order to apply atmospheric correction and to obtain the reflectance values used for TSM (total suspended matter) retrieval. The pixel quality flags/masks provided in the Level 1 Coast Colour product and in the Level 2 C2R product were used to mask the invalid pixels affected by the following phenomena: land, whitecaps, sun glint, cloud, cloud shadow, snow and ice. The C2R algorithm has been validated in various locations in the optically complex waters of the Baltic Sea, and it has proven to be suitable for water quality monitoring (e.g. Sitam et al., 2014; Attila et al., 2013; Vaičīūtė et al., 2012). We used TSM concentrations as a marker to distinguish turbid river water from “clear sea water” as TSM shows a stronger contrast compared to other biological and physical parameters (SST – sea surface temperature – and CHL – chlorophyll). Moreover, a comparative study by Beltrán-Abaunza et al. (2014) showed that TSM concentrations are more accurately retrieved by different standard remote sensing algorithms (including C2R) than other water constituents. A total

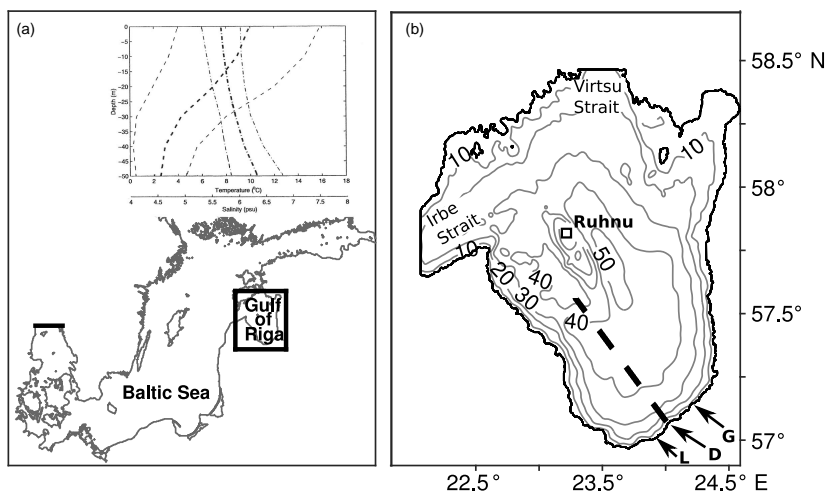


**Figure 1.** Map showing the location of the Gulf of Riga in the Baltic Sea (a). Embedded are mean (bold) temperature (dashed) and salinity (dash dotted) profiles with standard deviations (thin) from the central Gulf of Riga (adopted from Raudsepp, 2001). Topography of the Gulf of Riga (b). Arrows mark river mouth locations for the Daugava (D), Lielupe (L) and Gauja (G) rivers. The square shows the location of the weather station. The bold dashed line shows the transect of ferry-box measurements used for the model validation.

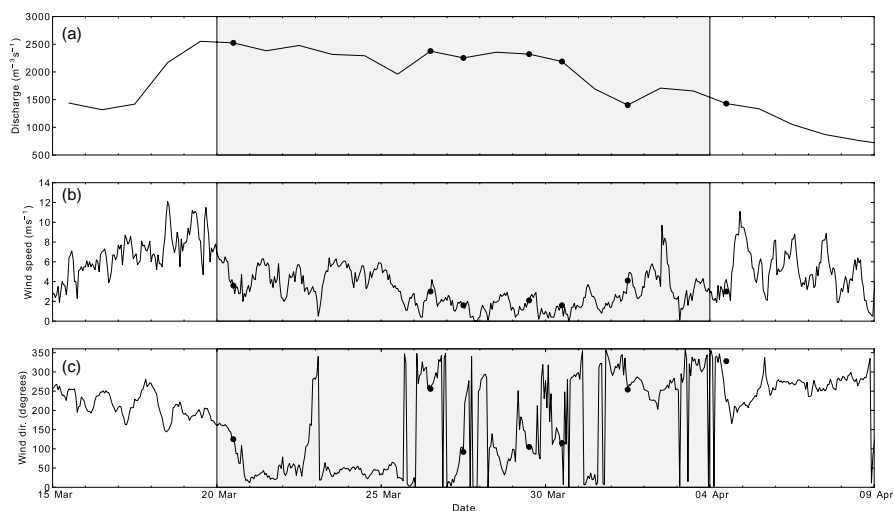


**Figure 2.** Time series of daily mean Daugava River discharge (a), hourly wind speed (b) and wind direction (c) measured at Ruhnu weather station. Black dots show time instants when satellite images were acquired. The grey area marks the period between the first and last available satellite image from the study period (20 March to 4 April).

of seven sufficiently cloud-free images was available from 20, 26, 27, 29, and 30 March and 1 and 4 April. The images were acquired at about 09:00 UTC. The satellite data were interpolated to a regular  $0.3 \text{ km} \times 0.3 \text{ km}$  grid on the UTM-34v projection. Then the TSM concentrations were smoothed using a  $3 \times 3$  point median filter.

## 2.2 River runoff and wind data

Daily volume flux for the Daugava River was measured 35 km upstream from the river mouth (coordinates –  $56.8516^\circ \text{ N}$ ,  $24.2728^\circ \text{ E}$ ). Daily volume flux for the Gauja and Lielupe rivers (see Fig. 1 for locations) was calculated

from measured data. As the locations of measurement stations are 55 and 95 km from the river mouth, the measured data were multiplied by factors 1.05 and 1.87 respectively<sup>1</sup>, in order to obtain river discharge at the river mouth. The coefficients are obtained as a ratio between the whole catchment area of those rivers and the catchment area of those rivers up to the stations where the river flow was measured.

Wind data at 1 h intervals were obtained from Ruhnu weather station, which is located on the island of Ruhnu in the central area of the Gulf of Riga (Figs. 1 and 2).

### 2.3 Numerical model set-up: GETM

For numerical simulation we used the fully baroclinic and hydrostatic ocean GETM model (General Estuarine Transport Model, Burchard and Bolding, 2002) that is coupled to the GOTM (General Ocean Turbulence Model, Umlauf and Burchard, 2005) for vertical turbulence parameterization. The GETM uses a spherical coordinate system in the horizontal plane and a bottom-following vertical coordinate system. Using a mode splitting technique, GETM solves water dynamics on the Arakawa C-grid (Arakawa and Lamb, 1977). The GETM is characterized by advanced numerical techniques of advection schemes and internal pressure discretization schemes that minimize computational errors (Stips et al., 2004; Burchard and Rennau, 2008). In our set-up we used the total variance diminishing (TVD) advection scheme for salinity, temperature and momentum (Pietrzak, 1998) and internal pressure parameterization suggested by Shchepetkin and McWilliams (2003). In our set-up we used the third-order monotone total variance diminishing (TVD) advection scheme with the P2-PDM limiter and a half-step directional split approach for salinity, temperature and momentum (Pietrzak, 1998; Klingbeil, 2014). Temporal discretization was conducted with a coupled explicit mode splitting technique for barotropic and baroclinic modes.

The model domain covered the GoR with closed boundaries at the Irbe Strait and the Virtsu Strait. In the study by Soosaar et al. (2014b), comparison of monthly mean circulations, with the Irbe and Suur straits being either closed or opened, showed only minor differences that occur mostly near the straits. The coefficient of determination between the two cases for April 1998 was  $R^2 = 0.93$ . Our analyses of model simulations concentrate on the south-eastern part of the GoR where the effect of closed straits is expected to be negligible over the simulation time period of 2 weeks. Topography was prepared using the Baltic Sea Bathymetry Database (BSHC, 2013) and interpolated to a 125 m regular grid. Depths at the head of Daugava were adjusted to include the Riga harbour fairway (depth 7 m). The vertical water column was split into 30 density adaptive layers, giving a vertical resolution of under 0.5 m within the stratified bulge area

<sup>1</sup>Methodology worked out and in use for the Gauja and Lielupe rivers in LVGMC – Latvian Environment, Geology and Meteorology Centre Institute. <http://www.meteo.lv/en/>.

(Gräwe et al., 2015). The barotropic time step was 3 s and the baroclinic time step 60 s. Hourly river runoff input from the measurements of three rivers, Daugava, Lielupe and Gauja, was included. Daugava runoff was equally distributed over seven grid cells. The meteorology was adopted from the EM-CWF ERA-Interim data set with a lateral resolution of  $1/4^\circ$  and a temporal resolution of 6 h (Dee et al., 2011).

The model simulation covered the period from 20 March to 5 April 2007. Initial salinity fields were interpolated from the 1 nautical mile simulation for the Baltic Sea (Maljutenko and Raudsepp, 2014). The density only depended on salinity. A 3-day spin-up period with a realistic salinity field and a linear increase in river runoff from zero to the measured river runoff value on 20 March 2007 was used before including wind forcing on 20 March (real simulation). TSM was used as a passive tracer for the detection of river water spreading in the model simulation. The initial TSM concentration was set to zero in the GoR and the TSM concentration in river water was set to a unit value. The passive tracer was released into the GoR only as the Daugava River load of TSM, being proportional to the Daugava River runoff starting from 20 March.

### 2.4 Model validation

In situ measurements suitable for the model validation from the study area during high Daugava River runoff are ferry-box measurements on board the ship travelling between Riga and Stockholm. The available measurements for the estimation of the ability of the model to reproduce Daugava River bulge dynamics cover the period from 20 March to 4 April 2014. This period comprises the increase in the Daugava River runoff from  $600 \text{ m}^3 \text{ s}^{-1}$  to the peak value of  $1100 \text{ m}^3 \text{ s}^{-1}$  and the decrease in the runoff to  $800 \text{ m}^3 \text{ s}^{-1}$  (Fig. 3a). In total, eight transects from the Daugava River mouth to the central GoR with 2-day intervals fall into the period (Fig. 1). The model set-up for the validation run was made similarly to the one described in Sect. 2.3. The daily river runoff input from the measurements of the Daugava River was included. The meteorology was adopted from the HIRLAM-ETA data set, with a lateral resolution of 11 km and a temporal resolution of 3 h (Undén et al., 2002). Initial salinity fields were interpolated from the HIROMB 1 nautical mile simulation for the Baltic Sea on 20 March 2014 (Funkquist and Kleine, 2000). The density only depended on salinity. No spin-up period was included.

The mid-field bulge front can be characterized as the location of a maximum salinity gradient. We calculated the salinity gradient along the ship transect from measurements and model results. The maximum gradient location from in situ measurements stayed mostly at 5 km from the river mouth (Fig. 3c). There are two exceptions, on 29 March and 2 April, when the maximum gradient was located at 10 km (Fig. 3c) following a period of wind to the west (Fig. 3b). In the model simulation, the bulge front increased from 1 km on 21 March

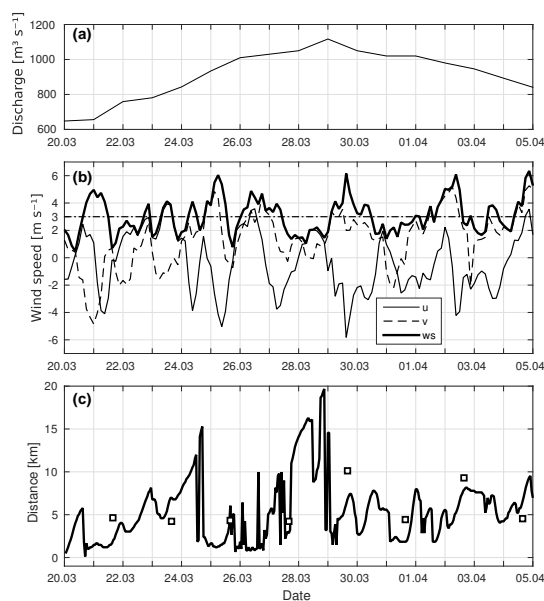


**Figure 3.** Time series of (a) daily mean Daugava River discharge; (b) 3 h wind speed (bold), eastern (solid) and northern (dashed) wind components from the HIRLAM-ETA data set at Ruhnu, and  $3 \text{ m s}^{-1}$  wind speed (dash dotted); (c) offshore location of the maximum salinity gradient from model (solid) and ship measurements (open square) for the period from 20 March to 5 April 2014. Distance is measured along the ship track from the mouth of the Daugava River.

to 15 km on 24 March. That period corresponded to the period of increase in river runoff and low winds (Fig. 3a, b). From the evening of 24 March the wind speed increased and the bulge was destroyed. The front retreated to a position at 1 km from the river mouth. The bulge started to increase on 27 March and reached a maximum extent of 20 km on the night of 28 March. This corresponded to a peak in river runoff and calm winds. During the rest of the simulation period, the bulge front remained between 2 and 10 km. The root mean square deviation between the locations of simulated and observed bulge fronts was 2.4 km.

### 3 Results

#### 3.1 Satellite imagery and model simulation

The first satellite image on 20 March showed the development of three river plumes. The Daugava River plume was far larger (about 8 km in diameter) than the Gauja and Lielupe river plumes (Fig. 4a), which can also be seen in the numerical model (Fig. 4h). The wind conditions favoured the development of river plumes. From 15 to 19 March wind speed in-

creased from  $2$  to  $10 \text{ m s}^{-1}$  (Fig. 2b), which could have generated sufficient mixing to destroy previously formed river plumes as well as prevent the development of a clearly distinguishable river plume. Just prior to the first satellite image, the wind speed dropped from  $11$  to  $2 \text{ m s}^{-1}$ , which may have considerably reduced wind mixing and enabled the free development of river plumes. From 17 to 20 March Daugava River discharge increased from  $1500$  to  $2500 \text{ m}^3 \text{ s}^{-1}$  (Fig. 2a). The discharges of the Lielupe and Gauja rivers were  $230$  and  $180 \text{ m}^3 \text{ s}^{-1}$  respectively. The river plumes were quite distinguishable, as the ambient TSM concentration was  $2 \text{ g m}^{-3}$ , compared to  $20 \text{ g m}^{-3}$  in the bulge centre, in the southern part of the GoR (Fig. 4a). In all three cases, the river water had most likely initially spread offshore, then turned to the right and formed a coastal current. In the bulge, current velocities were up to  $50 \text{ cm s}^{-1}$ , while ambient currents were about  $5 \text{ cm s}^{-1}$  (Fig. 4h). All three plumes consisted of a bulge area and a coastal current (Fig. 4a). The coastal current was detached from the coast, leaving a stripe of lower TSM water near the coast (Fig. 4a, h). The offshore location of the maximum currents parallel to the coast and a counter-current at the coast (Fig. 4h) were remnants of the previous spreading of river water along with wind- and density-driven currents in the GoR.

Checking the sequence of tracer spreading in the numerical model showed that the plume on 26 March was the result of the re-initiation of the river plume on 24 March. The winds of  $6 \text{ m s}^{-1}$  from the northeast had hampered the free development of the river plume by mixing river water and transporting it offshore. The Daugava River bulge had a diameter of  $\sim 16 \text{ km}$  (Fig. 4b). The core of the bulge was almost circular, with many intrusions along the outer rim. In the core of the bulge, freshly discharged water with a high TSM concentration formed a jet with an anti-cyclonic spreading pattern along the left side of the bulge. The existence of a coastal current could not be verified on the satellite image and the bulge manifested itself as more of a separate feature of the plume. The coastal current had formed as a narrow band pressed against the coast in the numerical model (Fig. 4i). As shown in Sect. 3.2, the northeasterly wind may push the bulge offshore and cause several intrusions at the open sea area of the bulge (Fig. 6b). Model simulation showed a strong background anti-cyclonic circulation of about  $20 \text{ cm s}^{-1}$  in the south-eastern GoR (Fig. 4i). The Gauja River plume consisted of a bulge area and a coastal current attached to the coast. The Lielupe River plume was almost undetectable, as the volume discharge had decreased to  $130 \text{ m}^3 \text{ s}^{-1}$ .

During the next 4 days, i.e. until 30 March, the wind speed was very low, between  $0$  and  $3 \text{ m s}^{-1}$ . We may assume that wind-driven currents and mixing were negligible. The Daugava River bulge remained almost circular and further detached from the coast (Fig. 4c–e, i–l). The main feature within the bulge was anti-cyclonically turning river water with a high TSM concentration (Fig. 4c–e) and a well-established anti-cyclonic circulation in the bulge, with a char-

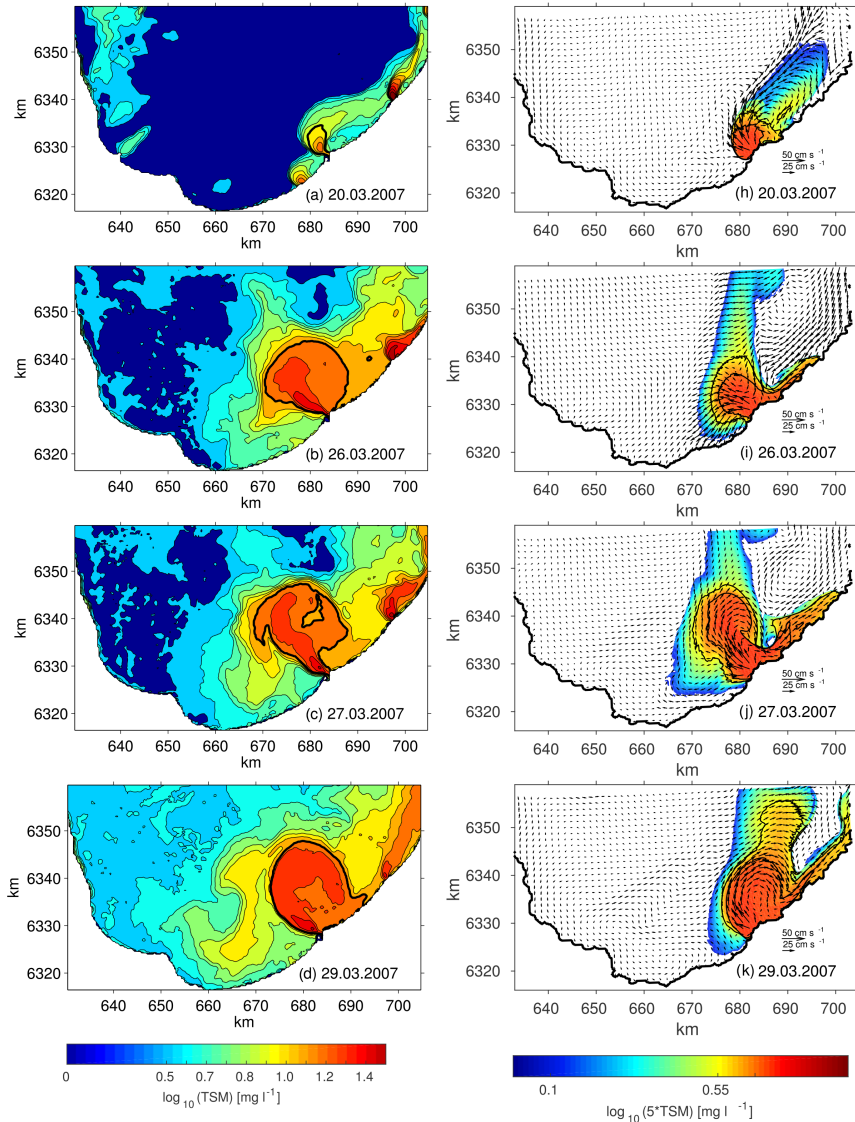


**Figure 4.**

acteristic current speed of  $20 \text{ cm s}^{-1}$  (Fig. 4i–l). This gives direct confirmation that water in natural buoyant bulges circulates anti-cyclonically in the Northern Hemisphere. More water intruded into the southern GoR at the western boundary of the bulge. Even weak onshore wind may cause significant intrusions at the western boundary of the bulge (Fig. 6d). This intrusion spread anti-cyclonically, probably due to ambient circulation, and diluted with surrounding water. No clear coastal currents were visible.

By 1 April, the wind speed had increased to  $4 \text{ m s}^{-1}$  and was blowing from the north. Daugava River discharge had decreased from  $\sim 2000$  to  $\sim 1500 \text{ m}^3 \text{ s}^{-1}$  (Fig. 2). The image from 1 April still showed a circular bulge with a notably smaller TSM concentration than previously (Fig. 4f). The bulge had been transported westward and was nearly detached from the Daugava River outlet. The numerical model captured the tendency of westward transport of the bulge from 30 March to 1 April, but the bulge was more distorted

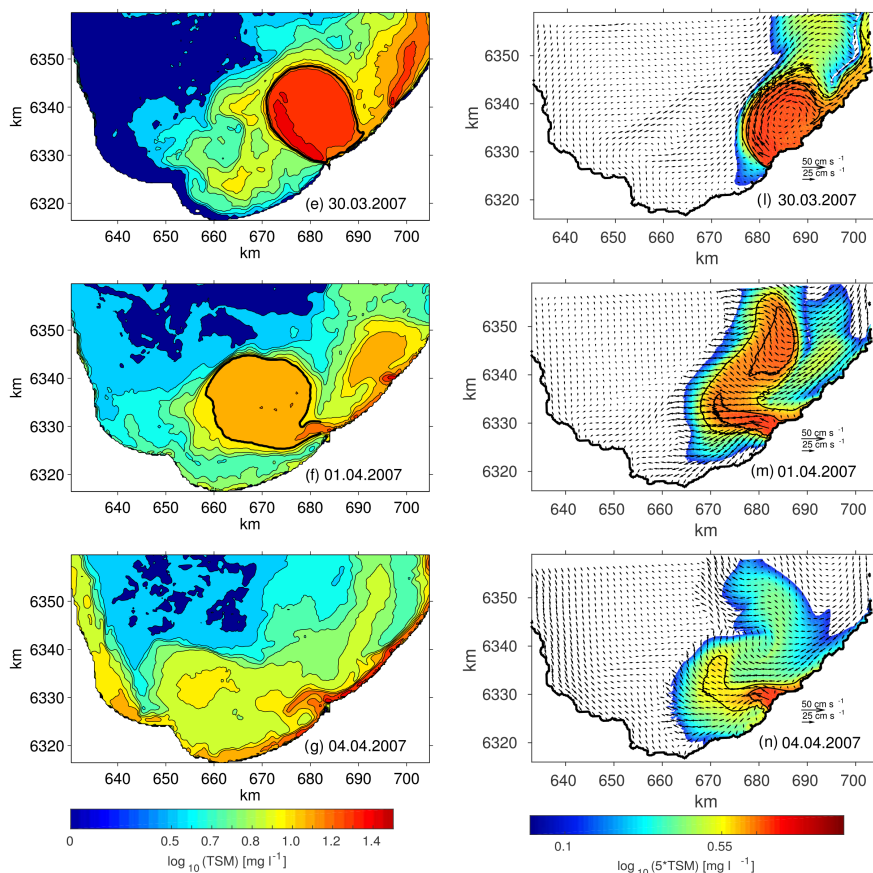


**Figure 4.** TSM concentration maps for the southern part of the Gulf of Riga from satellite images (left column) and TSM concentration and surface velocity maps from the numerical simulation (right column). The bold contours on the satellite images show the indicative edge of the Daugava River bulge. Black contours on the numerical model simulation maps represent TSM concentrations of  $\log_{10}(\text{TSM}) = -0.15$  and  $= -0.05$ . The former is used for the determination of the Daugava River bulge. The coordinate system is on the UTM-34v projection (Cont.).

(Fig. 4m). The strong wind event of  $10 \text{ m s}^{-1}$  on 2 April had destroyed the bulge, and river water with a higher TSM concentration had smeared over the southern GoR by 4 April (Fig. 4g, n).

### 3.2 Idealized simulations

In the realistic model simulation, the Daugava River plume was affected by river discharge, ambient currents and wind-driven currents. We performed numerical sensitivity tests with (1) river discharge into a stratified GoR, while wind forcing was switched off, and (2) river discharge into a homogeneous GoR with an ambient water salinity of  $6 \text{ g kg}^{-1}$ , which is the long-term average value for the salinity in the central GoR (Raudsepp, 2001, Fig. 2b), while wind forcing

was switched off (ideal simulation). In the first case, the anti-cyclonic bulge did not develop within the course of the model simulation and the coastal current was kept offshore due to ambient circulation (Fig. 5a). In the ideal run, river plume developed steadily into an anti-cyclonically recirculating bulge and a coastal current (Fig. 5b). The bulge length (offshore extent) and width (along-shore extent) as well as the width of the coastal current increased steadily in the course of the model simulation.

Additional simulations with cross-shore and alongshore winds were made with wind speeds of 2 and  $4 \text{ m s}^{-1}$ . A wind speed of  $2 \text{ m s}^{-1}$  caused minor, if any, alterations in the case of all wind directions (not shown). A wind speed of  $4 \text{ m s}^{-1}$  altered the bulge in agreement with the classi-

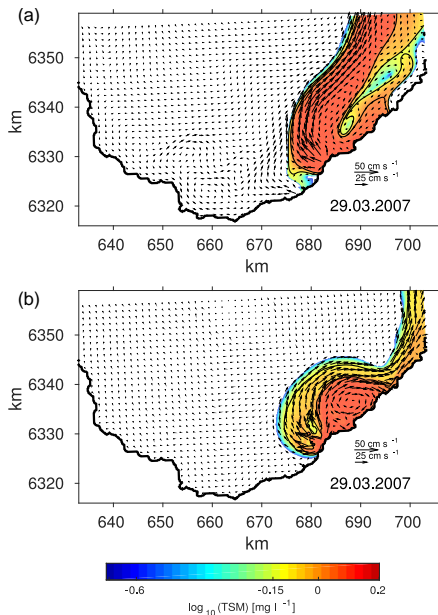


**Figure 5.** Instantaneous surface velocity and TSM concentration maps for simulation with realistic ambient density and no wind forcing (a) and idealized model simulation with uniform ambient density and no wind forcing (b) at noon on 29 March 2007. Solid lines represent TSM concentrations of  $\log_{10}(\text{TSM}) = -0.15$  and  $= -0.05$ . The coordinate system is on the UTM-34v projection.

cal Ekman transport theory. The alongshore downwelling favourable wind pushed the bulge towards the coast and the coastal current was well developed (Fig. 6a). The alongshore upwelling favourable wind pushed the bulge offshore, so that the bulge was detached from the coast and no coastal current developed (Fig. 6b). The bulge had an irregular shape with several intrusions at the open sea area of the bulge. In the case of offshore wind, the bulge mid-field region was less uniform, closer to the coast, and coastal current was enhanced (Fig. 6c). Onshore wind tilted the bulge to the upcoast direction, with significant intrusions at the upcoast rim of the bulge (Fig. 6d). The coastal current was restrained and had an irregular shape. Thus, comparison of the real run with test cases showed a significant effect of wind in the evolution of the river bulge, even if wind speed was moderate (see Fig. 2b).

### 3.3 Temporal evolution of the bulge

The evolution of the river bulge is classically described by the spreading of the offshore front of the bulge and an increase in bulge depth (e.g. Avicola and Huq, 2003; Horner-Devine et al., 2006). There are uncertainties in the determination of the edges of a bulge as well as the volume of a bulge.

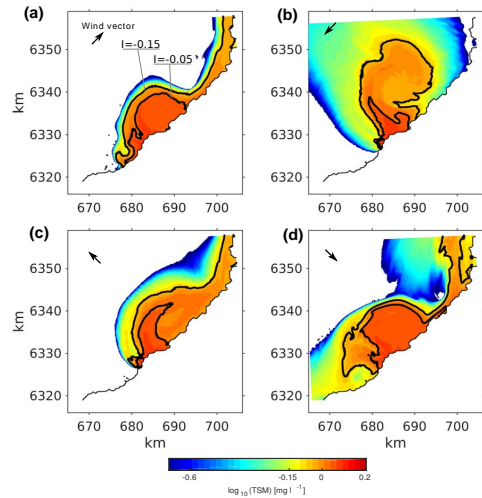


**Figure 6.** Instantaneous surface TSM concentration maps for simulation with uniform ambient density and a constant wind speed of  $4 \text{ m s}^{-1}$  blowing in a downstream (a), upstream (b), offshore (c) and onshore (d) direction at 6T from the start of the simulation. Solid lines represent TSM concentrations of  $\log_{10}(\text{TSM}) = -0.15$  and  $= -0.05$ . The coordinate system is on the UTM-34v projection.

In natural conditions, diffusion and mixing at the edges dilute river water with surrounding water (Horner-Devine et al., 2015). Multiple previous studies defined the bulge edge based on a preselected threshold value. Horner-Devine et al. (2006) chose a constant 20% buoyancy contour as the reference value. Gregorio et al. (2011) used a reference velocity,  $1.7 \text{ cm s}^{-1}$ , to define the coastal current front. Soosaar et al. (2014a) defined the bulge edge as 10% of the discharge depth.

We used TSM concentration to define the bulge boundary. Our main criterion was to capture the circular part of the bulge and neglect coastal current as well as most of the intrusions. In the numerical model, the bulge boundary was defined where  $I = \log_{10}(\text{TSM}) > -0.15$ . Different values of  $I > -0.05, -0.10, -0.20, -0.25$  were also used for the bulge boundary. The bulge radius and mean depth increased with decreasing  $I$  (Fig. 7b for radius; mean depth not shown), but the dynamics of the bulge did not depend on the selected threshold value for the bulge boundary.

We compared the temporal evolution of mean depth, radius and volume of the real and ideal bulge from the numerical model. In order to be consistent with previous river bulge studies (Horner-Devine, 2009; Horner-Devine et al., 2006, 2008), the bulge effective radius,  $r_b$ , was estimated through the area of the bulge,  $A_b$ , assuming a circular shape of the bulge

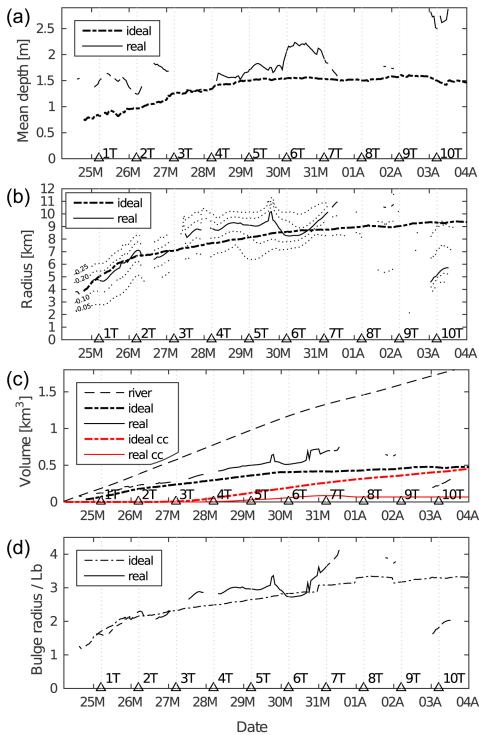


**Figure 7.** Time series of the Daugava River bulge mean depth (a), bulge radius (b), bulge volume (c) and the bulge effective radius scaled with the bulge Rossby radius (d). The solid line represents the real model simulation and the dash-dotted line the idealized model simulation. Time series of the bulge radius where the bulge is defined:  $I = \log_{10}(\text{TSM}) > -0.05; -0.10; -0.20; -0.25$  (dotted) (b). Time series of cumulative river water (dashed), bulge volume (black) and volume of the coastal current (red) in the real model simulation (solid) and ideal model simulation (dash-dotted) (c). Triangles represent the rotation period of the earth starting from 24 March 2007 05:00 GTM.

$$r_b = \left( \frac{A_b}{\pi} \right)^{\frac{1}{2}}. \quad (1)$$

According to the criterion of the bulge definition, the bulge is defined after about  $0.5T$ , where  $T$  is the rotation period of the earth (Fig. 7a, b) and  $T = 0 \equiv 24$  March 2007 05:00. A steady increase of the real bulge took place during seven rotation periods. Both mean depth and radius as well as the volume were larger for the real bulge than for the ideal bulge. We would like to note the pulsation of the real bulge – when bulge diameter increased, bulge mean depth decreased, and vice versa. The decrease in the bulge diameter was faster than the decrease in bulge mean depth during the dissipa-

tion phase, which started from  $7T$ . Occasionally, bulge depth even increased, implying that water in the bulge was mixed deeper during the dissipation phase.

The volume of river water that went into the bulge increased relatively quickly during the first two rotation periods (Fig. 7c). In the real case, almost 60 % of river water was trapped inside the bulge, while in the ideal case the volume reached 45 %. We estimated the volume that was transported away by the coastal current. In order to be consistent with our bulge definition, we calculated water flow at the transect through the model grid cells where  $I > -0.15$ . During  $2T$ , a negligible amount of river water was transported by the coastal current. During  $2T$  the fraction of river water inside the bulge decreased monotonically, while the volume of the coastal current increased (not shown). In the real case, water volume in the bulge increased until the bulge started to dissipate, but steadily retained its 50 % river water content. The fraction of river water started to increase from  $4T$ , but did not exceed 5 % until the end of the simulation. In the case of the real bulge, our estimations showed that about 50 % of river water could be determined as either coastal current or as bulge due to intrusions and mixing at the boundaries of the bulge and the coastal current (see Fig. 4), unless we broaden the definition of the bulge. Still, it is obvious from satellite images and simulation results that a far larger amount of river water stayed within the bulge and was transported offshore by intrusions than the amount that formed a coastal current. In the ideal bulge, the fraction of river water decreased after  $2T$ , while the coastal current increased. During  $11T$ , the fraction of the volume in the bulge and in the coastal current equilibrated. Thus, we may conclude that in the present case of the Daugava River plume, density- and wind-driven currents oppose the development of the coastal current.

The bulge radius was non-dimensionalized with the bulge Rossby radius

$$L_b = \left( \frac{2Qg'}{f^3} \right)^{\frac{1}{4}} \quad (2)$$

where  $Q$  is river runoff. In our case, the bulge Rossby radius varied between 2.7 and 3.1 km in time, according to the actual runoff of the Daugava River. Time series of increase in the non-dimensional bulge radius from numerical simulations are presented in Fig. 7d. We approximated the growth rate of the bulge radius using a power function. In the real case, we excluded the time period when the bulge started to dissipate, i.e. maintaining the values up to  $8T$ . The real and ideal simulations gave  $r_b \sim t^{0.50 \pm 0.04}$  and  $r_b \sim t^{0.28 \pm 0.01}$ , with the coefficients of determination being  $R^2 = 0.90$  and  $R^2 = 0.98$  respectively. Thus, in the real model simulation, the growth of the bulge radius was faster than in the ideal simulation. It can be explained by prevailing upwelling favourable winds (Fig. 2b, c) which even with a speed of  $3\text{--}4 \text{ m s}^{-1}$  restrained the development of a coastal current and retained more water in the bulge (Fig. 6b). Using

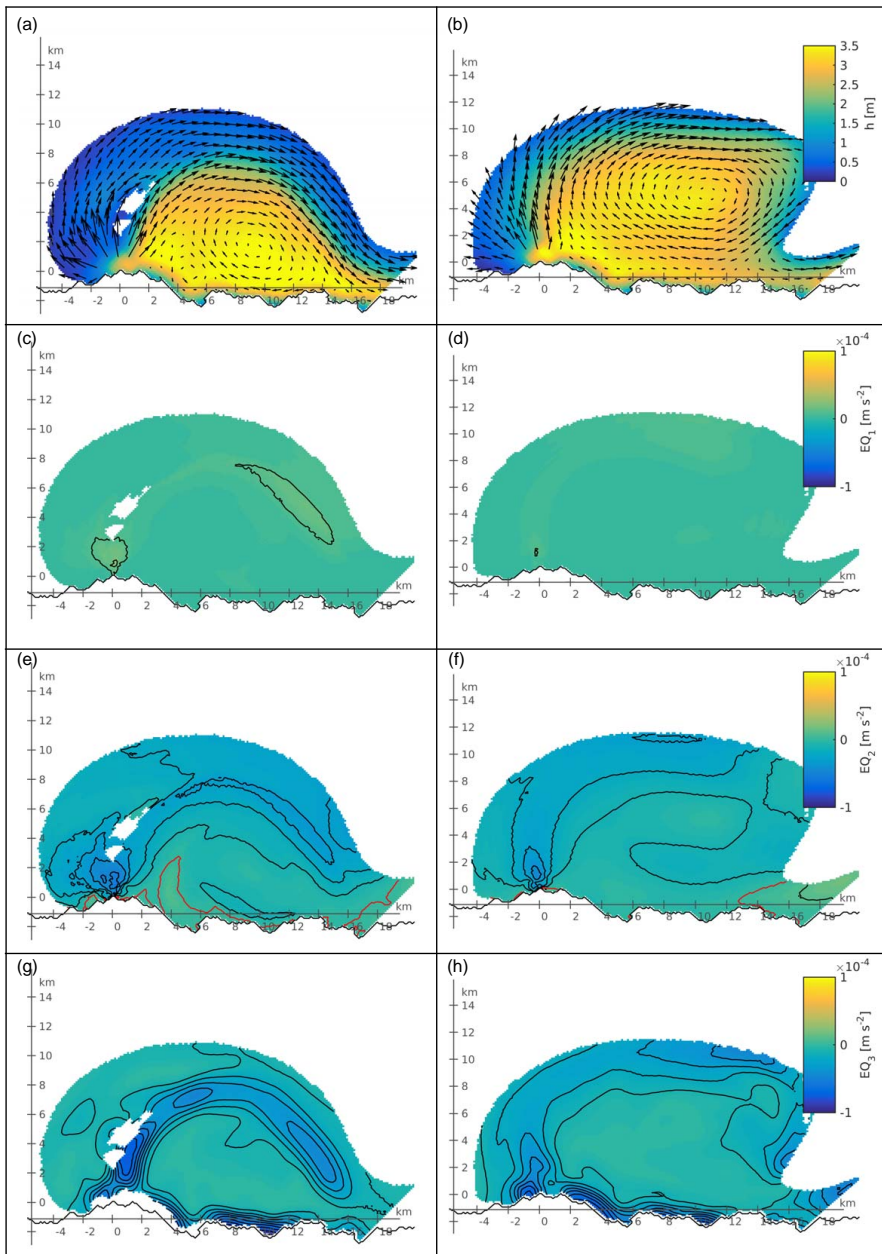


**Figure 8.**

thermal wind balance, Avicola and Huq (2003) estimated the growth rate of the bulge radius  $r_b \sim t^{1/4}$ , although in the laboratory experiments they obtained the growth rate  $r_b \sim t^{2/5}$ . From laboratory experiments, Horner-Devine et al. (2006)

estimated that a buoyant surface advective bulge expands radially as  $\sim t^{1/4}$  during the first five rotation periods, and later as  $\sim t^{2/5}$ . The measurement study for the Niagara River bulge (Horner-Devine et al., 2008) gave  $\sim t^{0.46 \pm 0.29}$ .

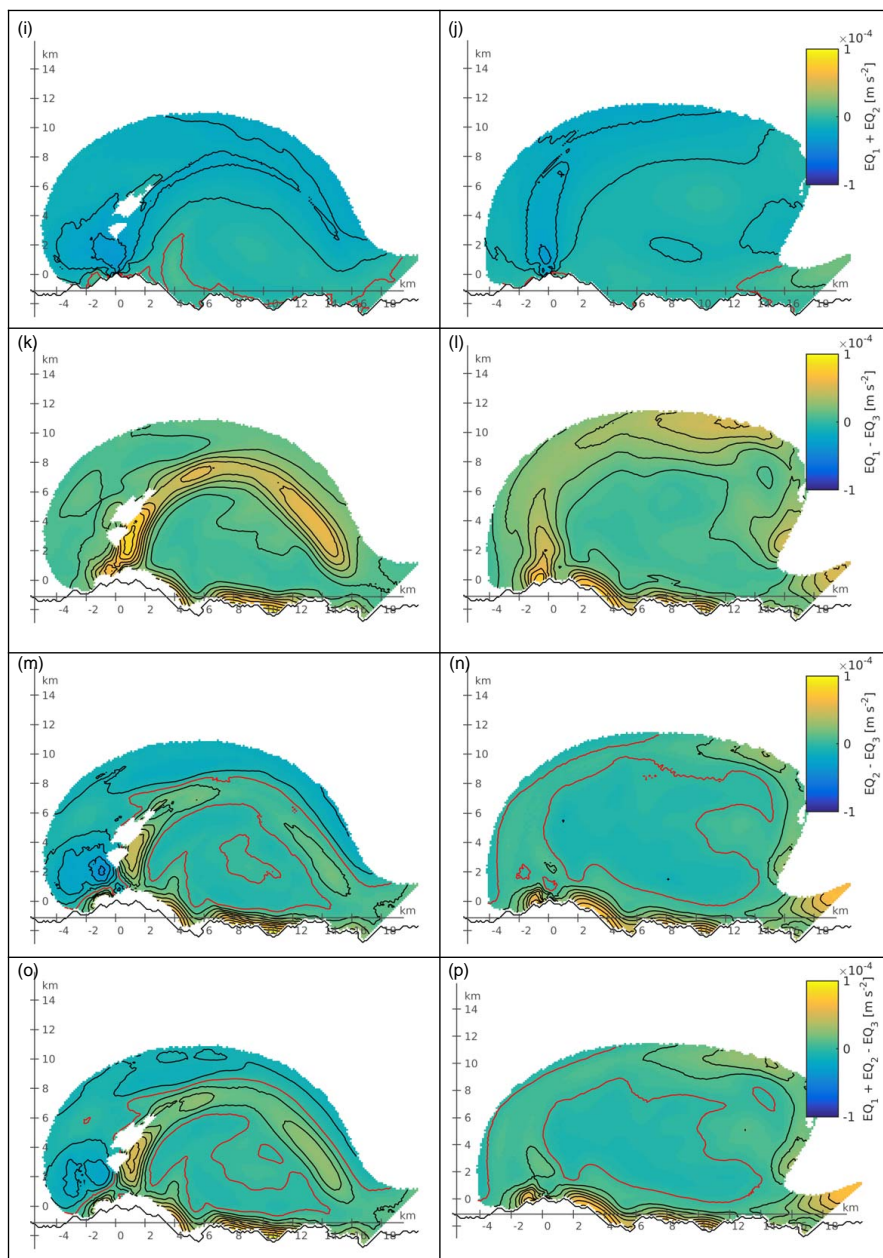


**Figure 8.** Bulge depth and depth averaged velocities, the terms ( $T_1$ ,  $T_2$ ,  $T_3$ ) of the balance (see Eq. 3) and the combinations of the terms for idealized (left column) and realistic (right column) model simulations on 29 March 2007 at 20:00. Bulge depth and depth averaged velocities (**a–b**), centrifugal term ( $T_1$ ) (**c–d**), Coriolis term ( $T_2$ ) (**e–f**), pressure gradient term ( $T_3$ ) (**g–h**),  $T_1 + T_2$  (**i–j**),  $T_1 - T_2$  (**k–l**),  $T_2 - T_3$  (**m–n**) and  $T_1 + T_2 - T_3$  (**o–p**). The contour interval is  $1 \text{ m s}^{-2}$ . The red isoline represents zero. The blank area within the bulge is where the tracer concentrations were below the threshold values of the bulge definition (see text for bulge definition). The origin of the coordinate system is at the mouth of the Daugava River. True north is shown with the arrow (Cont.).

### 3.4 Bulge momentum balance

The dynamics of the river bulge are described as a balance between centrifugal, Coriolis and pressure gradient terms:

$$\frac{v_{\theta}^2}{r} + f v_{\theta} = g' \frac{\partial h}{\partial r}, \quad (3)$$

as hypothesized by Yankovsky and Chapman (1997) and confirmed by Horner-Devine (2009) for the Columbia River plume. In Eq. (3), the  $v_{\theta}$  is depth averaged angular velocity,  $r$  is radial distance from the bulge centre,  $f$  is Coriolis' parameter,  $g'$  is reduced gravity and  $h$  is bulge thickness. The left side of the equations contains the centrifugal ( $T_1$ ) and Coriolis ( $T_2$ ) terms respectively; the right side of the equation is the pressure gradient term ( $T_3$ ). We calculated these terms for the case of the real bulge and the ideal bulge development on 29 March 2007 at 20:00 (Fig. 8). As was the case previously, the bulge was defined where  $I > -0.15$ . The currents were strongest at the steepest slope of the bulge (Fig. 8a, b). Although the ideal and real bulges were similar quantitatively, the bulge centre was much closer to the coast (3 km) for the ideal bulge than for the real bulge (6 km). The outer thin area of the ideal bulge was wider than in the case of the real bulge. All terms in Eq. (3) showed higher absolute values at the steepest slope of the bulge (Fig. 8c–h). With the exception of the near-field region, the centrifugal force was nearly an order of magnitude smaller than the Coriolis' term and the pressure gradient term. Geostrophic balance was valid for the entire mid-field of the bulge (Fig. 8m, n). Taking into account the balance, (Eq. 3), the error even increased slightly (Fig. 8o, p).

We calculated the time series of spatially averaged momentum balance terms, Eq. (3), for the ideal bulge (Fig. 9a) and the real bulge (Fig. 9b). In the case of the ideal bulge, all three terms contributed significantly to the momentum balance during the initial phase of bulge development, i.e. up to  $1T$  (Fig. 9a). Between  $1T$  and  $2T$  the contribution from the centrifugal force decreased, so that this term became nearly an order of magnitude smaller than the Coriolis term and the pressure gradient term. In the case of the real bulge, the centrifugal force also decreased during  $1T$  and  $2T$  (Fig. 9b). However, already at the beginning, the initial value of the centrifugal force was an order of magnitude smaller than the Coriolis and pressure terms. The Coriolis and pressure gradient terms do not have clear increasing or decreasing trends.

## 4 Discussion

A prominent feature in the satellite images and the model simulations was a well-developed anti-cyclonic circulation in the river bulge, which persisted for about 7–8 days. High river discharge and low wind conditions enabled undisturbed development of the bulge. The ideal model simulation showed that the bulge continued to develop steadily for

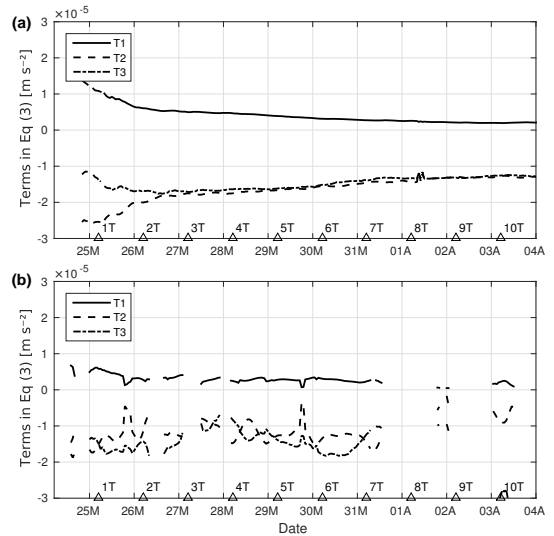


**Figure 9.** Time series of spatially averaged momentum balance terms (see Eq. 3): centrifugal term ( $T_1$ ) (solid), Coriolis term ( $T_2$ ) (dashed), and pressure gradient term ( $T_3$ ) (dash dotted) for ideal (a) and real (b) bulges. Triangles represent the rotation period of the earth starting from 24 March 2007, 05:00.

at least 10 rotation periods. Horner-Devine et al. (2006) argue that in the case of high inflow, i.e. a large Froude number,  $Fr = U(g'H)^{-1/2}$ , where  $U = Q(HW)^{-1}$ ,  $W$  is river width and  $H$  is river depth; the plume becomes unstable after five to six rotation periods. In our case, the Froude number stayed between 0.9 and 1.5 during the whole modelling period ( $W = 700$  m,  $H = 7$  m). The plume was also stable in the numerical experiments of Nof and Pichevin (2001) and Fong and Geyer (2002).

We estimated the movement of the bulge centre in the ideal simulation. The bulge centre moved steadily to the north, completing about 8 km during nine rotation periods (Fig. 10a). As the centre also moved downstream, the actual offshore reach of the centre was 6 km. The radius of the ideal bulge increased from 4 to 9 km from  $0.5T$  to  $10T$ . Thus, by the end of our simulation, the ratio of the bulge centre,  $y_c$ , to the bulge radius was less than 0.7, which according to Horner-Devine et al. (2006) means that the bulge does not separate from the wall and that flow into the coastal current does not decrease. The latter was evident from our numerical simulation with the ideal bulge.

The movement of the real bulge centre was more “chaotic” (Fig. 10b). At each 1 h time step, the bulge centre was defined if the anti-cyclonic circulation with closed streamlines existed (i.e. Fig. 4k). When ambient current overrode bulge circulation, the bulge centre was not defined (i.e. Fig. 4i), although the bulge still existed if we look at the distribution

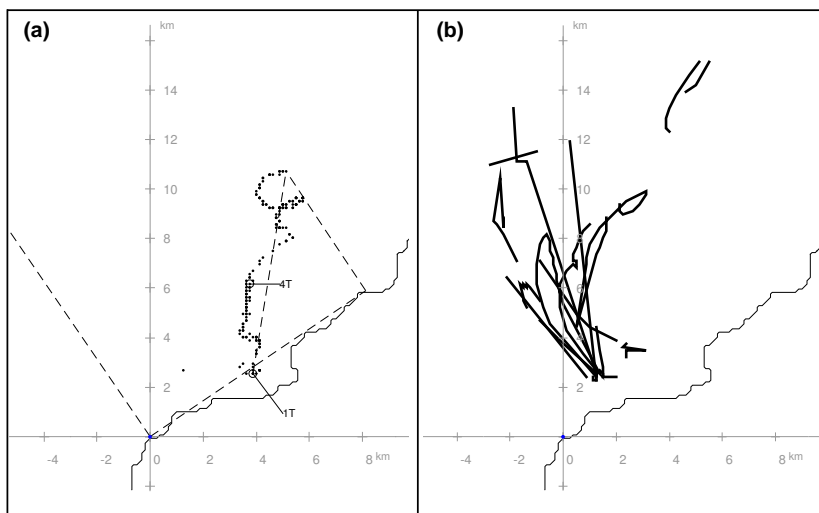


**Figure 10.** The trajectories of the bulge centre for the idealized simulation (a) and the realistic simulation (b) from 24 March 2007 05:00 to 5 April 2007 00:00. Each dot shows the location of the bulge centre at hourly intervals. Dashed lines show the normal and tangent to the coastline, the distance of the bulge centre from the location at 1T up to the end of the simulation, and the distance of the bulge centre at the end of the simulation to the coast in the direction of the normal to the coast. 1T and 4T show the location of the bulge centre after one and four rotation periods of the earth starting from 24 March 2007 05:00 (a). Discontinuities in the bulge trajectories for the realistic model simulation exist because the bulge centre was defined only if anti-cyclonic circulation with closed streamlines was present (b).

of the tracer concentration. Thus, the movement of the bulge centre was not followed continuously. The main feature in the movement of the bulge centre was offshore–onshore oscillations (Fig. 10b). This behaviour is somewhat similar to bulge pinch-off described by Horner-Devine et al. (2006). Horner-Devine et al. (2006) proposed the ratio of internal radius,  $L_i = U/f$ , to the bulge Rossby radius,  $L^* = L_i/L_b$ , to estimate bulge behaviour. In the case of the Daugava discharge, that ratio was between 0.81 and 1.26, which corresponds to situations where the bulge is forced offshore relative to its radius (Horner-Devine et al., 2006, Fig. 17d–g). In the case of a high Froude number and/or low  $g'$  (in our case,  $0.045 \text{ m s}^{-2}$ ), the bulge becomes unstable and the flow to the coastal current is reduced (Horner-Devine et al., 2006). The behaviour of the Daugava River bulge from satellite images and the real numerical model simulation (Fig. 4) showed that river water was mainly contained in the bulge and that there were numerous intrusions at the outer perimeter of the bulge, which is qualitatively similar to the bulge behaviour in the model simulation by Horner-Devine et al. (2006, his Fig. 14).

Horner-Devine et al. (2015) summarize the results of the volume fraction going into a coastal current relative to river discharge, depending on inflow Rossby number. A relatively high Rossby number  $O[1]$  implies that most freshwater stays in the bulge, while a lower Rossby number would imply that there is less water going into the bulge and more into the coastal current. In the Daugava River outflow, the inflow

Rossby number varied between 3.4 and 5.7, which suggests that almost all of the river water should have been trapped in the bulge. Our estimates from the numerical model calculation showed that the fraction of river water that formed a coastal current was up to 10 times smaller than the amount of river water that remained in the bulge. In the ideal case, considerable volume went into the coastal current, although  $Q$ ,  $Fr$ ,  $Ro$  and  $g'$  were the same for ideal and real model simulations.

The explanation for the discrepancy between the ideal bulge and laboratory experiments could be the different behaviour of the plume in a near-field region. In a near-field region, river flow has a lift-off point in the location where river water detaches from the bottom and the upper layer Froude number is equal to one (Horner-Devine et al., 2015). At the lift-off point, vertical velocities cause shoaling of the plume interface and acceleration of the upper layer flow in a more seaward region. This, in turn, increases the Froude number, resulting in intense vertical mixing. In our idealized numerical simulation, the lift-off occurred at about 0.5 km from the river mouth (Fig. 8a). The most intensive mixing started at 1 km from the coast where tracer concentrations were below the limit of the bulge definition (white area in Fig. 8a and low tracer concentration in Fig. 5a). The intensive mixing suppressed horizontal flow and the current velocities were low right behind the intense mixing zone, while the current velocities were higher at the left and right sides of the mixing

zone (Fig. 8a). Thus, the intensive mixing zone created a barrier for the river water flow and split it into two jets. The jet on the right formed a rotating bulge. As the barrier altered the flow direction, the flow angle was notably smaller than  $90^\circ$ , resulting in a bulge centre located closer to the coast (Avicola and Huq, 2003). The jet on the left remained on the outer edge of the bulge. Such a barrier region is not observed in laboratory simulations. Natural buoyant river plumes have a small vertical to horizontal aspect ratio,  $O(10^{-3})$ , where vertical turbulent flux of density is considered to be dominant over horizontal turbulent fluxes (Horner-Devine et al., 2015). For laboratory simulations, the aspect ratio is at least an order of magnitude smaller. Horizontal turbulence flux would be comparable in magnitude to vertical mixing, and a sharply separated region of intense mixing is far less likely to form. In addition, in our numerical simulations, the Daugava River runoff was smeared over five horizontal grid points right at the coast, which enables a better resolution of the river plume in the near field than, for instance, that achieved by Hetland and Signell (2005).

In the case of the realistic model simulation, wind mixing overpowered the local mixing, thereby avoiding the creation of the barrier region. The density-driven and wind-forced background currents restricted the development of a plume coastal current and pushed the river bulge offshore. As a result, the bulge centre was further away from the coast (see Fig. 10b).

## 5 Conclusions

Satellite TSM images showed a clearly formed river bulge from the Daugava River discharge during the studied low wind period. Satellite images also confirmed anti-cyclonic rotation inside the bulge. The bulge grew up to 20 km in diameter before being diluted. A high-resolution numerical model simulation repeated the plume behaviour satisfactorily and enabled a detailed study of the bulge dynamics. While previous studies conclude that balance in Eq. (3) is valid for the bulge, our study showed that geostrophic balance is valid for the entire mid-field of the bulge except during 1–1.5*T* at the beginning of the bulge formation. Comparison of realistic and idealized model simulations showed a significant effect of wind-driven and density-driven circulation in the evolution of the river bulge, even if the wind speed was moderate.

The bulge radius was non-dimensionalized with the bulge Rossby radius. The real model simulation (measured wind and realistic ambient density) and the ideal simulation with no wind and uniform ambient density gave  $r_b \sim t^{0.50 \pm 0.04}$  and  $r_b \sim t^{0.28 \pm 0.01}$ , with the coefficients of determination being  $R^2 = 0.90$  and  $R^2 = 0.98$  respectively. The bulge spreading rates agree well with laboratory experiments ( $\sim t^{1/4}$  by Horner-Devine et al., 2006) and fit in the margin of the Niagara River bulge study ( $\sim t^{0.46 \pm 0.29}$  by Horner-Devine et al., 2008).

Mean depth and radius as well as the volume were larger for the realistic model bulge than for the idealized bulge. River bulge behaviour from satellite images and the real numerical model simulation showed that river water is mainly contained in the bulge and there were numerous intrusions at the outer perimeter of the bulge caused by prevailing upwelling favourable and onshore winds. The fraction of river water that formed a coastal current was up to 10 times smaller than the amount of river water that remained in the bulge.

In the ideal simulation, considerable volume went into the coastal current, although  $Q$ ,  $Fr$ ,  $Ro$  and  $g'$  were the same for ideal and real model simulations. The ideal numerical model simulation showed that in the case of a high inflow Rossby number, the river inflow might split into two jets in the plume near-field region, with a strong mixing zone in-between. Although the ideal and real bulges were similar, the splitting of the outflow into two jets caused the bulge centre to be closer to the coast in the case of the ideal bulge than in the case of the real bulge.

*Acknowledgements.* Volume flux data for the Gauja and Lielupe rivers were provided by state limited liability company Latvian Environment, Geology and Meteorology Centre in Riga, Latvia. Volume flux data for the Daugava River were provided by Latvengero AS (a state joint stock company that provides electricity for the country's citizens). The work was financially supported by institutional research funding IUT (19-6) of the Estonian Ministry of Education and Research.

Edited by: J. M. Huthnance

## References

- Arakawa, A. and Lamb, V. R.: Computational design of the basic dynamical processes of the UCLA General Circulation Model, *Meth. Comput. Phys.*, 17, 173–263, 1977.
- Attila, J., Koponen, S., Kallio, K., Lindfors, A., Kaitala, S., and Ylöstalo, P.: MERIS Case II water processor comparison on coastal sites of the northern Baltic Sea, *Remote Sens. Environ.*, 128, 138–149, 2013.
- Avicola, G. and Huq, P.: The characteristics of the recirculating bulge region in coastal buoyant outflows, *J. Mar. Res.*, 61, 435–463, 2003.
- BSHC (Baltic Sea Hydrographic Commission): Baltic Sea Bathymetry Database version 0.9.3., available at: <http://data.bshc.pro/> (last access: 8 March 2016), 2013.
- Beltrán-Abaunza, J. M., Kratzer, S., and Brockmann, C.: Evaluation of MERIS products from Baltic Sea coastal waters rich in CDOM, *Ocean Sci.*, 10, 377–396, doi:10.5194/os-10-377-2014, 2014.
- Burchard, H. and Bolding, K.: GETM – a general estuarine transport model, Scientific documentation, Technical Report EUR 20253 EN, European Commission, 2002.
- Burchard, H. and Rennau, H.: Comparative quantification of physically and numerically induced mixing in ocean models, *Ocean Modelling*, 20, 293–311, 2008.

- Chant, R. J., Wilkin, J., Zhang, W., Choi, B.-J., Hunter, E., Castelao, R., Glenn, S., Jurisa, J., Schofield, O., Houghton, R., Kohut, J., Frazer, T. K., and Moline, M. A.: Dispersal of the Hudson River plume in the New York Bight: Synthesis of observational and numerical studies during LaTTE, *Oceanography*, 21, 148–161, 2008.
- Dee, D. P., Uppala, S. M., Simmons, A. J., Berrisford, P., Poli, P., Kobayashi, S., Andrae, U., Balmaseda, M. A., Balsamo, G., Bauer, P., Bechtold, P., Beljaars, A. C. M., van de Berg, L., Bidlot, J., Bormann, N., Delsol, C., Dragani, R., Fuentes, M., Geer, A. J., Haimberger, L., Healy, S. B., Hersbach, H., Holm, E. V., Isaksen, I., Kallberg, P., Köhler, M., Matricardi, M., McNally, A. P., Monge-Sanz, B. M., Morcrette, J.-J., Park, B.-K., Peubey, C., de Rosnay, P., Tavolato, C., Thepaut, J.-N., and Vitart, F.: The ERA-Interim reanalysis: configuration and performance of the data assimilation system, *Q. J. Roy. Meteor. Soc.*, 137, 553–597, 2011.
- Doerffer, R. and Schiller, H.: The MERIS case 2 water algorithm. *Int. J. Remote Sens.*, 28, 517–535, 2007.
- Doerffer, R. and Schiller, H.: MERIS Regional Coastal and Lake Case 2 Water Project atmospheric correction ATBD (Algorithm Theoretical Basis Document), 1.0, 41 pp., 2008.
- Doerffer, R., Sorensen K., and Aiken, J.: MERIS potential for coastal zone applications, *Int. J. Remote Sens.*, 20, 1809–1818, 1999.
- Dzwonkowski, B. and Yan, X.: Tracking of a Chesapeake Bay estuarine outflow plume with satellite-based ocean color data, *Cont. Shelf Res.*, 25, 1942–1958, 2005.
- Fernández-Nóvoa, D., Mendes, R., Decastro, M., Dias, J., Sánchez-Arcilla, A., and Gómez-Gesteira, M.: Analysis of the influence of river discharge and wind on the Ebro turbid plume using MODIS-Aqua and MODIS-Terra data, *J. Marine Syst.*, 142, 40–46, 2015.
- Fong, D. A. and Geyer, W. R.: The Alongshore Transport of Freshwater in a Surface-Trapped River Plume, *J. Phys. Oceanogr.*, 32, 957–972, 2002.
- Funkquist, L. and Kleiene, E.: An introduction to HIROMB, an operational baroclinic model for the Baltic Sea, Tech. Rep. SMHI, Norrköping, 2000.
- Gitelson, A. A., Gurlin, D., Moses, W. J., and Barrow, T.: A bio-optical algorithm for the remote estimation of the chlorophyll-a concentration in case 2 waters, *Environ. Res. Lett.*, 4, 045003 doi:10.1088/1748-9326/4/4/045003, 2009.
- Goyens, C., Jamet, C., and Schroeder, T.: Evaluation of four atmospheric correction algorithms for MODIS-Aqua images over contrasted coastal waters, *Remote Sens. Environ.*, 131, 63–75, 2013.
- Gräwe, U., Holtermann, P., Klingbeil, K., and Burchard, H.: Advantages of vertically adaptive coordinates in numerical models of stratified shelf seas, *Ocean Model.*, 92, 56–68, 2015.
- Gregorio, S. O., Haidvogel, D. B., Thomasa, P. J., Taskinoglu, E. S., and Skeend, A. J.: Laboratory and numerical simulations of gravity-driven coastal currents: Departures from geostrophic theory, *Dynam. Atmos. Oceans*, 52, 20–50, 2011.
- Hetland, R. D. and Signell, R. P.: Modelling coastal current transport in the Gulf of Maine, *Deep-Sea Res. II*, 52, 2430–2449, 2005.
- Hopkins, J., Lucas, M., Dufau, C., Sutton, M., Stum, J., Lauret, O., and Channelliere, C.: Detection and variability of the Congo River plume from satellite derived sea surface temperature, salinity, ocean colour and sea level, *Remote Sens. Environ.*, 139, 365–385, 2013.
- Horner-Devine, A. R.: The bulge circulation in the Columbia River plume, *Cont. Shelf Res.*, 29, 234–251, 2009.
- Horner-Devine, A. R., Fong, D. A., Monismith, S. G., and Maxworthy, T.: Laboratory experiments simulating a coastal river inflow, *J. Fluid Mech.*, 555, 203–232, 2006.
- Horner-Devine, A. R., Fong, D. A., and Monismith, S. G.: Evidence for the inherent unsteadiness of a river plume: Satellite observations of the Niagara River discharge, *Limnol. Oceanogr.*, 53, 2731–2737, 2008.
- Horner-Devine, A. R., Hetland, R., and Macdonald, D.: Mixing and Transport in Coastal River Plumes, *Annu. Rev. Fluid Mech.*, 47, 569–594, 2015.
- Keruss, M. and Sennikovs, J.: Determination of tides in Gulf of Riga and Baltic Sea. Proc. International Scientific Colloquium “Modelling of Material Processing”, Riga, 28–29 May 1999.
- Klingbeil, K., Mohammadi-Aragh, M., Gräwe, U., and Burchard, H.: Quantification of spurious dissipation and mixing discrete variance decay in a finite-volume frame-work, *Ocean Model.*, 81, 49–64, 2014.
- Kudela, R. M., Horner-Devine, A. R., Banas, N. S., Hickey, B. M., Peterson, T. D., Lessard, E. J., Frame, E., Bruland, K. W., Lohan, M., Jay, D. A., Peterson, J., Peterson, B., Kosro, M., Palacios, S., and Dever, E. P.: Multiple trophic levels fueled by recirculation in the Columbia River plume, *Geophys. Res. Lett.*, 37, L18607, doi:10.1029/2010GL044342, 2010.
- Lips, U., Zhurbas, V., Skudra, M., and Väli, G.: A numerical study of circulation in the Gulf of Riga, Baltic Sea. Part I: Whole-basin gyres and mean currents, *Cont. Shelf Res.*, 112, 1–13, 2016.
- Maljutenko, I. and Raudsepp, U.: Validation of GETM model simulated long-term salinity fields in the pathway of saltwater transport in response to the Major Baltic Inflows in the Baltic Sea, in: *IEEE Xplore: Baltic International Symposium (BALTIC)*, 2014 IEEE/OES, 27–29 May 2014, Tallinn Estonia, IEEE, 23–31, 2014.
- Mendes, R., Vaz, N., Fernández-Nóvoa, D., Silva, J., Decastro, M., Gómez-Gesteira, M., and Dias, J.: Observation of a turbid plume using MODIS imagery: The case of Douro estuary (Portugal), *Remote Sens. Environ.*, 154, 127–138, 2014.
- Nof, D. and Pichevin, T.: The Ballooning of Outflows, *J. Phys. Oceanogr.*, 31, 3045–3058, 2001.
- Pan, J., Gu, Y., and Wang, D.: Observations and numerical modeling of the Pearl River plume in summer season, *J. Geophys. Res.-Oceans*, 119, 2480–2500, 2014.
- Pietrzak, J.: The use of TVD limiters for forward-in-time upstream-biased advection schemes in ocean modeling, *Mon. Weather Rev.*, 126, 812–830, 1998.
- Raudsepp, U.: Interannual and seasonal temperature and salinity variations in the Gulf of Riga and corresponding saline water inflow from the Baltic Proper, *Nordic Hydrology*, 32, 135–160, 2001.
- Raudsepp, U., Beletsky, D., and Schwab, D. J.: Basin-scale topographic waves in the Gulf of Riga, *J. Phys. Oceanogr.*, 33, 1129–1140, 2003.
- Saldías, G., Sobarzo, M., Largier, J., Moffat, C., and Letelier, R.: Seasonal variability of turbid river plumes off central Chile based

- on high-resolution MODIS imagery, *Remote Sens. Environ.*, 123, 220–233, 2012.
- Shchepetkin, A. F. and McWilliams, J. C.: A method for computing horizontal pressuregradient force in an oceanic model with a nonaligned vertical coordinate, *J. Geophys. Res.*, 108, 3090, doi:10.1029/2001JC001047, 2003.
- Siitam, L., Sipelgas, L., and Uiboupin, R.: Analysis of natural background and dredging-induced changes in TSM concentration from MERIS images near commercial harbours in the Estonian coastal sea, *Int. J. Remote Sens.*, 35, 6764–6780, 2014.
- Stips, A., Bolding, K., Pohlmann, T., and Burchard, H.: Simulating the temporal and spatial dynamics of the North Sea using the new model GETM (general estuarine transport model, *Ocean Dyn.*, 54, 266–283, 2004.
- Soosaar, E., Hetland, R. D., Horner-Devine, A., Avenier, M. E., and Raudsepp, U.: Offshore spreading of buoyant bulge from numerical simulations and laboratory experiments. In: *IEEE Xplore: Baltic International Symposium (BALTIC), 2014 IEEE/OES, 27–29 May 2014, Tallinn Estonia, IEEE, 2014a.*
- Soosaar, E., Maljutenko, I., Raudsepp, U., and Elken, J.: An investigation of anticyclonic circulation in the southern Gulf of Riga during the spring period, *Cont. Shelf Res.*, 78, 75–84, 2014b.
- Thomas, P. J. and Linden, P. F.: Rotating gravity currents: small-scale and large-scale laboratory experiments and a geostrophic model, *J. Fluid Mech.*, 578, 35–65, 2007.
- Umlauf, L. and Burchard, H.: Second-order turbulence closure models for geophysical boundary layers. A review of recent work, *Cont. Shelf Res.*, 2, 795–827, 2005.
- Undén, P., Rontu, L., Jörvinen, H., Lynch, P., Calvo, J., Cats, G., Cuxart, J., Eerola, K., Fortelius, C., Garcia-Moya, J. A., Jones, C., Lenderink, G., McDonald, A., McGrath, R., Navascues, B., Nielsen, N. W., Ødegaard, V., Rodrigues, E., Rummukainen, M., Rööm, R., Sattler, K., Sass, B. H., Savijörvi, H., Schreur, B. W., and Sigg, R., The, H., and Tijm, A.: HIRLAM-5 scientific documentation, available at: <http://www.hirlam.org/> (last access: 8 March 2016), 2002.
- Vaičiūtė, D., Bresciani, M., and Bučas, M.: Validation of MERIS Bio-Optical Products with In Situ Data in the Turbid Lithuanian Baltic Sea Coastal Waters, *J. Appl. Remote Sens.*, 6, 063568-1–063568-20, doi:10.1117/1.JRS.6.063568, 2012.
- Valente, A. and Silva, J.: On the observability of the fortnightly cycle of the Tagus estuary turbid plume using MODIS ocean colour images, *J. Marine Syst.*, 75, 131–137, 2009.
- Whitney, M. and Garvine, R.: Wind influence on a coastal buoyant outflow, *J. Geophys. Res.*, 110, C03014, doi:10.1029/2003JC002261, 2005.
- Yankovsky, A. E. and Chapman, D. C.: A simple theory for the fate of buoyant coastal discharges, *J. Phys. Oceanogr.*, 27, 1386–1401, 1997.

### **Publication III**

Soosaar, E., Maljutenko, I., Raudsepp, U. and Elken, J. (2014). An investigation of anticyclonic circulation in the southern Gulf of Riga during the spring period. *Continental Shelf Research*, 78, 75 - 84.





Contents lists available at ScienceDirect

## Continental Shelf Research

journal homepage: [www.elsevier.com/locate/csr](http://www.elsevier.com/locate/csr)

## Research papers

## An investigation of anticyclonic circulation in the southern Gulf of Riga during the spring period



Edith Soosaar\*, Ilja Maljutenko, Urmas Raudsepp, Jüri Elken

Marine Systems Institute at Tallinn University of Technology, Akadeemia 15a, 12618 Tallinn, Estonia

## ARTICLE INFO

## Article history:

Received 20 December 2012

Received in revised form

29 October 2013

Accepted 8 February 2014

Available online 22 February 2014

## Keywords:

Anticyclonic circulation

ROFI

Vorticity

River discharge

Numerical modeling

Gulf of Riga

## ABSTRACT

Previous studies of the gulf-type Region of Freshwater Influence (ROFI) have shown that circulation near the area of freshwater inflow sometimes becomes anticyclonic. Such a circulation is different from basic coastal ocean buoyancy-driven circulation where an anticyclonic bulge develops near the source and a coastal current is established along the right hand coast (in the northern hemisphere), resulting in the general cyclonic circulation. The spring (from March to June) circulation and spreading of river discharge water in the southern Gulf of Riga (GoR) in the Baltic Sea was analyzed based on the results of a 10-year simulation (1997–2006) using the General Estuarine Transport Model (GETM). Monthly mean currents in the upper layer of the GoR revealed a double gyre structure dominated either by an anticyclonic or cyclonic gyre in the near-head southeastern part and corresponding cyclonic/anticyclonic gyre in the near-mouth northwestern part of the gulf. Time series analysis of PCA and vorticity, calculated from velocity data and model sensitivity tests, showed that in spring the anticyclonic circulation in the upper layer of the southern GoR is driven primarily by the estuarine type density field. This anticyclonic circulation is enhanced by easterly winds but blocked or even reversed by westerly winds. The estuarine type density field is maintained by salt flux in the northwestern connection to the Baltic Proper and river discharge in the southern GoR.

© 2014 Published by Elsevier Ltd.

## 1. Introduction

Fresh water from rivers contributes significant amounts of buoyancy to large areas of the coastal sea. The region where buoyancy input by rivers is comparable to or exceeds the seasonal input of buoyancy as heat is called ROFI (Region Of Freshwater Influence; a term adapted by Simpson (1997)). Buoyancy input results in a circulation pattern where lower density water from river output forms a circulating bulge near the source and a coastal current along the right hand coast (in the northern hemisphere) (Yankovsky and Chapman, 1997). Such a circulation pattern is believed to be the result of the combined effect of the inertial and Coriolis forces and is confirmed by multiple in situ measurements and laboratory and numerical simulations (Horner-Devine et al., 2006; Yankovsky and Chapman, 1997).

Local winds, tides and ambient currents modify the spreading of buoyant plume (see Osadchiev and Zavialov, 2013 and reference therein). Regarding local effects, winds that favor downwelling

(towards the buoyant coastal current) compress the plume to the coast (Whitney and Garvine, 2006) and enhance the coastal current (Jurisa and Chant, 2012). Winds that favor upwelling (opposite to the buoyant coastal current) spread buoyant water offshore and can reverse the coastal current (Whitney and Garvine, 2006), so that new discharged water is transported leftwards from the source (Choi and Wilkin, 2007). On the basin scale of large lakes and enclosed seas, spatially uniform wind drives barotropic circulation with downwind currents at the coast and return flow in the center of the basin (Bennett, 1974).

A study by Fujiwara et al. (1997) shows theoretically that when an estuary is wider than the internal Rossby deformation radius, the combination of classical longitudinal estuarine circulation and the Earth's rotation may cause the surface circulation to become anticyclonic at the estuary head. In the northern hemisphere, this circulation will eventually transport fresh water from the river along the left hand coast. Anticyclonic residual circulation has been observed at the estuary head in Ise Bay, Osaka Bay and Tokyo Bay (Fujiwara et al., 1997). The presence of an anticyclonic circulation in the ROFIs is also confirmed by an observational study in the Kattegat-Skagerrak region, which is a transition area between the brackish Baltic Sea and the saline North Sea (Nielsen, 2005).

\* Correspondence to: Marine System Institute at Tallinn University of Technology, Akadeemia tee 15a-321, Tallinn, Estonia.

E-mail address: [edith.soosaar@msi.ttu.ee](mailto:edith.soosaar@msi.ttu.ee) (E. Soosaar).

Measurements in the Kara Sea show the presence of an anticyclonic circulation in the Ob River discharge region in the late summer period (McClimans et al., 2000). The process was reproduced by numerical simulations (Panteleev et al., 2007). In the Gulf of Trieste, in the northern Adriatic, an anticyclonic gyre covers the surface layer during the stratified season (Malačič and Petelin, 2009). In all of these cases, the salinity distribution consists of vertical stratification, i.e. a brackish upper layer and a more saline lower layer, and a horizontal salinity gradient in the surface layer.

The morphological characteristics and hydrographic conditions in the Gulf of Riga (GoR) in the eastern Baltic Sea are well suited for the emergence of an anticyclonic circulation in the GoR head. The GoR is an almost bowl-shaped brackish-water semi-enclosed estuarine sub-basin (Fig. 1a). The area of the GoR is about  $18,000 \text{ km}^2$  (140 km in length and 110 km in width), with a maximum depth of 56 m and mean depth of 22 m. The Daugava River located in the south-eastern part of the GoR is the main fresh water source. The river discharge ranges from  $200 \text{ m}^3 \text{ s}^{-1}$  in late summer to  $2500 \text{ m}^3 \text{ s}^{-1}$  in spring. The GoR has two openings connecting it to the Baltic Sea: the Irbe Strait (with a sill depth of 25 m and a minimum cross-section area of  $0.4 \text{ km}^2$ ) in the west and the Virtsu Strait (with a sill depth of 5 m and a minimum cross-section area of  $0.04 \text{ km}^2$ ) in the north (Fig. 1b).

As the GoR is shallow, water is usually well mixed throughout the period from December to March (Raudsepp, 2001). Ice is formed in the GoR every winter. The annual ice extent as well as duration of ice season has a wide range of variation determined by the severity of the winter (Soosaar et al., 2010). During severe winters ice starts to form in December and may last until the end of April. Increased freshwater discharge from the melting of snow and ice in early spring (March–April) stabilizes the surface layer and contributes to the seasonal stratification, resulting in a more or less two-layered salinity structure (Stipa et al., 1999). In summer and autumn the stratification is mostly maintained by temperature fluxes from the atmosphere. The tides are negligible in the GoR, which simplifies the problem by eliminating one cause of mixing.

Thus, the aim of our study is to investigate the springtime water circulation in the southern GoR, which is well preconditioned for the formation of anticyclonic circulation and is characterized by high river discharge. The input of freshwater

buoyancy exceeds the input of buoyancy as heat, which is in accordance with the formal definition of ROFI by Simpson (1997). As there are no extensive field measurements of currents and salinity distribution available, we mainly rely on the results of numerical model simulations. Sparse in situ measurement data that are used in this study are available for May 1994 and 2006.

## 2. Materials and methods

### 2.1. Numerical model

In this study we use the fully baroclinic and hydrostatic ocean model GETM (General Estuarine Transport Model (Burchard and Bolding, 2002)) that is coupled with the GOTM (General Ocean Turbulence Model (Umlauf and Burchard, 2005)) which is used for vertical turbulence parameterization. The GETM uses a spherical coordinate system in the horizontal plane and a bottom-following vertical coordinate system. Using the mode splitting technique, GETM solves water dynamics on the Arakawa C grid (Arakawa and Lamb, 1977). The GETM is characterized by the advanced numerical techniques of advection schemes and internal pressure discretization schemes that minimize computational errors (Stips et al., 2004; Burchard and Rennau, 2008). Here we used the total variance diminishing (TVD) advection scheme for salinity, temperature and momentum (Pietrzak, 1998) and internal pressure parameterization suggested by Shchepetkin and McWilliams (2003).

For the current model simulations, the model domain covers the whole Baltic Sea (Fig. 1a). The bathymetry has been interpolated to the 2 nautical mile grid from the digital topography by Seifert et al. (2001). Depths have been adjusted so that the maximum depth is 260 m in the deepest areas of the Baltic Sea. The vertical water column is split into 25 sigma layers, where  $z_k$  is the layer depth and  $D$  is the depth of the water column.

The model simulation covers the period from 1 January 1997 to 31 December 2006. Initial salinity and temperature fields were interpolated from the climatic mean field constructed using the Data Assimilation System coupled with the Baltic Environmental Database at Stockholm University (<http://nest.su.se/das>). Initial sea surface elevation was set to zero. Atmospheric forcing was

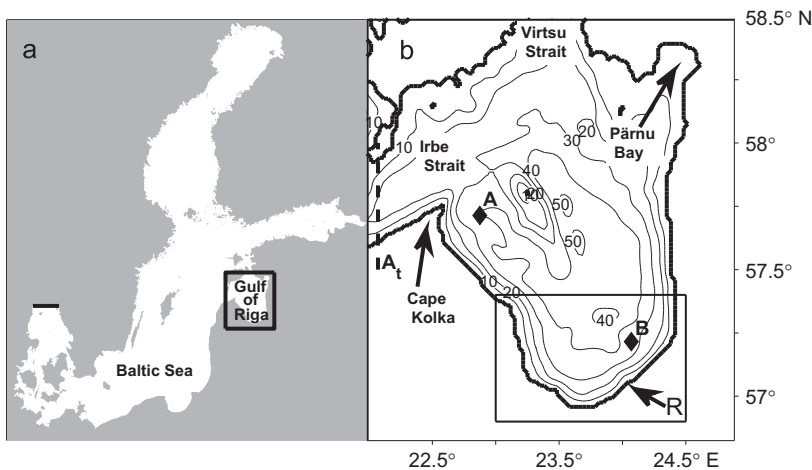


**Fig. 1.** Map showing the location of the Gulf of Riga (a) and its topography (b). R and arrow mark the location of the Daugava River outflow, At is the location of the north–south transect for the calculation of salt flux, A and B are sites where density is calculated (a depth of 30 m for A and 5 m for B). The box shows the area over which spatially averaged relative vorticity is calculated.

adopted from the ERA40 re-analysis data which had been dynamically down-scaled with the Rossby Centre Atmosphere Ocean (RCOA) model (Döscher et al., 2002, 2010). Wind gustiness had been added to wind fields, according to Höglund et al. (2009). For open boundary sea level elevations, data from measurements in Smögen (Sweden) was used. Salinity and temperature at the open boundary was adopted from Janssen et al. (1999) climatological mean fields. River runoff was obtained from the hydrological model HYPE (Lindström et al., 2010). Validation of the model in terms of temperature and salinity has been presented by Passenko et al. (2010). The root mean square error (RMSE) for sea surface temperature at three stations in the Gulf of Finland varied between 0.3 and 0.4, and the RMSE for surface salinity was between 0.7 and 0.9. The corresponding values for bottom temperature and salinity were 0.5–0.9 and 0.9–1.1, respectively.

## 2.2. PCA

To assess the circulation patterns in the southern GoR over a longer time period, the principal component analysis (PCA) of monthly mean horizontal velocity vectors from March to June in 1997–2006 was performed. The velocity vectors were extracted at a depth of 5 m. At first, a time-averaged velocity field was subtracted from the original data, before applying the PCA (Fig. 2). In general, the mean current velocities were low. The strongest current ( $0.03 \text{ m s}^{-1}$ ) was obtained at the river mouth. The velocities of the coastal current along the eastern coast of the gulf and over the interior of the gulf did not exceed  $0.02 \text{ m s}^{-1}$  and  $0.015 \text{ m s}^{-1}$ , respectively. The data was analyzed in the S-mode of the PCA where eigenvectors,  $E_k(\vec{x})$ , represent different modes of the velocity vector field and principal amplitudes (PA),  $A_k(t_n)$ , display temporal variations of the corresponding mode (Preisendorfer and Mobley, 1988), where  $k$  refers to mode number,  $t_n$  is time in months and  $\vec{x}$  is location in the horizontal plane. The horizontal velocity vectors can be reproduced from the orthogonal modes as

$$\vec{U}(t_n, \vec{x}) = (u, v)(t_n, \vec{x}) = \sum_{k=1}^K A_k(t_n) E_k(\vec{x}), \quad (1)$$

where  $(u, v)$  are current velocity components in  $x$  and  $y$  directions, respectively, and  $K$  is the total number of orthogonal modes. The corresponding PA shows how dominant this mode is for a particular month. Positive amplitude values show circulation in the same

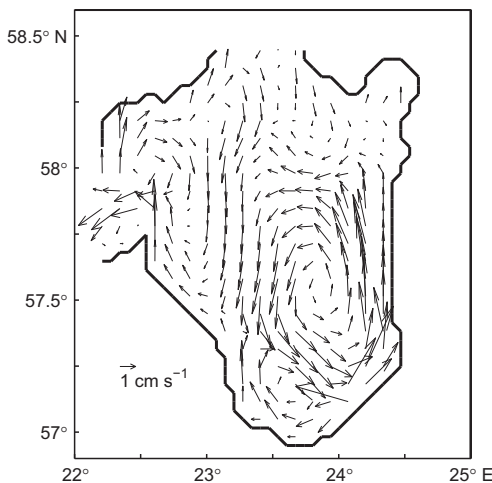


Fig. 2. Mean velocity at a depth of 5 m calculated over the four spring months (March–June) and covering a simulation period of ten years (1997–2006).

direction as shown by the mode. When amplitude values are negative, corresponding circulation is opposite in direction.

The coefficient of determination,  $r^2$ , shows how well a particular mode explains the corresponding monthly mean circulation and is defined as

$$r_k^2(t_n) = 1 - \frac{\sum_{i,j} \{ [u_{ij}^m(t_n) - A_k(t_n)u_{ij}^k(t_n)]^2 + [v_{ij}^m(t_n) - A_k(t_n)v_{ij}^k(t_n)]^2 \}}{\sum_{i,j} [u_{ij}^{m^2}(t_n) + v_{ij}^{m^2}(t_n)]}, \quad (2)$$

where superscript  $m$  refers to the model and  $k$  to the principal component. The subscripts  $i$  and  $j$  refer to the location in the model grid in  $x$  and  $y$  directions.

## 3. Results

The model data for the GoR was extracted from the model simulation for the whole Baltic Sea for the period 1997–2006. We use monthly mean velocity and salinity data for the four months of March, April, May and June during each model year. These months comprise the period of the melting of ice in the GoR and high river runoff (Soosaar et al., 2010), which cause stratification of the water column due to salinity (Raudsepp, 2001; Stipa et al., 1999) and represent the gulf-type ROFI according to the definition by Simpson (1997).

### 3.1. The cases of anticyclonic and river plume circulations

From the whole model data set, we present horizontal salinity and velocity distribution at a depth of 5 m together with salinity and the cross-section velocity component along the transect in the southern part of the GoR for April 1998 and 2006 (Figs. 3 and 4). We analyzed monthly mean salinity profiles from the southern GoR and a 5-m depth was chosen because this depth represents the upper layer in the two layer approximation of the water column stratification during all the months considered, and is within the river plume thickness. April 1998 (Fig. 3) represents a combination of wind induced double gyre circulation that can be driven by persistent winds from the east (monthly mean wind speed was  $3.2 \text{ m s}^{-1}$ ) and anticyclonic circulation as described by Fujiwara et al. (1997). April 2006 (Fig. 4) represents river plume circulation (Yankovsky and Chapman, 1997) that is supported by weak wind from the south (monthly mean wind speed was  $1.6 \text{ m s}^{-1}$ ). In April 1998 low saline water has spread anticyclonically from the mouth of the Daugava River (Fig. 3a). There is a notable southeast-northwest salinity gradient along the line from Daugava River mouth to Cape Kolka ( $0.7 \times 10^{-4} \text{ g kg}^{-1} \text{ m}^{-1}$  as the mean value within the river plume up to 11 km from the coast, and  $0.09 \times 10^{-4} \text{ g kg}^{-1} \text{ m}^{-1}$  over the rest of the line), which is typical for an estuarine type gulf with its main freshwater sources in the gulf head and an open connection to the sea. A well-established anticyclonic gyre covers the southern part of the GoR (Fig. 3b). The currents are strongest ( $0.07 \text{ m s}^{-1}$ ) on the southwestern side of the gyre and drop to a negligible value on the northeastern side. A stagnation point can be identified at the eastern coast of the GoR ( $57.98^\circ \text{N}$ ,  $24.34^\circ \text{E}$ ) where the flow reaching the coast splits into northward and southward currents. A prominent cyclonic gyre resides in the northwestern part of the GoR (Fig. 3b).

Salinity and cross-section velocity distribution on the east-west transect across the anticyclonic gyre show that the gyre extends down to a depth of 20–25 m and is confined by a halocline below (Fig. 3c and d). Below the halocline, the cross-section velocity is directed to the south over the entire transect. Within the gyre, the vertical salinity distribution is nearly homogeneous (maximum potential energy anomaly (PEA) of  $1.83 \text{ J m}^{-3}$  between



a depth of 0–20 m and longitude of 23.3–23.94°E). PEA,  $\varphi$ , is defined as the integral of the product of the buoyancy force and distance from the reference level

$$\varphi = \frac{1}{H} \int_{-H}^0 g(\bar{\rho} - \rho)z dz \quad (3)$$

where  $g$  is gravity constant,  $H$  is water depth,  $z$  is the layer depth and  $\bar{\rho}$  is average density of the water column

$$\bar{\rho} = \frac{1}{H} \int_{-H}^0 \rho(z) dz. \quad (4)$$

The northward currents are strongest at the surface ( $0.06 \text{ m s}^{-1}$ ) and decrease with depth. The southward currents on the eastern side of the gyre do not exceed  $0.02 \text{ m s}^{-1}$  at the surface due to the merging of the gyre with the northward flowing river water in the upper 8-m thick layer at the eastern coast. The return flow is established below the river water with a maximum southward velocity of  $0.04 \text{ m s}^{-1}$  at a depth of 19 m.

In April 2006, low saline water from the Daugava River has spread along the right hand coast from the river mouth and extends almost to Pärnu Bay (Fig. 4a). There is a strong coastal current of up to  $0.08 \text{ m s}^{-1}$  over the same area (Fig. 4b). The mean salinity gradient along the line between Daugava River mouth and Cape Kolka is  $1.3 \times 10^{-4} \text{ g kg}^{-1} \text{ m}^{-1}$  within the river plume (up to 11 km offshore) and  $0.06 \times 10^{-4} \text{ g kg}^{-1} \text{ m}^{-1}$  along the rest of the line. The circulation pattern consists of 2 cyclonic and 2 anticyclonic circulation cells (Fig. 4b). Except for the river water belt, the water column is well mixed down to a depth of 30 m, the maximum PEA is  $3 \text{ J m}^{-3}$  between a depth of 0–30 m and a longitude of 23.3–23.94°E. The cross-section flow to the south is slow ( $\leq 0.01 \text{ m s}^{-1}$ ) and vertically uniform, except on the water surface. A considerable surface layer current with a northward direction is present in the frontal zone of the river water. This flow is strongest at the surface ( $0.08 \text{ m s}^{-1}$ ) and extends to a depth of 10 m while decreasing in speed. Below, a southward countercurrent exists with a maximum flow of  $0.05 \text{ m s}^{-1}$  on the bottom slope.

Two snapshots of the measured salinity distribution in the surface layer are available for the southern GoR in May 1994 and 2006 (Fig. 5). The salinity distribution in May 1994 shows that fresh water from the river has spread offshore and a bulge-like structure has formed close to the river mouth. The salinity gradient over the gulf is mainly south-north directed. This salinity distribution indicates the presence of anti-cyclonic circulation near the river mouth. Monthly mean wind of  $2.3 \text{ m s}^{-1}$  was from the south in May 1994. In May 2006 there is a strong east–west salinity gradient at the eastern coast of the GoR and a much

more homogeneous salinity distribution in the offshore area. The salinity distribution corresponds to the circulation scheme of a buoyancy-driven coastal current. Monthly mean wind of  $0.8 \text{ m s}^{-1}$  was from the southwest in May 2006.

### 3.2. Circulation patterns in the upper layer

The first three modes from the PCA analysis of the period from March to June in 1997–2006 explain 43%, 14% and 10% of the total variability in the model, respectively. These modes with corresponding time series of the principal amplitudes are presented in Fig. 6. The first mode (Fig. 6a) shows a double gyre circulation pattern where the anticyclonic circulation is located in the south-eastern and cyclonic gyre in the northwestern part of the GoR. This pattern matches the circulation pattern in April 1998 (Fig. 3b) with  $r^2=0.87$ . The circulation pattern of the second mode (Fig. 6b) shows general cyclonic circulation in the whole GoR. There is a strong along-coast current at the eastern coast of the GoR, extending from the mouth of the Daugava River to the Virtsu Strait, and decreasing anticyclonic shear offshore. The coefficient of determination between simulated mean circulation in April 2006 (Fig. 4b) and that explained by the second mode is  $r^2=0.53$ . In the case of the third mode, a large anticyclonic/cyclonic gyre covers most of the GoR area extending to 58°N (Fig. 6c).

In addition to the principal amplitude (PA), we calculated the coefficient of determination according to (2) for each month (Fig. 7). As there is no exact linear relationship between PA and  $r^2$ , we use the threshold value  $r^2 \geq 0.5$  to define whether monthly mean circulation is dominated by a particular mode or not. The threshold value was selected after visual inspection of all monthly mean circulation patterns. According to this criterion, the anticyclonic circulation explained by the first mode in the southern GoR is dominant in April 1998 ( $r^2=0.87$ ), March and April 2001 ( $r^2=0.63$  and  $0.63$ ), May 2002 ( $r^2=0.83$ ), April 2003 ( $r^2=0.51$ ) and April 2005 ( $r^2=0.65$ ), i.e. in six cases. A similar flow structure, but with opposite direction of current vectors, i.e. cyclonic circulation in the southern GoR (negative PA) prevails in March and April 1997 ( $r^2=0.51$  and  $0.70$ ), March, May and June 2000 ( $r^2=0.76$ ,  $0.61$  and  $0.79$ ), June 2003 ( $r^2=0.61$ ) and June 2004 ( $r^2=0.66$ ), i.e. in seven cases. The circulation pattern explained by the second mode with a positive PA prevails in March 1999 ( $r^2=0.66$ ), April 2000 ( $r^2=0.64$ ) and April 2006 ( $r^2=0.53$ ). The second mode with a negative PA explains the flow pattern in May 1999 ( $r^2=0.63$ ), only. There is only one occasion

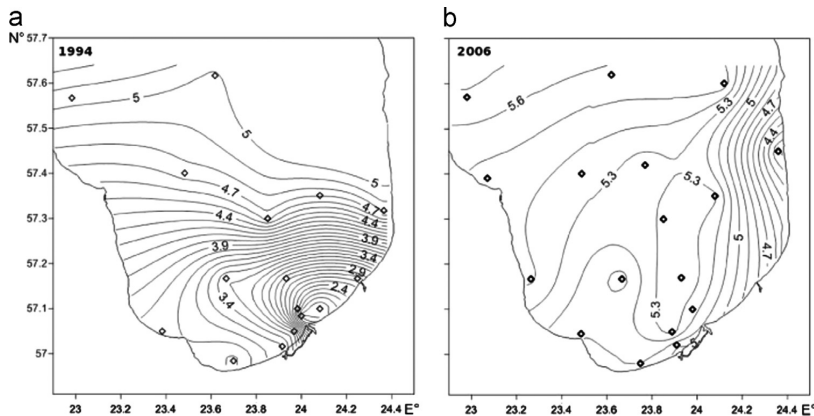
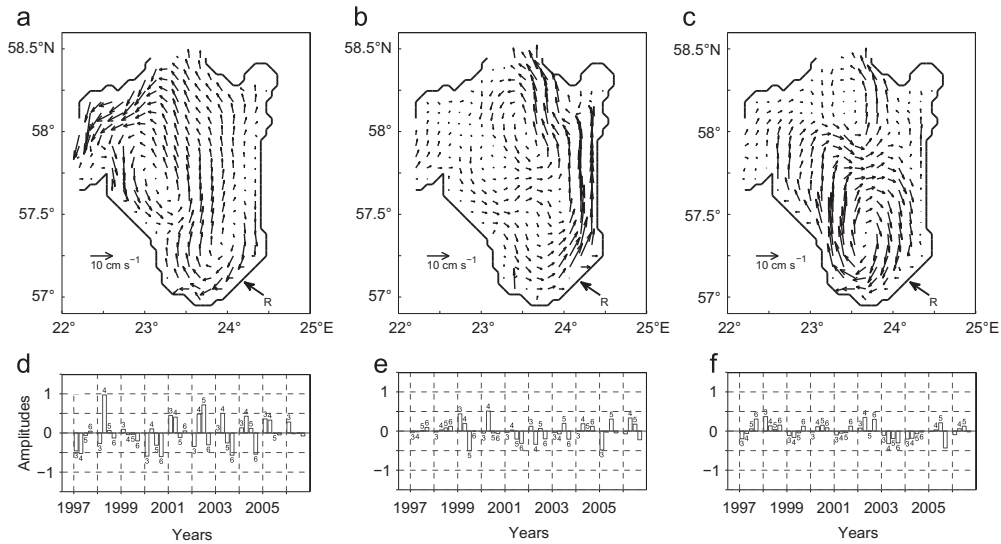
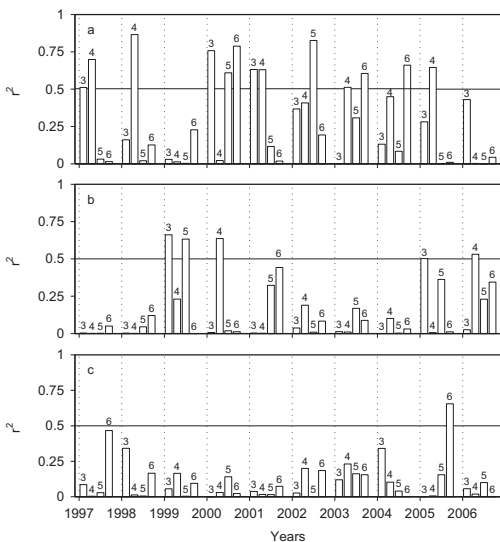


Fig. 5. Measured salinity distribution at a depth of 1 m in the southern GoR in May 1994 (left) and in May 2006 (right). The rhombuses mark locations of stations.



**Fig. 6.** The first (a), second (b) and third (c) circulation modes at a depth of 5 m for March, April, May and June in 1997–2006 and the amplitudes for the corresponding modes (d), (e) and (f), respectively.



**Fig. 7.** Coefficients of determination,  $R^2$ , for the first (a), second (b) and third principal components compared to corresponding monthly mean water circulation at a depth of 5 m.  $R^2$  is calculated according to Eq. (2).

when the third mode exceeds the threshold value, i.e. in June 2005 ( $r^2=0.66$ ) with  $PA < 0$ .

### 3.3. Model sensitivity tests

To analyze the factors that may cause anticyclonic circulation we focus on April 1998 when anticyclonic gyre is strongly present in the southern GoR. Water exchange through the Irbe Strait and Suur Strait, the effect of river discharge, wind forcing and

density-driven circulation were considered. All simulation runs were made over a period of two months (March and April), but only the mean circulation in April was analyzed.

Comparing monthly mean circulations, with the Irbe and Suur straits being either closed or opened, only minor differences emerge that occur mostly in the northern part of the gulf near the straits (Figs. 8a and 3b). The coefficient of determination between the two cases for April 1998 is  $R^2=0.93$ . Hence, we use closed boundaries for the three idealized simulations with 3-dimensional initial density gradient forcing, wind forcing and river discharge forcing accordingly.

To separate density-driven circulation, the simulation was initiated with salinity and temperature fields from the numerical model simulation results of 28 February 1998. Wind forcing and river discharge were excluded. Monthly mean circulation for April shows large anticyclonic circulation over the entire southern GoR reaching up to 57.75°N and a cyclonic loop in the northern part of the gulf (Fig. 8b).

In order to separate wind-driven circulation, simulation was initiated with uniform water density. Wind forcing from March and April 1998 was applied, while river discharge was switched off. Resulting circulation shows a double-gyre pattern with an anticyclonic loop in the southeastern part and a large cyclonic gyre over the central and northwestern parts (Fig. 8c). Wind in April 1998 was mainly from the east and northeast.

To separate river circulation, a simulation was initiated with a uniform ambient salinity of  $5 \text{ g kg}^{-1}$ . Wind forcing was switched off. The Daugava River discharge from March and April 1998 was applied. The resulting monthly mean circulation for April shows a river water bulge near the river mouth and a cyclonic coastal current along the eastern coast. Rest of the GoR is covered by weak cyclonic circulation (Fig. 8d). Monthly mean river discharge was  $1700 \text{ m}^3 \text{ s}^{-1}$  and  $1188 \text{ m}^3 \text{ s}^{-1}$  in March and April 1998, respectively.

The sensitivity tests show that wind forcing dominantly from the east as well as 3-dimensional density gradient forcing result in anticyclonic circulation at a depth of 5 m in the southern GoR in April 1998. Moreover, when we used initial 3-dimensional density distribution from 28 February 2006, the result was once again an anticyclonic circulation pattern in the southern GoR. The buoyancy input by the river does not produce anticyclonic circulation, but

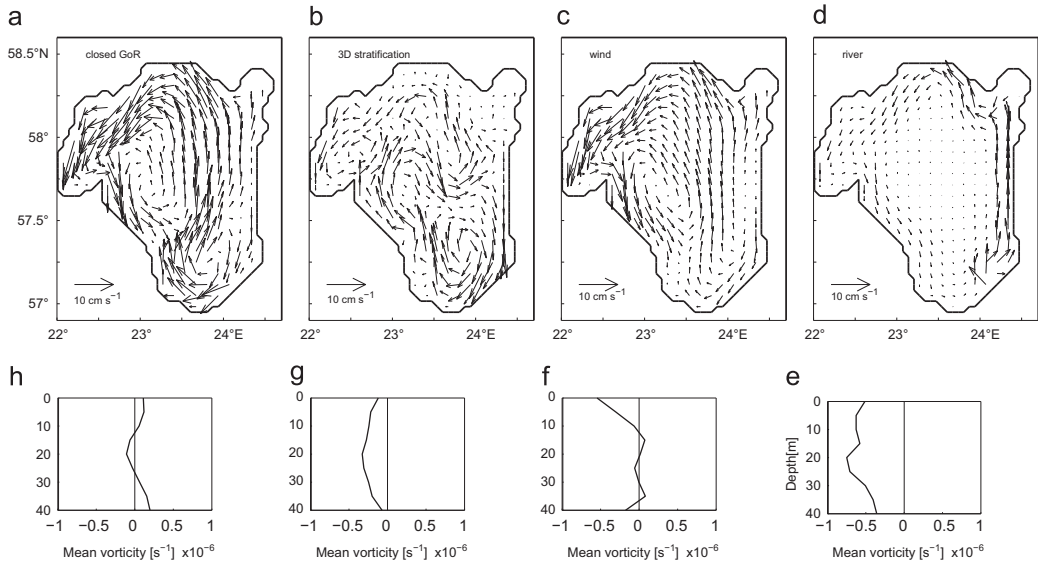


**Fig. 8.** (a)–(d) Monthly mean velocity patterns at a depth of 5 m (in April 1998) from the idealized simulations. (a) Closed boundary at the Irbe and Suur straits, (b) 3-dimensional density gradient forcing, (c) wind forcing from March and April 1998, (d) river discharge forcing in March and April 1998, and (e)–(h) respective vertical profiles of the relative vorticity averaged over the south-eastern part of the GoR (see Fig. 1 for the area).

merely contributes to the anticyclonic shear within the river bulge area. Obviously, this particular realization is not the result of a single factor, but a combination of them.

### 3.4. Relative vorticity

We study the rotation patterns further by using monthly mean relative vorticity. The PCA modes represent orthogonal flow patterns at a depth of 5 m over the whole GoR. Spatially averaged relative vorticity provides evidence for the presence of either anticyclonic or cyclonic circulation in the southern part of the GoR (see Fig. 1 for the area). The area was selected to capture the anticyclonic circulation according to the flow scheme of the first mode in the southeastern GoR (Fig. 6a). First, vertical profiles of horizontally averaged relative vorticity at 5 m depth intervals were calculated over the southern part of the gulf. Then, the relative vorticity profiles were vertically averaged while presuming that relative vorticity is homogeneous in the 5-m thick layers.

In the southern part of the GoR negative mean vorticity is clearly dominant during the spring period (Fig. 9). Frequency as well as average and maximum values are higher in the case of negative vorticity. Thus, when we use relative vorticity for describing the circulation in the southern GoR, we get “asymmetric” temporal occurrence of cyclonic and anticyclonic circulation. On the other hand, when we use the circulation pattern of the first principal mode for describing the circulation in the GoR, we get “symmetric” temporal occurrence of cyclonic and anticyclonic circulations. Still, there is a statistically significant linear relationship between the mean vorticity and the PA of the first mode ( $R^2=0.62$ ,  $p < 0.001$ ) (Figs. 6a, d and 9).

Vertical profiles of relative vorticity were calculated from the idealized test cases over the same area in the southern GoR. Relative vorticity is negative all over the water column when the GoR is closed (Fig. 8e). Vertically averaged vorticity is close to the value of the continuous run in April 1998, being  $-0.56 \times 10^{-6} \text{ s}^{-1}$  and  $-0.50 \times 10^{-6} \text{ s}^{-1}$  in the case of the straits closed and opened, respectively. In the case of 3-dimensional density gradient forcing,

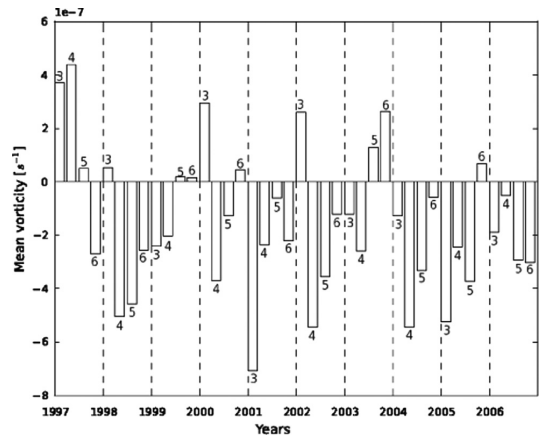


**Fig. 9.** Monthly mean relative vorticity averaged over the southern part of the GoR (see Fig. 1 for the area) from March, April, May and June 1997–2006.

relative vorticity is negative in the upper 10-m layer and around zero below (Fig. 8f), so that vertically averaged vorticity is negative,  $-0.11 \times 10^{-6} \text{ s}^{-1}$ . Wind forcing results in negative vorticity over the whole water column with a vertically averaged value of  $-0.2 \times 10^{-6} \text{ s}^{-1}$  (Fig. 8g). Buoyancy forcing caused by river inflow results in positive vorticity in the upper and lower 10-m thick layers, while being negative in the intermediate layer (Fig. 8h). Vertically averaged vorticity is  $0.06 \times 10^{-6} \text{ s}^{-1}$ .

### 3.5. Linear regression model for vorticity time series

The monthly mean values of PEA, river discharge,  $Q_R$ , wind mixing, monthly accumulated salt flux through transect in the Irbe Strait,  $S_f$ , east-west and north-south components of monthly accumulated wind impulses,  $I_x$  and  $I_y$ , and density difference

between northwestern and southeastern GoR,  $\Delta\rho$ , were considered as potential factors affecting cyclonic/anticyclonic circulation in the southern GoR. Positive salt flux means that salt is transported into the GoR. Monthly mean density values at atmospheric pressure have been calculated from two sites and at different depths. The northwestern site is located at 57°42' N 22° 52' E where the density has been calculated at a depth of 30 m, and the southeastern site is located at 57° 13' N 24° 4' E where the density has been calculated at a depth of 5 m. Only monthly mean salinity values were extracted from the numerical model while the temperature was kept constant with the value of 10 °C. Choosing the density difference between these locations and depth levels will take both the horizontal density gradient as well as the vertical stratification into account, thus being a proxy for the 3-dimensional density gradient.

At first, a multiple regression model for the dependent variable of vertically averaged vorticity,  $\omega$ , that included all above listed independent variables was applied. Obviously, this model was an exaggeration of the physical factors that could affect vertically averaged vorticity in the southern GoR. The rough model revealed that zero hypothesis can be rejected for the east–west wind impulse and density difference. Therefore, a new multiple linear regression model including these two independent variables was built. Model sensitivity tests showed that both wind with a mean vector from the east as well as the 3-dimensional density gradient can drive anti-cyclonic circulation in the southern GoR (Fig. 8b and c). Overall goodness of fit of the model for monthly mean spatially averaged relative vorticity in the southern GoR

$$\omega = a_1 I_x + a_2 \Delta\rho \quad (5)$$

( $a_1 = 4.23 \times 10^{-10} \text{ s kg}^{-1}$ ,  $a_2 = -3.4 \times 10^{-7} \text{ kg g}^{-1} \text{ s}^{-1}$ ) is rather high ( $R^2 = 0.77$ ,  $p < 10^{-4}$ ). A *t*-test for separate coefficients has

$p < 10^{-4}$  for both coefficients. Density difference between selected locations is maintained by river discharge in the gulf head (Daugava River) and salt flux in the gulf mouth (Irbe Strait), so that we obtain the multiple linear regression model for  $\Delta\rho$

$$\Delta\rho = b_1 Q_R + b_2 S_f \quad (6)$$

( $b_1 = 5.5 \times 10^{-4} \text{ g kg}^{-1} \text{ s m}^{-3}$ ,  $b_2 = 3.17 \times 10^{-13} \text{ s m}^{-3}$ ) with  $R^2 = 0.67$  ( $p < 10^{-4}$ ). The *p*-values for  $Q_R$  and  $S_f$  are  $p < 10^{-4}$  and  $p = 0.016$ , respectively. Salt flux in Irbe Strait is related to the east–west wind impulse

$$S_f = c_1 I_x + c_2 \quad (7)$$

( $c_1 = -1.2 \times 10^9 \text{ g s m}^3 \text{ kg}^{-2}$ ,  $c_2 = 2.74 \times 10^{11} \text{ g m}^3 \text{ kg}^{-1} \text{ s}^{-1}$ ) ( $R^2 = 0.62$ ,  $p < 10^{-4}$ ). The scatterplots of dependent variables versus independent variables in (5), (6) and (7) are shown in Fig. 10. We have presented values calculated from the model results. Negative vorticity persists even at positive values of east–west wind impulse, while positive vorticity can be produced if east–west wind impulse, in case of our parameters, exceeds 500  $\text{kg s}^{-2}$ . (Fig. 10a). There is a tendency towards higher difference in density between southeastern and northwestern GoR being in favor of negative vorticity (Fig. 10b). River discharge contributes to the density difference but does not dominate in the process of setting up the density difference between southeastern and northwestern GoR (Fig. 10c). Positive salt flux in the Irbe Strait supplies saline water into the GoR and increases the density difference (Fig. 10d). Low values of density difference are related to negative salt flux. Salt flux is clearly negative when wind impulse is positive and exceeds the value of 500  $\text{kg s}^{-2}$  (Fig. 10e). At lower values of positive wind impulse salt flux can be either positive or negative, while negative wind impulse mainly supports salt flux into the GoR.

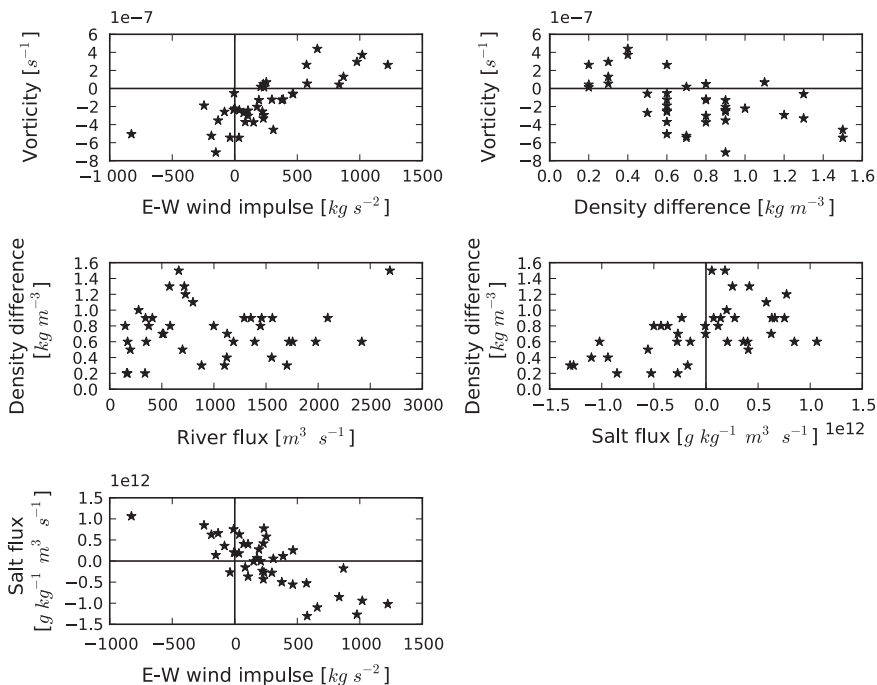


Fig. 10. Scatterplots of monthly mean (a) wind impulse and vorticity, (b) density difference and vorticity, (c) river flux and density difference, (d) salt flux and density difference, and (e) wind impulse and salt flux for the March–June periods of 1997–2006.

#### 4. Discussion

The results of a model simulation covering a period of ten years were analyzed to investigate circulation in the southern GoR in spring, when the GoR can be considered a gulf-type ROFI.

Our results show that double gyre circulation is the most prominent circulation pattern in the upper layer of the GoR. It may be either anticyclonic or cyclonic in the southeastern gulf and the opposite in the northwestern part. This pattern corresponds to the classical wind-forced double gyre circulation scheme in large lakes (Bennett, 1974) when there is steady wind from the east or west. Due to shallowness of the GoR, double-gyre wind-driven circulation is readily excited in the GoR (Raudsepp, 2001; Raudsepp et al., 2003). In addition to wind forcing, anticyclonic circulation in the southern GoR can be forced by three-dimensional density distribution. Baroclinic geostrophic adjustment in a rotating circular basin consists of a geostrophic component in the form of a basin-scale double gyre (Wake et al., 2004). In the case of the GoR, the anticyclonic gyre should reside over the southern and the cyclonic gyre over the northern gulf. The main connection of the GoR to the Baltic Sea is through the Irbe Strait with a sill depth of 22 m. This limits the water and salt exchange between the gulf and the Baltic Sea. After an inflow event in the Irbe Strait, we may treat the GoR as a closed circular basin where baroclinic geostrophic adjustment results in anticyclonic circulation in the southern gulf. According to theoretical considerations by Fujiwara et al. (1997), anticyclonic circulation is generated at the head of a wide estuary with a two-layer salinity stratification and a longitudinal salinity gradient. To preserve the latter, upward entrainment of lower layer water into the upper layer is required. The primary difference between baroclinic geostrophic adjustment and anticyclonic circulation driven by estuarine circulation is that when using potential vorticity formulation the horizontal divergence in the upper layer is in the case of the former caused by changes in layer thickness (Wake et al., 2004) and in the case of the latter by upward entrainment (Fujiwara et al., 1997). In the case of continuous salt transport to the GoR through the Irbe Strait, we presume that anticyclonic circulation is forced by the mechanism described by Fujiwara et al. (1997). Both mechanisms support the occurrence of anticyclonic circulation in the southern GoR. In the present study we are not trying to separate these two mechanisms.

McClimans et al. (2000) speculated that the anticyclonic circulation in the Kara Sea ROFI is caused by increased river discharge during previous months. Freshwater accumulated in the ROFI zone during intensive river discharge acts as a zonal barrier, directing the flow to the left during reduced discharge months. Idealized numerical experiments in the Kara Sea show that the absence of baroclinic effects (using uniform salinity and temperature distribution) results in cyclonic circulation (Panteleev et al., 2007). An observational study in the Kattegat–Skagerrak region (Nielsen, 2005) confirms the presence of strong anticyclonic circulation in that area. Although there is a strong horizontal density front separating the brackish Baltic Sea water in the upper layer and the North Sea saline water in the lower layer, he concluded that wind-generated vertical entrainment is the primary driving agent for the anticyclonic circulation.

The cyclonic/anticyclonic circulation in the southern GoR was accounted for through spatially averaged relative vorticity. Negative vorticity (anticyclonic circulation) is forced by the winds from the east and by the 3-dimensional density distribution that vertically takes into account the two layer stratification and horizontally the estuarine salinity distribution. Positive vorticity (cyclonic circulation) is forced by winds from the west. River discharge may contribute to negative or positive vorticity in the southern GoR. Previous simulations and laboratory experiments of buoyant discharges have shown that buoyant water can form

a large surface-trapped anticyclonic bulge (Garvine, 2001; Yankovsky and Chapman, 1997) near the river mouth, which has also been observed in the field (Huq, 2009; Horner-Devine et al., 2008). The formation of an anticyclonic bulge contributes to negative vorticity, while a coastal current contributes to positive vorticity. A bulge is expected to form if  $h/D \leq 0.25$  (Huq, 2009), where  $h = (2Q/g^*)^{1/2}$  is depth scale,  $D$  is ambient water depth,  $Q$  is river flow rate and  $g^*$  is reduced gravity. Rough estimates of  $h$  with a river discharge rate between 500 and 2500 m<sup>3</sup> s<sup>-1</sup>, and a density difference between 1 and 5 kg m<sup>-3</sup>, give values in the range of 1.5 to 7.5 m. Thus, we may expect that in certain months the anticyclonic buoyant bulge is well established, while in certain months river water is just deflected to the right from the river mouth. Our results showed that there is no significant relationship between the river discharge rate and the relative vorticity in the southern GoR, which indicates that the buoyancy input by Daugava River contributes to positive/negative vorticity in the southern GoR.

Taking into account potential forcing mechanisms and calculated monthly mean spatially averaged relative vorticity, we may conclude that there is asymmetry in the realization of either cyclonic or anticyclonic circulation in the southern GoR. The present study shows that negative mean vorticity is more frequent in the southern GoR than a positive one. A relatively strong positive east–west monthly accumulated wind impulse is needed to reverse anticyclonic circulation in the southern GoR.

Most previous studies assume that with little or no wind forcing river water will spread along the right hand coast, which is indeed the case when ambient water density is homogeneous. The present study supplements the common understanding of river water circulation by taking into account anticyclonic circulation caused by three-dimensional density stratification that transports river water to the left and offshore from the river mouth. Furthermore, nutrients as well as dissolved and particulate matter discharged by the river may be transported from the river mouth along the left hand coast. A numerical model study by Andrejev et al. (2010) for the Gulf of Finland shows anticyclonic circulation forming near the Neva River mouth and fresher water from the river discharge being partly transported along the left hand coast. While summarizing the measurement results, Wassman and Tamminen (1999) stated that the southwestern part in the GoR in spring was more influenced by the freshwater flow from the Daugava River than the south-eastern part and as a consequence phytoplankton bloom was more pronounced there.

#### 5. Conclusions

The spring (from March to June) circulation and spreading of river discharge water in the southern GoR was analyzed based on the results of a 10-year simulation (1997–2006) using the GETM for the entire Baltic Sea. Three basic circulation schemes prevail in the upper layer of the GoR in spring. Dominant circulation patterns in spring were the anticyclonic/cyclonic gyre in the southeastern and cyclonic/anticyclonic gyre in the northwestern part of the Gulf of Riga. The spreading of Daugava River water along the eastern coast of the GoR took place less frequently.

The anticyclonic/cyclonic circulation was accounted for with the spatially averaged relative vorticity in the southern GoR. There is asymmetry in the realization of cyclonic or anticyclonic circulation in the southern GoR. The present study shows that in the spring period anticyclonic circulation is far more frequent than cyclonic circulation.

The 3-dimensional estuarine type density field drives the anticyclonic circulation in the upper layer of the southern GoR in spring. The forming of circulation is either enhanced by the wind impulse from the east or destroyed or reversed to cyclonic circulation by the

wind impulse from the west. The 3-dimensional estuarine type density field is maintained by the salt flux in the Irbe Strait and by the freshwater discharge from the Daugava River. The wind impulse from the east directly drives the salt flux through the Irbe Strait into the GoR.

Our results suggest that anticyclonic circulation is a natural phenomenon in the wide ROFI caused by the 3-dimensional estuarine type density gradient, which is realized either by baroclinic geostrophic adjustment (Wake et al., 2004) in the case of an event like the supply of saline water, or by upward entrainment of lower layer water into the upper layer (Fujiwara et al., 1997) due to continuous inflow of saline water into the estuarine basin.

## Acknowledgments

This research was partially supported by the Estonian Science Foundation Grant nos. ETF8968 and ETF9278, BONUS+ECOSUP-PORT Project and Project EstKliima funded by the Environmental Protection and Technology Programme No 3.2.0802.11-0043 of the European Regional Fund.

## References

- Andrejev, O., Sokolov, A., Soomere, T., Värv, R., Viikmäe, B., 2010. The use of high-resolution bathymetry for circulation modelling in the Gulf of Finland. *Est. J. Eng.* 16, 187–210.
- Arakawa, A., Lamb, V.R., 1977. Computational design of the basic dynamical processes of the UCLA General Circulation Model. *Methods Comput. Phys.*, 173–263.
- Bennett, J.R., 1974. On the dynamics of wind-driven lake currents. *J. Phys. Oceanogr.* 4, 400–414.
- Burchard, H., Bolding, K., 2002. GETM – a general estuarine transport model. Scientific documentation. Technical Report EUR 20253 EN, European Commission.
- Burchard, H., Rennau, H., 2008. Comparative quantification of physically and numerically induced mixing in ocean models. *Ocean Model.* 20, 293–311.
- Choi, B.J., Wilkin, J.L., 2007. The effect of wind on the dispersal of the Hudson River plume. *J. Phys. Oceanogr.* 37, 1878–1897.
- Döscher, R., Willen, U., Jones, C., Rutgersson, A., Meier, H.E.M., Hansson, U., Graham, L.P., 2002. The development of the regional coupled ocean-atmosphere model RCAO. *Boreal Environ. Res.* 7, 183–192.
- Döscher, R., Wyser, K., Meier, H.E.M., Qian, M., Redler, R., 2010. Quantifying Arctic contributions to climate predictability in a regional coupled ocean-ice-atmosphere model. *Clim. Dyn.* 34, 1157–1176.
- Garvine, R.W., 2001. The impact of model configuration in studies of buoyant coastal discharge. *J. Mar. Res.* 59, 193–225.
- Horner-Devine, A.R., Fong, D.A., Monismith, S.G., 2008. Evidence for the inherent unsteadiness of a river plume: satellite observations of the Niagara River discharge. *Limnol. Oceanogr.* 53, 2731–2737.
- Horner-Devine, A.R., Fong, D.A., Monismith, S.G., Maxworthy, T., 2006. Laboratory experiments simulating a coastal river discharge. *J. Fluid Mech.* 555, 203–232.
- Höglund, A., Meier, H.E.M., Broman, B., Kriez, E., 2009. Validation and correction of regionalised ERA-40 wind fields over the Baltic Sea using the Rossby Centre Atmosphere model RCA3.0. *Oceanogr.* 97. SMHI, Norrköping, Sweden 46.
- Huq, P., 2009. The role of Kelvin number on bulge formation from estuarine buoyant outflows. *Estuaries Coasts* 32, 709–719.
- Janssen, F., Schrum, C., Backhaus, J., 1999. A climatological dataset of temperature and salinity for the North Sea and the Baltic Sea. *Ger. J. Hydrogr.* 9, 1–245.
- Jurisa, J.T., Chant, R., 2012. The coupled Hudson River estuarine-plume response to variable wind and river forcings. *Ocean Dyn.* 62, 771–784.
- Fujiwara, T., Sanford, L.P., Nakatsujic, K., Sugiyama, Y., 1997. Anticyclonic circulation driven by the estuarine circulation in a gulf type ROFI. *J. Mar. Syst.* 12, 83–99.
- Lindström, G., Janssen, F., Schrum, C., Backhaus, J., 2010. Development and testing of the HYPE (Hydrological Predictions for the Environment) water quality model for different spatial scales. *Hydro. Res.* 41, 295–319.
- Malačić, V., Petelin, P., 2009. Climatic circulation in the Gulf of Trieste (northern Adriatic). *J. Geophys. Res.—Oceans* 114, <http://dx.doi.org/10.1029/2008JC004904>.
- McClimans, T.A., Johnson, D.R., Krosshavn, M., King, S.E., Carroll, J., Grenness, O., 2000. Transport processes in the Kara Sea. *J. Geophys. Res.—Oceans* 105, 14,121–14,139.
- Nielsen, M.H., 2005. The baroclinic surface currents in the Kattegat. *J. Mar. Syst.* 55, 97–121.
- Osadchiv, A.A., Zavialov, P.O., 2013. Lagrangian model of a surface-advected river plume. *Cont. Shelf Res.* 58, 96–106.
- Panteleev, G., Proshutinsky, A., Kulakov, M., Nechaev, D.A., Maslowski, W., 2007. Investigation of the summer Kara Sea circulation employing a variational data assimilation technique. *J. Geophys. Res.—Oceans* 112, <http://dx.doi.org/10.1029/2006JC003728>.
- Passenko, J., Lessin, G., Raudsepp, U., Maljutenko, I., Neumann, T. and Laanemets, J., 2010. Analysis of temporal variability of measured and modeled vertical distributions of salinity and temperature in the Gulf of Finland during 10-year period. In: *Baltic International Symposium (BAL TIC)*, 2010 IEEE/OES US/EU. <http://dx.doi.org/10.1109/BAL TIC.2010.5621648>.
- Pietrzak, J., 1998. The use of TVD limiters for forward-in-time upstream-biased advection schemes in ocean modeling. *Mon. Weather Rev.* 126, 812–830.
- Preisendorfer, R.W., Mobley, C.D., 1988. *Principal Component Analysis in Meteorology and Oceanography*. Elsevier, Amsterdam.
- Raudsepp, U., Beletsky, D., Schwab, D.J., 2003. Basin-scale topographic waves in the Gulf of Riga. *J. Phys. Oceanogr.* 33, 1129–1140.
- Raudsepp, U., 2001. Interannual and seasonal temperature and salinity variations in the Gulf of Riga and corresponding saline water inflow from the Baltic Proper. *Nord. Hydrol.* 33, 135–160.
- Seifert, T., Tauber, F. and Kayser, B., 2001. A high Resolution Spherical Grid Topography of the Baltic Sea, revised ed. ([http://www.io-warnemuende.de/admin/de\\_indexhtml](http://www.io-warnemuende.de/admin/de_indexhtml)).
- Shchepetkin, A.F., McWilliams, J.C., 2003. A method for computing horizontal pressure-gradient force in an oceanic model with a nonaligned vertical coordinate. *J. Geophys. Res.—Oceans* 108, 347–404.
- Simpson, J.H., 1997. Physical processes in the ROFI regime. *J. Mar. Syst.* 12, 3–15.
- Soosaar, E., Sipeigas, L. and Raudsepp, U., 2010. Simple model calculations of the ice thickness for complementing satellite remote sensing of ice extent. In: *Baltic International Symposium (BAL TIC)*, 2010 IEEE/OES US/EU. <http://dx.doi.org/10.1109/BAL TIC.2010.5621637>.
- Stipa, T., Tamminen, T., Seppälä, J., 1999. On the creation and maintenance of stratification in the Gulf of Riga. *J. Mar. Syst.* 23, 27–49.
- Stips, A., Bolding, K., Pohlmann, T., Burchard, H., 2004. Simulating the temporal and spatial dynamics of the North Sea using the new model GETM (general estuarine transport model). *Ocean Dyn.* 54, 266–283.
- Umlauf, L., Burchard, H., 2005. Second-order turbulence closure models for geophysical boundary layers. A review of recent work. *Cont. Shelf Res.* 2, 795–827.
- Wake, G.W., Ivey, G.N., Imberger, J., McDonald, N.R., Stocker, R., 2004. Baroclinic geostrophic adjustment in a rotating circular basin. *J. Fluid Mech.* 515, 63–86.
- Wassman, P., Tamminen, T., 1999. Pelagic eutrophication and sedimentation in the Gulf of Riga: a synthesis. *J. Mar. Syst.* 23, 269–283.
- Whitney, M.M., Garvine, R.W., 2006. Simulating the Delaware Bay buoyant outflow: comparison with observations. *J. Phys. Oceanogr.* 36, 3–21.
- Yankovsky, A.E., Chapman, D.C., 1997. A simple theory for the fate of buoyant coastal discharges. *J. Phys. Oceanogr.* 27, 1386–1401.

# Acknowledgement

There are quite a number of people whom i would like to thank for all the support and help throughout my research. Mostly I would like to thank my supervisor Prof. Urmas Raudsepp and co-supervisor Prof. Robert D. Hetland for support and guidance during my Ph. D. studies.

I am deeply grateful to many of my colleagues and collaborators at the Marine Systems Institute who kindly shared their experiences: Ilja Maljutenko whos guidance and skill in numerical modeling have been invaluable for this work. Prof. Alex Horner-Devine for laboratory data, Dr. Rivo Uiboupin for a help with satellite data, Dr. Tarmo Kõuts and Dr. Maris Skudra for field data, Dr. Madis-Jaak Lilover for reviewing the thesis and making comments that helped to improve the manuscript and Sirje Sildever for her comments on parts of the work and sugar rushes over the years. Also no acknowledgement would be complete without mentioning my office companions. Peeter, Victor and Ilja, over the long years and multiple buildings you have provided companionship, heated discussions, wide range of ideas and questionable music selection. Without you this work would have probably been finished earlier. This road side by side in space have been quite a rollercoaster. Good luck with all and rock on.

The work was financially supported by institutional research funding IUT (19-6) of the Estonian Ministry of Education and Research. The author wishes to thank SA Archimedes DoRa programme, that made possible my stay in Texas A&M Univeristy.

Most important of all, I would like to express my thanks to my family and friends for their unfailing support, understanding and faith in me.

## Abstract

The main objective of the present thesis is to study the buoyant river bulge in the coastal sea and the circulation in the head of the gulf type ROFI. Freshwater discharge alters physical processes in the coastal sea by adding momentum and buoyancy. Also by creating some of the most biologically active and interesting regions by adding nutrients, pollutants and sediments.

Regional Ocean Modeling System and available laboratory data from a rotating circular basin experiment were used to study offshore spreading of buoyant bulge at laboratory scale. Altogether 11 pairs of laboratory-numerical simulation runs were analyzed. Development of a bulge and coastal current was observed in all experiments. Two phases of bulge spreading were identified. An initial rapid spreading phase lasted 0.3-0.7 rotation periods and a followed by slow expansion phase that lasted until the end of the simulation. During both phases bulge spreading scaled with the bulge Rossby radius. The shift from first phase to second coincided with the formation of the coastal current. Bulge front spreading agree well when inflow Kelvin number is about one. When  $K > 1/K < 1$ , the model underestimates/overestimates the bulge offshore reach.

Satellite remote sensing imagery and numerical modelling were used for the study of river bulge evolution and dynamics in a non-tidal sea, the Gulf of Riga (GoR) in the Baltic Sea. Total suspended matter (TSM) images showed a clearly formed anti-cyclonically rotating river bulge from Daugava River discharge during the studied low wind period. In about 7-8 days the bulge grew up to 20 km in diameter, before being diluted. Bulge growth rate was estimated as  $r_b \sim t^{0.31 \pm 0.23}$  ( $R^2=0.87$ ). A high resolution (horizontal grid step of 125 m) General Estuarine Transport Model (GETM) was used for detailed description of the development of the river plume in the southern GoR over the period when satellite images were acquired. In the model simulation, the  $r_b \sim t^{0.5 \pm 0.04}$  ( $R^2=0.90$ ). Both the model simulation and the satellite images showed that river water was mainly contained in the bulge and there were numerous intrusions at the outer perimeter of the bulge. We made numerical sensitivity tests with actual bathymetry and measured river runoff without wind forcing: 1) having initial 3-dimensional density distribution; 2) using initially a homogeneous ambient density field. In the first case, the anti-cyclonic bulge did not develop within the course of the model simulation and coastal current was kept offshore due to ambient density-driven circulation. In the second case, the river plume developed steadily into an anti-cyclonically recirculating bulge and a coastal current. Comparison of sensitivity test results with model runs with wind forcing included showed that wind has a significant effect in the evolution of the river bulge, even if the wind speed was moderate (3-4 m s<sup>-1</sup>). In the second case,  $r_b \sim t^{0.28 \pm 0.01}$  ( $R^2=0.98$ ). While previous studies conclude that mid-field bulge region is governed by balance between centrifugal, Coriolis and pressure gradient terms, our study showed that geostrophic balance is valid for the entire mid-field of the bulge. In addition, while there is discharge into the homogenous

GoR in case of high inflow Rossby number, the river inflow might split into two jets, with strong mixing zone in-between, in the plume near field region.

The spring (from March to June) circulation and spreading of river discharge water in the southern Gulf of Riga (GoR) in the Baltic Sea was analyzed based on the results of a 10-year simulation (1997–2006) using the General Estuarine Transport Model (GETM). Time series analysis of PCA and vorticity and model sensitivity tests were made. Monthly mean currents in the upper layer of the GoR revealed a double gyre structure dominated either by an anticyclonic or cyclonic gyre in the near-head south-eastern part and corresponding cyclonic/anticyclonic gyre in the near-mouth northwestern part of the gulf. It was concluded that anticyclonic circulation in the southern GoR is primarily driven by the estuarine type density field. In the spring the anticyclonic circulation in the upper layer of the southern GoR is driven primarily by the estuarine type density field. This anticyclonic circulation is enhanced by easterly winds but blocked or even reversed by westerly winds. The estuarine type density field is maintained by salt flux in the northwestern connection to the Baltic Proper and river discharge in the southern GoR.

## Resümees

Käesolevas töös „Jõevee levik rannikumeres Riia lahe näitel“ uuriti rannikumerre suubuva jõevee levikut, kasutades selleks laboriekspimente, satelliitvaatlusi ja erinevalt seadistatud numbrilisi mudeleid. Jõgede kaudu jõuab rannikumerre toitaineid, mis loovad eripärased ning kõrgendatud bioproduktiooniga alad, mille dünaamika mõistmine on oluline lisaks teadusele ka majanduslikult ning ka võimaliku reostusohu korral.

Kuna jõevee tihedus on väiksem kui mereveel, soodustab see horisontaalse ja vertikaalse tiheduse gradiendi moodustumist veesambas, mis omakorda mõjutab jõevee levikut suudmelähedasel merealal.

Ilma välise mõjutusteta, mis vett läbi segaks, moodustub jõe suudme lähedasel mere alal aja jooksul suurenev antitsüklaalne tsirkulatsioonipesa. Ainult osa jõeveest kantakse ära kitsas kaldahoovuses. Kuigi selline tsirkulatsioonipesa ilmneb nii mudelarvutustes kui ka laboriekspimentides, on selles piirkonnas reaalseste mõõtmiste läbiviimine ressursimahukas ja nõuab täpset ajastust. Lahendamata on mitmed küsimused, mis puudutavad vee ringlemist tsirkulatsioonipesas, mis on küll mudelis ja laboris kinnitatud, kuid vastavad mõõtmisandmed jõgede suudmetest on puudulikud.

Töö esimeses osas on uuritud jõevee levikut, kasutades kõrglahutuslikku ROMS-mudelit ja pöörleval laual sooritatud laboratooriumi eksperimendi tulemusi. Mudeli tulemuste kokkulangevus labori eksperimentidega on hea. Töö teises osas on uuritud jõevee levikut Liivi lahes, kasutades numbrilist mudelit GETM ja satelliidi TSM andmeid.

Daugava jõevee levik on analüüsitud tuulevaiksel perioodil 2007. aasta märtsis ja aprillis.

Kevadisi domineerivaid tsirkulatsioonimustreid on uuritud Liivi lahes perioodil 1997-2006, milleks on kasutatud GETM-mudeli simulatsiooni.

Käesoleva doktoritöö tulemused võib kokku võtta järgmiselt:

- Satelliidipildidelt saadud info tuulevaiksel perioodil 2007. aasta kevadel kinnitas, et Daugava jõevee tsirkulatsioonipesa pöörleb anti-tsüklaaalselt.
- Jõevee piirkonna laienemine toimub võrdeliselt väljavoolu Rossby raadiusega. Laienemise kiirus on hinnatud võrdeliseks  $t^{0.28-0.5}$ , mis langeb kokku eelnevate uuringute tulemustega.
- Tsirkulatsioonipesa laienemises saab eristada kahte faasi. Esimeses faasis, mis kestab 0.3-1 pöörlemisperioodi, toimub pesa laienemine kiiresti. Seejärel laienemiskiirus aeglustub ja jätkab stabiilset kasvu kuni vaadatud perioodi lõpuni. Üleminek esimesest teise faasi langeb ajaliselt kokku kaldahoovuse formeerumisega.

- Erinevalt eelnevatest uurimistöödest, kus järeldati, et tsirkulatsioonipesas on tasakaalus tsentrifugaal, Coriolisi ja rõhugradiendi jõud, siis käesoleva töö tulemus näitab, et domineeriv on geostroofiline tasakaal ning tsentrifugaaljõud on teistest jõududest suurusjärgu võrra väiksem.
- Lihtsustatud numbrilise mudeli tulemused näitavad, et suure Rossby arvu korral lahkneb jõevee väljavool suudmealas kaheks joaks, kuna nende vahel tekib intensiivse segunemise barjäär.
- Laboritingimustes mudeleksperimenti seadistades on oluline arvestada sissevoolu Kelvini numbrit. Kui Kelvini number on suurusjärgus üks, siis on mudeli tulemused heas kooskõlas laboritingimustes saadud tulemustega. Kui Kelvini number on suurem/väiksem, siis mudel vastavalt alahindab/ülehindab jõevee laieneva leviku kiirust.
- Kuu keskmised tsirkulatsioonimustrid näitavad, et Liivi lahe lõunaosas on kevadel domineeriv antitsükloonaalne taustahoovus. Otseselt mõjutab antitsükloonaalse taustahoovuse teket kolmemõõtmeline estuaarne tiheduse gradient.
- Antitsükloonaalne taustahoovus Liivi lahe taolistes piirkondades on kombinatsioon kahest protsessist. Esiteks soolase vee kerkimisest põhjakihtidest, mis on tingitud püsivast veevahetusest Läänemerega. Teiseks, ühekordsest suurema soolase vee hulga sissevoolust tingitud geostroofilisest kohandumisest.

# Curriculum Vitae

Name: Edith Soosaar

Date of birth: 6. september 1980

E-mail: [edith.soosaar@msi.ttu.ee](mailto:edith.soosaar@msi.ttu.ee)

## EDUCATION

2006 - ... Tallinn University of Technology. PhD student

2009 - 2010 Texas A&M, visiting scholar.

2005 - 2006 Tallinn University of Technology, Engineering Physics . MSc.

2006 – Studies and research at Polytechnic University of Catalonia

2000 - 2005 Tallinn University of Technology, Engineering Physics . BSc.

## PROFESSIONAL EMPLOYMENT

2006 - ... – Marine Systems Institute at Tallinn University of Technology, engineer.

2003 - 2006 Marine Systems Institute at Tallinn University of Technology, technician.

## SCIENTIFIC WORK

- Soosaar, Edith; Maljutenko, Ilja; Uiboupin, Rivo; Skudra, Maris; Raudsepp, Urmas. (2016). River bulge evolution and dynamics in a non-tidal sea – Daugava River plume in the Gulf of Riga, Baltic Sea. *Ocean Sci.*, Volume 12, 417–432
- Soosaar, Edith; Maljutenko, Ilja; Raudsepp, Urmas; Elken, Jüri. (2014). An investigation of anticyclonic circulation in the southern Gulf of Riga during the spring period. *Continental Shelf Research*, Volume 78, 75 - 84.
- Soosaar, Edith; Hetland, Robert D.; Horner-Devine, Alexander; Avenier, Margaret E.; Raudsepp, Urmas (2014). Offshore spreading of buoyant bulge from numerical simulations and laboratory experiments. In: *IEEE Xplore: Baltic International Symposium (BALTIC), 2014 IEEE/OES, 27-29 May 2014, Tallinn Estonia*. IEEE.
- Soosaar, Edith; Sipelgas, Liis; Raudsepp, Urmas (2010). Simple model calculations of the ice thickness for complementing satellite remote sensing of ice extent. In: *IEEE/OES Baltic 2010 International Symposium: IEEE/OES Baltic 2010 International Symposium*. IEEE-Inst Electrical Electronics Engineers Inc, 1 - 8.
- Myrberg, K.; Lehmann, A.; Raudsepp, U.; Szymelfenig, M.; Lips, I.; Lips, U.; Matciak, M.; Kowalewski, M.; Krężel, A.; Burska, D.; Szymanek, L.; Ameryk, A.; Bielecka, L.; Bradtke, K.; Gałkowska, A.; Gromisz, S.; Jędrasik, J.; Kaluźny, M.; Kozłowski, Ł.; Krajewska-Sołtys, A.; Ołdakowski, B.; Ostrowski, M.; Zalewski, M.; Andrejev, O.; Suomi, I.; Zhurbas, V.; Kauppinen, O-K.; Soosaar, E.; Laanemets, J.; Uiboupin, R.; Talpsepp, L.; Golenko, M.; Golenko, N.; Vahtera, E.

(2008). Upwelling events, coastal offshore exchange, links to biogeochemical processes – Highlights from the Baltic Sea Science Congress, March 19 – 22, 2007 at Rostock University. *Oceanologia*, 50(1), 95 - 113.

- Raudsepp, Urmas; Belikova, Viktoria; Lips, Urmas; Sipelgas, Liis; Soosaar, Edith; Uiboupin, Rivo (2007). The upwelling event in the southern Gulf of Finland in August 2006 on satellite images and in the numerical model results. Baltic Sea Science Congress, Rostock, 2007. 35.

### **DEFENDED THESES**

Soosaar, E. (2006). Numerical modeling of upwelling filaments in the Gulf of Finland. (Master thesis) Marine Systems Institute at Tallinn University of Technology.

### **LANGUAGE SKILLS**

Estonian – native language

English – good

Russian – beginner

# Elulookirjeldus

Nimi: Edith Soosaar

Sünniaeg: 6. september 1980

E-post: edith.soosaar@msi.ttu.ee

## HARIDUSTEE

2006 - ... Tallinna Tehnikaülikool, maa-teadused. Doktorant.

2009 - 2010 Texas A&M, doktorantuuri täiendusõpingud.

2005 - 2006 Tallinna Tehnikaülikool, tehniline füüsika. Magistriõpe.

2006 kevadsemester – Kataloonia Ülikool, magistrantuuri täiendusõpingud.

2000 - 2005 Tallinna Tehnikaülikool, tehniline füüsika. Bakalaureuseõpe.

## TEENISTUSKÄIK

2006 - ... – Meresüsteemide Instituut. Insener. Teaduslik uurimustöö ja doktorantuuri õpingud.

2003 - 2006 TTÜ Meresüsteemide Instituut. Tehnik.

## PUBLIKATSIOONID

- Soosaar, Edith; Maljutenko, Ilja; Uiboupin, Rivo; Skudra, Maris; Raudsepp, Urm. (2016). River bulge evolution and dynamics in a non-tidal sea – Daugava River plume in the Gulf of Riga, Baltic Sea. *Ocean Sci.*, Volume 12, 417–432
- Soosaar, Edith; Maljutenko, Ilja; Raudsepp, Urm. (2014). An investigation of anticyclonic circulation in the southern Gulf of Riga during the spring period. *Continental Shelf Research*, Volume 78, 75 - 84.
- Soosaar, Edith; Hetland, Robert D.; Horner-Devine, Alexander; Avenier, Margaret E.; Raudsepp, Urm. (2014). Offshore spreading of buoyant bulge from numerical simulations and laboratory experiments. In: *IEEE Xplore: Baltic International Symposium (BALTIC), 2014 IEEE/OES, 27-29 May 2014, Tallinn Estonia*. IEEE.
- Soosaar, Edith; Sipelgas, Liis; Raudsepp, Urm. (2010). Simple model calculations of the ice thickness for complementing satellite remote sensing of ice extent. In: *IEEE/OES Baltic 2010 International Symposium: IEEE/OES Baltic 2010 International Symposium*. IEEE-Inst Electrical Electronics Engineers Inc, 1 - 8.
- Myrberg, K.; Lehmann, A.; Raudsepp, U.; Szymelfenig, M.; Lips, I.; Lips, U.; Matciak, M.; Kowalewski, M.; Krężel, A.; Burska, D.; Szymanek, L.; Ameryk, A.; Bielecka, L.; Bradtke, K.; Gałkowska, A.; Gromisz, S.; Jędrasik, J.; Kaluźny, M.; Kozłowski, Ł.; Krajewska-Sołtys, A.; Ołdakowski, B.; Ostrowski, M.; Zalewski, M.; Andrejev, O.; Suomi, I.; Zhurbas, V.; Kauppinen, O-K.; Soosaar, E.; Laanemets, J.; Uiboupin, R.; Talpsepp, L.; Golenko, M.; Golenko, N.; Vahtera, E. (2008). Upwelling events, coastal offshore exchange, links to biogeochemical processes – Highlights from the Baltic Sea Science

- Congress, March 19 – 22, 2007 at Rostock University. *Oceanologia*, 50(1), 95 - 113.
- Raudsepp, Urmas; Belikova, Viktoria; Lips, Urmas; Sipelgas, Liis; Soosaar, Edith; Uiboupin, Rivo (2007). The upwelling event in the southern Gulf of Finland in August 2006 on satellite images and in the numerical model results . Baltic Sea Science Congress, Rostock, 2007. , 35.

## **KAITSTUD LÕPUTÖÖD**

Soosaar, E. (2006). Numerical modeling of upwelling filaments in the Gulf of Finland. (Magistritöö)TTÜ Meresüsteemide Instituut

## **VÕÕRKEELEOSKUS**

eesti keel – emakeel

inglise keel – suurepärane kõnes ja hea kirjas

vene keel – algaja

**DISSERTATIONS DEFENDED AT  
TALLINN UNIVERSITY OF TECHNOLOGY ON  
NATURAL AND EXACT SCIENCES**

1. **Olav Kongas**. Nonlinear Dynamics in Modeling Cardiac Arrhythmias. 1998.
2. **Kalju Vanatalu**. Optimization of Processes of Microbial Biosynthesis of Isotopically Labeled Biomolecules and Their Complexes. 1999.
3. **Ahto Buldas**. An Algebraic Approach to the Structure of Graphs. 1999.
4. **Monika Drews**. A Metabolic Study of Insect Cells in Batch and Continuous Culture: Application of Chemostat and Turbidostat to the Production of Recombinant Proteins. 1999.
5. **Eola Valdre**. Endothelial-Specific Regulation of Vessel Formation: Role of Receptor Tyrosine Kinases. 2000.
6. **Kalju Lott**. Doping and Defect Thermodynamic Equilibrium in ZnS. 2000.
7. **Reet Koljak**. Novel Fatty Acid Dioxygenases from the Corals *Plexaura homomalla* and *Gersemia fruticosa*. 2001.
8. **Anne Paju**. Asymmetric oxidation of Prochiral and Racemic Ketones by Using Sharpless Catalyst. 2001.
9. **Marko Vendelin**. Cardiac Mechanoenergetics *in silico*. 2001.
10. **Pearu Peterson**. Multi-Soliton Interactions and the Inverse Problem of Wave Crest. 2001.
11. **Anne Menert**. Microcalorimetry of Anaerobic Digestion. 2001.
12. **Toomas Tiivel**. The Role of the Mitochondrial Outer Membrane in *in vivo* Regulation of Respiration in Normal Heart and Skeletal Muscle Cell. 2002.
13. **Olle Hints**. Ordovician Scolecodonts of Estonia and Neighbouring Areas: Taxonomy, Distribution, Palaeoecology, and Application. 2002.
14. **Jaak Nõlvak**. Chitinozoan Biostratigraphy in the Ordovician of Baltoscandia. 2002.
15. **Liivi Kluge**. On Algebraic Structure of Pre-Operad. 2002.
16. **Jaanus Lass**. Biosignal Interpretation: Study of Cardiac Arrhythmias and Electromagnetic Field Effects on Human Nervous System. 2002.
17. **Janek Peterson**. Synthesis, Structural Characterization and Modification of PAMAM Dendrimers. 2002.
18. **Merike Vaher**. Room Temperature Ionic Liquids as Background Electrolyte Additives in Capillary Electrophoresis. 2002.
19. **Valdek Mikli**. Electron Microscopy and Image Analysis Study of Powdered Hardmetal Materials and Optoelectronic Thin Films. 2003.
20. **Mart Viljus**. The Microstructure and Properties of Fine-Grained Cermets. 2003.
21. **Signe Kask**. Identification and Characterization of Dairy-Related *Lactobacillus*. 2003.
22. **Tiiu-Mai Laht**. Influence of Microstructure of the Curd on Enzymatic and Microbiological Processes in Swiss-Type Cheese. 2003.
23. **Anne Kuusksalu**. 2–5A Synthetase in the Marine Sponge *Geodia cydonium*. 2003.
24. **Sergei Bereznev**. Solar Cells Based on Polycrystalline Copper-Indium Chalcogenides and Conductive Polymers. 2003.

25. **Kadri Kriis.** Asymmetric Synthesis of C<sub>2</sub>-Symmetric Bimorpholines and Their Application as Chiral Ligands in the Transfer Hydrogenation of Aromatic Ketones. 2004.
26. **Jekaterina Reut.** Polypyrrole Coatings on Conducting and Insulating Substrates. 2004.
27. **Sven Nõmm.** Realization and Identification of Discrete-Time Nonlinear Systems. 2004.
28. **Olga Kijatkina.** Deposition of Copper Indium Disulphide Films by Chemical Spray Pyrolysis. 2004.
29. **Gert Tamberg.** On Sampling Operators Defined by Rogosinski, Hann and Blackman Windows. 2004.
30. **Monika Übner.** Interaction of Humic Substances with Metal Cations. 2004.
31. **Kaarel Adamberg.** Growth Characteristics of Non-Starter Lactic Acid Bacteria from Cheese. 2004.
32. **Imre Vallikivi.** Lipase-Catalysed Reactions of Prostaglandins. 2004.
33. **Merike Peld.** Substituted Apatites as Sorbents for Heavy Metals. 2005.
34. **Vitali Syritski.** Study of Synthesis and Redox Switching of Polypyrrole and Poly(3,4-ethylenedioxythiophene) by Using *in-situ* Techniques. 2004.
35. **Lee Põllumaa.** Evaluation of Ecotoxicological Effects Related to Oil Shale Industry. 2004.
36. **Riina Aav.** Synthesis of 9,11-Secosterols Intermediates. 2005.
37. **Andres Braunbrück.** Wave Interaction in Weakly Inhomogeneous Materials. 2005.
38. **Robert Kitt.** Generalised Scale-Invariance in Financial Time Series. 2005.
39. **Juss Pavelson.** Mesoscale Physical Processes and the Related Impact on the Summer Nutrient Fields and Phytoplankton Blooms in the Western Gulf of Finland. 2005.
40. **Olari Ilison.** Solitons and Solitary Waves in Media with Higher Order Dispersive and Nonlinear Effects. 2005.
41. **Maksim Säkki.** Intermittency and Long-Range Structurization of Heart Rate. 2005.
42. **Enli Kiipli.** Modelling Seawater Chemistry of the East Baltic Basin in the Late Ordovician–Early Silurian. 2005.
43. **Igor Golovtsov.** Modification of Conductive Properties and Processability of Polyparaphenylene, Polypyrrole and polyaniline. 2005.
44. **Katrin Laos.** Interaction Between Furcellaran and the Globular Proteins (Bovine Serum Albumin  $\beta$ -Lactoglobulin). 2005.
45. **Arvo Mere.** Structural and Electrical Properties of Spray Deposited Copper Indium Disulphide Films for Solar Cells. 2006.
46. **Sille Ehala.** Development and Application of Various On- and Off-Line Analytical Methods for the Analysis of Bioactive Compounds. 2006.
47. **Maria Kulp.** Capillary Electrophoretic Monitoring of Biochemical Reaction Kinetics. 2006.
48. **Anu Aaspõllu.** Proteinases from *Vipera lebetina* Snake Venom Affecting Hemostasis. 2006.

49. **Lyudmila Chekulayeva.** Photosensitized Inactivation of Tumor Cells by Porphyrins and Chlorins. 2006.
50. **Merle Uudsemaa.** Quantum-Chemical Modeling of Solvated First Row Transition Metal Ions. 2006.
51. **Tagli Pitsi.** Nutrition Situation of Pre-School Children in Estonia from 1995 to 2004. 2006.
52. **Angela Ivask.** Luminescent Recombinant Sensor Bacteria for the Analysis of Bioavailable Heavy Metals. 2006.
53. **Tiina Lõugas.** Study on Physico-Chemical Properties and Some Bioactive Compounds of Sea Buckthorn (*Hippophae rhamnoides* L.). 2006.
54. **Kaja Kasemets.** Effect of Changing Environmental Conditions on the Fermentative Growth of *Saccharomyces cerevisiae* S288C: Auxo-accelerostat Study. 2006.
55. **Ildar Nisamedtinov.** Application of <sup>13</sup>C and Fluorescence Labeling in Metabolic Studies of *Saccharomyces* spp. 2006.
56. **Alar Leibak.** On Additive Generalisation of Voronoï's Theory of Perfect Forms over Algebraic Number Fields. 2006.
57. **Andri Jagomägi.** Photoluminescence of Chalcopyrite Tellurides. 2006.
58. **Tõnu Martma.** Application of Carbon Isotopes to the Study of the Ordovician and Silurian of the Baltic. 2006.
59. **Marit Kauk.** Chemical Composition of CuInSe<sub>2</sub> Monograin Powders for Solar Cell Application. 2006.
60. **Julia Kois.** Electrochemical Deposition of CuInSe<sub>2</sub> Thin Films for Photovoltaic Applications. 2006.
61. **Ilona Oja Açıık.** Sol-Gel Deposition of Titanium Dioxide Films. 2007.
62. **Tiia Anmann.** Integrated and Organized Cellular Bioenergetic Systems in Heart and Brain. 2007.
63. **Katrin Trummal.** Purification, Characterization and Specificity Studies of Metalloproteinases from *Vipera lebetina* Snake Venom. 2007.
64. **Gennadi Lessin.** Biochemical Definition of Coastal Zone Using Numerical Modeling and Measurement Data. 2007.
65. **Enno Pais.** Inverse problems to determine non-homogeneous degenerate memory kernels in heat flow. 2007.
66. **Maria Borissova.** Capillary Electrophoresis on Alkylimidazolium Salts. 2007.
67. **Karin Valmsen.** Prostaglandin Synthesis in the Coral *Plexaura homomalla*: Control of Prostaglandin Stereochemistry at Carbon 15 by Cyclooxygenases. 2007.
68. **Kristjan Piirimäe.** Long-Term Changes of Nutrient Fluxes in the Drainage Basin of the Gulf of Finland – Application of the PolFlow Model. 2007.
69. **Tatjana Dedova.** Chemical Spray Pyrolysis Deposition of Zinc Sulfide Thin Films and Zinc Oxide Nanostructured Layers. 2007.
70. **Katrin Tomson.** Production of Labelled Recombinant Proteins in Fed-Batch Systems in *Escherichia coli*. 2007.
71. **Cecilia Sarmiento.** Suppressors of RNA Silencing in Plants. 2008.
72. **Vilja Mardla.** Inhibition of Platelet Aggregation with Combination of Antiplatelet Agents. 2008.

73. **Maie Bachmann.** Effect of Modulated Microwave Radiation on Human Resting Electroencephalographic Signal. 2008.
74. **Dan Hvonen.** Terahertz Spectroscopy of Low-Dimensional Spin Systems. 2008.
75. **Ly Villo.** Stereoselective Chemoenzymatic Synthesis of Deoxy Sugar Esters Involving *Candida antarctica* Lipase B. 2008.
76. **Johan Anton.** Technology of Integrated Photoelasticity for Residual Stress Measurement in Glass Articles of Axisymmetric Shape. 2008.
77. **Olga Volobujeva.** SEM Study of Selenization of Different Thin Metallic Films. 2008.
78. **Artur Jgi.** Synthesis of 4'-Substituted 2,3'-dideoxynucleoside Analogues. 2008.
79. **Mario Kadastik.** Doubly Charged Higgs Boson Decays and Implications on Neutrino Physics. 2008.
80. **Fernando Prez-Caballero.** Carbon Aerogels from 5-Methylresorcinol-Formaldehyde Gels. 2008.
81. **Sirje Vaask.** The Comparability, Reproducibility and Validity of Estonian Food Consumption Surveys. 2008.
82. **Anna Menaker.** Electrosynthesized Conducting Polymers, Polypyrrole and Poly(3,4-ethylenedioxythiophene), for Molecular Imprinting. 2009.
83. **Lauri Ilison.** Solitons and Solitary Waves in Hierarchical Korteweg-de Vries Type Systems. 2009.
84. **Kaia Ernits.** Study of In<sub>2</sub>S<sub>3</sub> and ZnS Thin Films Deposited by Ultrasonic Spray Pyrolysis and Chemical Deposition. 2009.
85. **Veljo Sinivee.** Portable Spectrometer for Ionizing Radiation "Gammamapper". 2009.
86. **Jri Virkepu.** On Lagrange Formalism for Lie Theory and Operadic Harmonic Oscillator in Low Dimensions. 2009.
87. **Marko Piirsoo.** Deciphering Molecular Basis of Schwann Cell Development. 2009.
88. **Kati Helmja.** Determination of Phenolic Compounds and Their Antioxidative Capability in Plant Extracts. 2010.
89. **Merike Smera.** Sobemoviruses: Genomic Organization, Potential for Recombination and Necessity of P1 in Systemic Infection. 2010.
90. **Kristjan Laes.** Preparation and Impedance Spectroscopy of Hybrid Structures Based on CuIn<sub>3</sub>Se<sub>5</sub> Photoabsorber. 2010.
91. **Kristin Lippur.** Asymmetric Synthesis of 2,2'-Bimorpholine and its 5,5'-Substituted Derivatives. 2010.
92. **Merike Luman.** Dialysis Dose and Nutrition Assessment by an Optical Method. 2010.
93. **Mihhail Berezovski.** Numerical Simulation of Wave Propagation in Heterogeneous and Microstructured Materials. 2010.
94. **Tamara Aid-Pavlidis.** Structure and Regulation of BDNF Gene. 2010.
95. **Olga Bragina.** The Role of Sonic Hedgehog Pathway in Neuro- and Tumorigenesis. 2010.

96. **Merle Randrüüt.** Wave Propagation in Microstructured Solids: Solitary and Periodic Waves. 2010.
97. **Marju Laars.** Asymmetric Organocatalytic Michael and Aldol Reactions Mediated by Cyclic Amines. 2010.
98. **Maarja Grossberg.** Optical Properties of Multinary Semiconductor Compounds for Photovoltaic Applications. 2010.
99. **Alla Maloverjan.** Vertebrate Homologues of Drosophila Fused Kinase and Their Role in Sonic Hedgehog Signalling Pathway. 2010.
100. **Priit Pruunsild.** Neuronal Activity-Dependent Transcription Factors and Regulation of Human *BDNF* Gene. 2010.
101. **Tatjana Knjazeva.** New Approaches in Capillary Electrophoresis for Separation and Study of Proteins. 2011.
102. **Atanas Katerski.** Chemical Composition of Sprayed Copper Indium Disulfide Films for Nanostructured Solar Cells. 2011.
103. **Kristi Timmo.** Formation of Properties of  $\text{CuInSe}_2$  and  $\text{Cu}_2\text{ZnSn}(\text{S,Se})_4$  Monograin Powders Synthesized in Molten KI. 2011.
104. **Kert Tamm.** Wave Propagation and Interaction in Mindlin-Type Microstructured Solids: Numerical Simulation. 2011.
105. **Adrian Popp.** Ordovician Proetid Trilobites in Baltoscandia and Germany. 2011.
106. **Ove Pärn.** Sea Ice Deformation Events in the Gulf of Finland and This Impact on Shipping. 2011.
107. **Germo Väli.** Numerical Experiments on Matter Transport in the Baltic Sea. 2011.
108. **Andrus Seiman.** Point-of-Care Analyser Based on Capillary Electrophoresis. 2011.
109. **Olga Katargina.** Tick-Borne Pathogens Circulating in Estonia (Tick-Borne Encephalitis Virus, *Anaplasma phagocytophilum*, *Babesia* Species): Their Prevalence and Genetic Characterization. 2011.
110. **Ingrid Sumeri.** The Study of Probiotic Bacteria in Human Gastrointestinal Tract Simulator. 2011.
111. **Kairit Zovo.** Functional Characterization of Cellular Copper Proteome. 2011.
112. **Natalja Makarytsheva.** Analysis of Organic Species in Sediments and Soil by High Performance Separation Methods. 2011.
113. **Monika Mortimer.** Evaluation of the Biological Effects of Engineered Nanoparticles on Unicellular Pro- and Eukaryotic Organisms. 2011.
114. **Kersti Tepp.** Molecular System Bioenergetics of Cardiac Cells: Quantitative Analysis of Structure-Function Relationship. 2011.
115. **Anna-Liisa Peikolainen.** Organic Aerogels Based on 5-Methylresorcinol. 2011.
116. **Leeli Amon.** Palaeoecological Reconstruction of Late-Glacial Vegetation Dynamics in Eastern Baltic Area: A View Based on Plant Macrofossil Analysis. 2011.
117. **Tanel Peets.** Dispersion Analysis of Wave Motion in Microstructured Solids. 2011.

118. **Liina Kaupmees**. Selenization of Molybdenum as Contact Material in Solar Cells. 2011.
119. **Allan Olsper**. Properties of VPg and Coat Protein of Sobemoviruses. 2011.
120. **Kadri Koppel**. Food Category Appraisal Using Sensory Methods. 2011.
121. **Jelena Gorbatšova**. Development of Methods for CE Analysis of Plant Phenolics and Vitamins. 2011.
122. **Karin Viipsi**. Impact of EDTA and Humic Substances on the Removal of Cd and Zn from Aqueous Solutions by Apatite. 2012.
123. **David Schryer**. Metabolic Flux Analysis of Compartmentalized Systems Using Dynamic Isotopologue Modeling. 2012.
124. **Ardo Illaste**. Analysis of Molecular Movements in Cardiac Myocytes. 2012.
125. **Indrek Reile**. 3-Alkylcyclopentane-1,2-Diones in Asymmetric Oxidation and Alkylation Reactions. 2012.
126. **Tatjana Tamberg**. Some Classes of Finite 2-Groups and Their Endomorphism Semigroups. 2012.
127. **Taavi Liblik**. Variability of Thermohaline Structure in the Gulf of Finland in Summer. 2012.
128. **Priidik Lagemaa**. Operational Forecasting in Estonian Marine Waters. 2012.
129. **Andrei Errapart**. Photoelastic Tomography in Linear and Non-linear Approximation. 2012.
130. **Külliki Krabbi**. Biochemical Diagnosis of Classical Galactosemia and Mucopolysaccharidoses in Estonia. 2012.
131. **Kristel Kaseleht**. Identification of Aroma Compounds in Food using SPME-GC/MS and GC-Olfactometry. 2012.
132. **Kristel Kodar**. Immunoglobulin G Glycosylation Profiling in Patients with Gastric Cancer. 2012.
133. **Kai Rosin**. Solar Radiation and Wind as Agents of the Formation of the Radiation Regime in Water Bodies. 2012.
134. **Ann Tiiman**. Interactions of Alzheimer's Amyloid-Beta Peptides with Zn(II) and Cu(II) Ions. 2012.
135. **Olga Gavrilova**. Application and Elaboration of Accounting Approaches for Sustainable Development. 2012.
136. **Olesja Bondarenko**. Development of Bacterial Biosensors and Human Stem Cell-Based *In Vitro* Assays for the Toxicological Profiling of Synthetic Nanoparticles. 2012.
137. **Katri Muska**. Study of Composition and Thermal Treatments of Quaternary Compounds for Monograin Layer Solar Cells. 2012.
138. **Ranno Nahku**. Validation of Critical Factors for the Quantitative Characterization of Bacterial Physiology in Accelerostat Cultures. 2012.
139. **Petri-Jaan Lahtvee**. Quantitative Omics-level Analysis of Growth Rate Dependent Energy Metabolism in *Lactococcus lactis*. 2012.
140. **Kerti Orumets**. Molecular Mechanisms Controlling Intracellular Glutathione Levels in Baker's Yeast *Saccharomyces cerevisiae* and its Random Mutagenized Glutathione Over-Accumulating Isolate. 2012.
141. **Loreida Timberg**. Spice-Cured Sprats Ripening, Sensory Parameters Development, and Quality Indicators. 2012.

142. **Anna Mihhalevski.** Rye Sourdough Fermentation and Bread Stability. 2012.
143. **Liisa Arike.** Quantitative Proteomics of *Escherichia coli*: From Relative to Absolute Scale. 2012.
144. **Kairi Otto.** Deposition of In<sub>2</sub>S<sub>3</sub> Thin Films by Chemical Spray Pyrolysis. 2012.
145. **Mari Sepp.** Functions of the Basic Helix-Loop-Helix Transcription Factor TCF4 in Health and Disease. 2012.
146. **Anna Suhhova.** Detection of the Effect of Weak Stressors on Human Resting Electroencephalographic Signal. 2012.
147. **Aram Kazarjan.** Development and Production of Extruded Food and Feed Products Containing Probiotic Microorganisms. 2012.
148. **Rivo Uiboupin.** Application of Remote Sensing Methods for the Investigation of Spatio-Temporal Variability of Sea Surface Temperature and Chlorophyll Fields in the Gulf of Finland. 2013.
149. **Tiina Kriščiunaite.** A Study of Milk Coagulability. 2013.
150. **Tuuli Levandi.** Comparative Study of Cereal Varieties by Analytical Separation Methods and Chemometrics. 2013.
151. **Natalja Kabanova.** Development of a Microcalorimetric Method for the Study of Fermentation Processes. 2013.
152. **Himani Khanduri.** Magnetic Properties of Functional Oxides. 2013.
153. **Julia Smirnova.** Investigation of Properties and Reaction Mechanisms of Redox-Active Proteins by ESI MS. 2013.
154. **Mervi Sepp.** Estimation of Diffusion Restrictions in Cardiomyocytes Using Kinetic Measurements. 2013.
155. **Kersti Jääger.** Differentiation and Heterogeneity of Mesenchymal Stem Cells. 2013.
156. **Victor Alari.** Multi-Scale Wind Wave Modeling in the Baltic Sea. 2013.
157. **Taavi Päll.** Studies of CD44 Hyaluronan Binding Domain as Novel Angiogenesis Inhibitor. 2013.
158. **Allan Niidu.** Synthesis of Cyclopentane and Tetrahydrofuran Derivatives. 2013.
159. **Julia Geller.** Detection and Genetic Characterization of *Borrelia* Species Circulating in Tick Population in Estonia. 2013.
160. **Irina Stulova.** The Effects of Milk Composition and Treatment on the Growth of Lactic Acid Bacteria. 2013.
161. **Jana Holmar.** Optical Method for Uric Acid Removal Assessment During Dialysis. 2013.
162. **Kerti Ausmees.** Synthesis of Heterobicyclo[3.2.0]heptane Derivatives via Multicomponent Cascade Reaction. 2013.
163. **Minna Varikmaa.** Structural and Functional Studies of Mitochondrial Respiration Regulation in Muscle Cells. 2013.
164. **Indrek Koppel.** Transcriptional Mechanisms of BDNF Gene Regulation. 2014.
165. **Kristjan Pilt.** Optical Pulse Wave Signal Analysis for Determination of Early Arterial Ageing in Diabetic Patients. 2014.

166. **Andres Anier**. Estimation of the Complexity of the Electroencephalogram for Brain Monitoring in Intensive Care. 2014.
167. **Toivo Kallaste**. Pyroclastic Sanidine in the Lower Palaeozoic Bentonites – A Tool for Regional Geological Correlations. 2014.
168. **Erki Kärber**. Properties of ZnO-nanorod/In<sub>2</sub>S<sub>3</sub>/CuInS<sub>2</sub> Solar Cell and the Constituent Layers Deposited by Chemical Spray Method. 2014.
169. **Julia Lehner**. Formation of Cu<sub>2</sub>ZnSnS<sub>4</sub> and Cu<sub>2</sub>ZnSnSe<sub>4</sub> by Chalcogenisation of Electrochemically Deposited Precursor Layers. 2014.
170. **Peep Pitk**. Protein- and Lipid-rich Solid Slaughterhouse Waste Anaerobic Co-digestion: Resource Analysis and Process Optimization. 2014.
171. **Kaspar Valgepea**. Absolute Quantitative Multi-omics Characterization of Specific Growth Rate-dependent Metabolism of *Escherichia coli*. 2014.
172. **Artur Noole**. Asymmetric Organocatalytic Synthesis of 3,3'-Disubstituted Oxindoles. 2014.
173. **Robert Tsanev**. Identification and Structure-Functional Characterisation of the Gene Transcriptional Repressor Domain of Human Gli Proteins. 2014.
174. **Dmitri Kartofelev**. Nonlinear Sound Generation Mechanisms in Musical Acoustic. 2014.
175. **Sigrid Hade**. GIS Applications in the Studies of the Palaeozoic Graptolite Argillite and Landscape Change. 2014.
176. **Agne Velthut-Meikas**. Ovarian Follicle as the Environment of Oocyte Maturation: The Role of Granulosa Cells and Follicular Fluid at Pre-Ovulatory Development. 2014.
177. **Kristel Hälvin**. Determination of B-group Vitamins in Food Using an LC-MS Stable Isotope Dilution Assay. 2014.
178. **Mailis Pääri**. Characterization of the Oligoadenylate Synthetase Subgroup from Phylum Porifera. 2014.
179. **Jekaterina Kazantseva**. Alternative Splicing of *TAF4*: A Dynamic Switch between Distinct Cell Functions. 2014.
180. **Jaanus Suurväli**. Regulator of G Protein Signalling 16 (RGS16): Functions in Immunity and Genomic Location in an Ancient MHC-Related Evolutionarily Conserved Synteny Group. 2014.
181. **Ene Viiard**. Diversity and Stability of Lactic Acid Bacteria During Rye Sourdough Propagation. 2014.
182. **Kristella Hansen**. Prostaglandin Synthesis in Marine Arthropods and Red Algae. 2014.
183. **Helike Lõhelaid**. Allene Oxide Synthase-lipoxygenase Pathway in Coral Stress Response. 2015.
184. **Normunds Stivrins**. Postglacial Environmental Conditions, Vegetation Succession and Human Impact in Latvia. 2015.
185. **Mary-Liis Kütt**. Identification and Characterization of Bioactive Peptides with Antimicrobial and Immunoregulating Properties Derived from Bovine Colostrum and Milk. 2015.
186. **Kazbulat Šogenov**. Petrophysical Models of the CO<sub>2</sub> Plume at Prospective Storage Sites in the Baltic Basin. 2015.

187. **Taavi Raadik**. Application of Modulation Spectroscopy Methods in Photovoltaic Materials Research. 2015.
188. **Reio Põder**. Study of Oxygen Vacancy Dynamics in Sc-doped Ceria with NMR Techniques. 2015.
189. **Sven Siir**. Internal Geochemical Stratification of Bentonites (Altered Volcanic Ash Beds) and its Interpretation. 2015.
190. **Kaur Jaanson**. Novel Transgenic Models Based on Bacterial Artificial Chromosomes for Studying BDNF Gene Regulation. 2015.
191. **Niina Karro**. Analysis of ADP Compartmentation in Cardiomyocytes and Its Role in Protection Against Mitochondrial Permeability Transition Pore Opening. 2015.
192. **Piret Laht**. B-plexins Regulate the Maturation of Neurons Through Microtubule Dynamics. 2015.
193. **Sergei Žari**. Organocatalytic Asymmetric Addition to Unsaturated 1,4-Dicarbonyl Compounds. 2015.
194. **Natalja Buhhalko**. Processes Influencing the Spatio-temporal Dynamics of Nutrients and Phytoplankton in Summer in the Gulf of Finland, Baltic Sea. 2015.
195. **Natalia Maticiu**. Mechanism of Changes in the Properties of Chemically Deposited CdS Thin Films Induced by Thermal Annealing. 2015.
196. **Mario Öeren**. Computational Study of Cyclohexylhemicucurbiturils. 2015.
197. **Mari Kalda**. Mechanoenergetics of a Single Cardiomyocyte. 2015.
198. **Ieva Grudzinska**. Diatom Stratigraphy and Relative Sea Level Changes of the Eastern Baltic Sea over the Holocene. 2015.
199. **Anna Kazantseva**. Alternative Splicing in Health and Disease. 2015.
200. **Jana Kazarjan**. Investigation of Endogenous Antioxidants and Their Synthetic Analogues by Capillary Electrophoresis. 2016.
201. **Maria Safonova**. SnS Thin Films Deposition by Chemical Solution Method and Characterization. 2016.
202. **Jekaterina Mazina**. Detection of Psycho- and Bioactive Drugs in Different Sample Matrices by Fluorescence Spectroscopy and Capillary Electrophoresis. 2016.
203. **Karin Rosenstein**. Genes Regulated by Estrogen and Progesterone in Human Endometrium. 2016.
204. **Aleksei Tretjakov**. A Macromolecular Imprinting Approach to Design Synthetic Receptors for Label-Free Biosensing Applications. 2016.
205. **Mati Danilson**. Temperature Dependent Electrical Properties of Kesterite Monograin Layer Solar Cells. 2016.
206. **Kaspar Kevvai**. Applications of <sup>15</sup>N-labeled Yeast Hydrolysates in Metabolic Studies of *Lactococcus lactis* and *Saccharomyces Cerevisiae*. 2016.
207. **Kadri Aller**. Development and Applications of Chemically Defined Media for Lactic Acid Bacteria. 2016.
208. **Gert Preegel**. Cyclopentane-1,2-dione and Cyclopent-2-en-1-one in Asymmetric Organocatalytic Reactions. 2016.
209. **Jekaterina Služenikina**. Applications of Marine Scatterometer Winds and Quality Aspects of their Assimilation into Numerical Weather Prediction Model HIRLAM. 2016.

210. **Erkki Kask.** Study of Kesterite Solar Cell Absorbers by Capacitance Spectroscopy Methods. 2016.
211. **Jürgen Arund.** Major Chromophores and Fluorophores in the Spent Dialysate as Cornerstones for Optical Monitoring of Kidney Replacement Therapy. 2016.
212. **Andrei Šamarin.** Hybrid PET/MR Imaging of Bone Metabolism and Morphology. 2016.
213. **Kairi Kasemets.** Inverse Problems for Parabolic Integro-Differential Equations with Instant and Integral Conditions. 2016.